UNIVERSITY OF SOUTHAMPTON

FACULTY OF PHYSICAL SCIENCES AND ENGINEERING

Optoelectronics Research Centre

Integrated planar cavities for external cavity diode lasers

by

Stephen G. Lynch

Thesis for the degree of Doctor of Philosophy

June 2017

UNIVERSITY OF SOUTHAMPTON

ABSTRACT

FACULTY OF PHYSICAL SCIENCES AND ENGINEERING
Optoelectronics Research Centre

Doctor of Philosophy

INTEGRATED PLANAR CAVITIES FOR EXTERNAL CAVITY DIODE LASERS

by Stephen G. Lynch

External cavity diode lasers (ECDL) have demonstrated single mode operation, narrower linewidths, wider tuneability and lower noise operation when compared to fully monolithic diode lasers. An ECDL is a laser system that integrates a diode laser into a larger cavity permitting greater control over the laser properties. The external cavities are usually based on diffractions gratings and moving parts. This thesis is focused on making more stable, compact and versatile platforms based on integrated optical gratings. The fabrication and characterisation of three ECDL geometries is covered, all hosting direct UV-written planar Bragg gratings.

A planar glass-on-silicon chip with a UV-written Bragg grating and waveguide was coupled with a gain-chip to form a single mode 1651 nm laser suitable for methane gas sensing. The relative intensity noise (RIN) was measured to be <150 dB at 100 MHz. The laser was mixed with a replica to generate a beat note where the Lorentz linewidth was measured to be 220 kHz. Frequency offset locking to a replicated laser was demonstrated using a commercial phase locked loop chip. Using the laser, the R4 methane gas line at 1650.96 nm was measured down to a concentration of 1250 ppm at room temperature and atmospheric pressure.

A new ECDL for acetylene, based on a new optical platform consisting of a fibre-planar composite, coined integrated optical fibre (IOF), hosting a Bragg grating inscribed at 1532.83 nm. The RIN was measured and demonstrated improved noise characteristics compared to commercial ECDL. The linewidth was measured to be <14 kHz similar to commercial system. Finally, this system scanned the P13 acetylene line at 20 Torr at 20 °C, confirming the IOF 1532.83 nm operation.

In a third experiment, an ECDL was constructed at a wavelength of 1560.48 nm suitable for frequency doubling to 780 nm Rubidium spectroscopy. This system was adhered onto a silicon substrate and packaged in a small aluminium enclosure, demonstrating improved stability with improved low frequency RIN compared to the previous systems.

Contents

List of Figures

List of Symbols

α_{ab}	Coefficient of absorption. 43, 76
$\alpha(t)$	Instantaneous amplitude noise function. 35
α_L	Linear coefficient of thermal expansion. 83, 84
α	Henry's linewidth enhancement factor. 38
α_{SW}	Constant characterising a slab waveguide structure. 18, 19
β	Propagation constant. 18, 25, 26
$\Delta\beta$	Coupled-mode phase mismatch. 26
γ	Homogeneously broadened spectrum full-width half-maximum. 44, 45
δ	Kronecker delta function. 25
ε_0	Relative permittivity of free space. 17
ε_r	Relative permittivity of a material. 17, 23
θ_L	Littrow configuration angle. 6
κ	Coupled-mode equation coupling parameter. 26
κ_{SW}	Constant characterising a slab waveguide structure. 18, 19
Λ	Bragg grating fringe periodicity. 21–23, 25, 26, 72
λ	Wavelength of electromagnetic radiation in a vacuum. 5, 72, 153
λ_{Bragg}	Bragg wavelength. 22, 72, 75, 83
μ_0	Relative permeability of a free space. 17
μ_r	Relative permeability of a material. 17
$\delta\nu_{ST}$	Full-width at half maximum of the Schawlow-Townes linewidth. 38
$\delta\nu$	Full-width at half maximum of the linewidth. 39, 41, 113, 121
ν	Arbitrary constant. 76
$H(t)$	Heaviside step function. 85
ξ	Thermo-optic coefficient. 83, 84
ρ	Continous constant indexing cladding modes. 24
ρ_f	Free charge density. 16
κ	Coupled-mode equation self-coupling parameter. 26
τ	Arbitrary constant representing time, often time delay. 34, 40, 85, 113

τ_{rt} Round trip time of resonator. 38
θ_i Angle of incident light.. 5
θ_m Angle of diffracted light of order m.. 5
ϕ Bragg grating chirp function. 23, 26
$\phi(t)$ Instantaneous phase function. 34, 35, 37, 40, 114, 116–118
ω Angular frequency. 18

a Diffraction grating period.. 5

B Magnetic field. 16, 17

D Electric displacement. 16, 17
d Core layer thickness. 17, 18

$\mathcal{E}$ Discrete energy level of a quantum system. 42
E Electric field. 16–19, 24, 25, 113, 114
$\mathbb{E}[\cdot]$ Statistical expectation operator. 34

F_s Sampling rate. 116, 117

$\mathcal{H}[\cdot]$ Hilbert transform operator. 117
H Magnetic field strength. 16–18

I Absorption spectrum function. 44–46
I_{pd} Photocurrent from a photodiode. 35

J Free current density. 16

$k_{(\text{subscript})}$ Wave number or vector. 22
k_0 Free space wavenumber. 18
k Arbitrary constant used in phase noise model. 41
$\boldsymbol{K}_{\text{Br}}$ Bragg grating wave vector. 22

Length of the Bragg grating. 27
L_{coh} Coherence length. 113
L Resonator length. 39
L_{tot} Total resonator losses. 38

M Envelope function of forward propagating mode. 24–26
m Diffraction order.. 5

N	Envelope function of backward propagating mode. 24–26
n	Index of refraction. 17–19
N_{at}	Total number of atoms. 45
$n_{\text{at}}(v)$	Number of atoms with velocity between v and dv.. 45
Δn	Fluctuating component of Bragg effective index profile. 23
δn	Amplitude of sinusoidally varying component of Bragg effective index profile. 23
n_{eff}	Waveguide effective index of refraction. 22, 72, 74–76, 81
$\overline{n}_{\text{eff}}$	Steady state component of Bragg effective index profile. 23
P	Polarisation density. 24
p	Arbitrary constant. 27
$\mathcal{P}$	Electromagnetic power. 35, 37, 38, 126
q	Arbitrary constant. 27
R	Optical reflectivity. 76
R_{cm}	Forward propagating coupled-mode variable. 26, 27
R_x	Autocorrelation of the signal x. 34, 40, 113
$x(t)$	Random process in time t. 34
S	Poynting vector. 25
S_{cm}	Backward propagating coupled-mode variable. 26, 27
S_{q}	Surface roughness parameter. 66, 69, 70
S_x	Power spectral density of the signal x. 34, 35, 40, 41, 118
T	Integration time constant. 34
T_{oc}	Transmission of output coupler. 38
u	Discrete constant indexing guided modes. 24, 25
V	Normalised frequency of a slab waveguide. 19, 20
$V(t)$	Instantaneous voltage amplitude. 116–118
$v(t)$	Voltage signal. 116, 117
v	Gas molecule velocity. 45

Declaration of Authorship

I, Stephen G. Lynch, declare that the thesis entitled *Integrated planar cavities for external cavity diode lasers* and the work presented in the thesis are both my own, and have been generated by me as the result of my own original research. I confirm that:

- this work was done wholly or mainly while in candidature for a research degree at this University;
- where any part of this thesis has previously been submitted for a degree or any other qualification at this University or any other institution, this has been clearly stated;
- where I have consulted the published work of others, this is always clearly attributed;
- where I have quoted from the work of others, the source is always given. With the exception of such quotations, this thesis is entirely my own work;
- I have acknowledged all main sources of help;
- where the thesis is based on work done by myself jointly with others, I have made clear exactly what was done by others and what I have contributed myself;
- parts of this work have been published as: Appendix A

Signed:……

Date:……

"There is nothing like looking, if you want to find something. You certainly usually find something, if you look, but it is not always quite the something you were after."

J.R.R. Tolkien, The Hobbit

Acknowledgements

I would never have achieved what I have, become the person I am, without the incredible and talented individuals that I am privileged to be surrounded by. As such I would like to give a big thank you to those individuals.

To my supervisors. Prof. Peter Smith and Dr. James Gates who brought me into the fold. Without your deep knowledge, wisdom and patient guidance I would never have gotten here.

The many talented, warm, individuals and friends that are part of my research group. To Paolo Mennea for the fixing my UV-writing and soldering nightmares, and resisting the urge to dismember me. To Lewis Carpenter and Peter Cooper for showing me how to tame the rebellious Daisy. To Matthew Posner for being a loyal friend and course-mate since the beginning of our journey in Southampton. To Corin Gawith, for your life and career advice. To Chris Holmes for your support and guidance, and adding an exciting direction to my project. To Alexander Jantzen, Miranda Turvey, and Rex Bannerman, thank you for your questions and incredible personalities. To Teresa Ferreiro for your friendship, incredible patience, rational voice, and kind offer to proofread my thesis, without your support I cannot imagine having reached this point. To Sam Berry for entertaining my ridiculous thought experiments, the biscuits and coffee, the singing and music, the eye watering Thai green curries, you have been my one of my greatest friends throughout this journey. Thank you, all of you.

The friends I do not have the pleasure to work with. To Tony Curran, Peter West and Alex Melhuish for the pubs, the running, the life advice, and for enduring all my rants. Those friends I have not mentioned, you know who you are, thank you to you all.

To Mum and Dad, who have despite it all, have never failed to give your unconditional love and support.

Finally, to Gabriel for teaching me compassion, providing me love, friendship and devotion.

You all have my sincere thanks.

- Chapter 1 -

Introduction

1.1 Motivation

Since the diode laser was first demonstrated in 1962, it has been an area of intense research leading to a wider range of realisations in semiconductor materials and structures. Relative to many other types of lasers, diode lasers are cheaper, more efficient, compact and are available a wide range of colours from 231 nm in multiquantum-well AlGaN lasers [1] to 1.4 THz using quantum cascade lasers [2].

The wide gain bandwidths often demonstrated by semiconductor gain devices have made them useful as semiconductor optical amplifiers in telecommunications. These wide bandwidths have also seen them integrated into tuneable external cavities known as external cavity diode lasers (ECDLs). In this application, diode lasers have excelled and largely displaced tuneable dye lasers as a safer, longer lasting, relatively cheaper, and more compact alternative. The use of external cavities for CW diode lasers has demonstrated low noise, highly temporally coherent, single frequency operation.

Lasers are essentially electronic oscillators that operate at optical frequencies. Like electronic oscillators, the quality of their oscillations can be measured by the noise present in the strength of the field and the regularity or phase of the oscillations. The noise content of the optical field is the limiting factor for many applications where low noise operation is essential.

Nd:YAG nonplanar ring oscillators and fibre lasers have been demonstrated as some of the lowest noise and most coherent, free-running, single frequency devices available. As a result both have been considered suitable laser systems for the Laser Interferometer Space Antenna (LISA) [3], towards detecting gravitational waves. These lasers however

are limited to a small set of wavelengths determined by the relatively narrow bandwidth transitions of the rare elements they often utilise, in addition they are often more expensive than many ECDL-based systems. It is in applications that demand low noise, high coherence and wide tuneability at wavelengths unavailable to other lasers, that diode laser systems are favoured. This section will discuss several applications where ECDLs are widely used.

1.1.1 Gas spectroscopy and sensing

Diode lasers have been important for enabling the field of tunable diode-laser spectroscopy (TDLS). Taking advantage of their continuously-tunable and narrow linewidth operation. The optical interaction with the gas' quantum energy levels are utilised to detect and characterise the gas' spectral features, most commonly the optical absorptions. Single frequency diode lasers enable measurement of the spectral lines with extremely high resolution due to their narrow linewidths, and can be made to be self referencing [4]. For ambient atmospheric conditions, only laser linewidths of several MHz are needed as the broadened gas line has a width on the order of GHz. The advent of quantum cascade and interband cascade semiconductor lasers has extended the field to resolve spectral lines in the infra-red spectrum and even part of THz region [2], [4].

The procurement of single frequency diode lasers for gas sensing often is expensive compared to other types of sensors [4]. Diode lasers that are fabricated on wafers using lithographic processing that have to be developed for specific wavelengths of interest. For monolithic diode lasers, during any wafer process many laser chips will be unsuitable as their operational wavelength may fall outside of the spectroscopic line of interest due to limited manufacturing tolerances. As a result ECDL systems that usually utilise wide band diode gain-chips, providing wide tuneability, have become a popular optical source in TDLS. Separating fabrication of the wavelength selective element and the gain element into different processes significantly reduces the costs associated with developing these laser system that target specific wavelengths. However the mechanical nature of grating based lasers often make them unsuitable for field applications. More monolithic mechanically robust diode lasers that can either be fabricated cheaply at spectral lines of interest or tuned to them would be ideal for field sensing applications.

1.1.2 Coherent telecommunications

Near infra-red wavelengths have been the primary wavelengths used in optical communications, driven primarily by this spectral region's excellent transmission in silica optical fibres. Diode lasers generate light efficiently and readily at these wavelengths, and are also relatively cheap to produce and can be directly modulated. ECLDs offer additional advantages in noise and tuneability for this application.

Photodetectors on there own are unable to garner information about an optical field's phase. Direct detection schemes, where modulated light incident on a photodiode, without additional optical processing, are limited to amplitude based encodings. Modern, high capacity, fibre based, optical telecommunication systems usually encode data using phase shift keying (PSK), frequency shift keying (FSK) or quadrature amplitude modulation (QAM) schemes. These schemes encode data using the frequency or phase of an optical field, and in the case of QAM, in combination with amplitude. Detection of the field or phase in these encodings is often achieved using heterodyne detection where a coherent source is combined with the signal onto a photodetector producing an electronically detectable beat note. As a result these systems require highly temporally coherent lasers to minimise bit errors. These transmission systems therefore require highly coherent signal sources as well as coherent demodulation sources as the sources instabilities compound. This highlights the need for low noise, high coherence lasers [5].

Wavelength division multiplexed (WDM) communication systems transmit data using a number of different wavelengths channels simultaneously. This demands the requirement for narrow linewidth lasers to tune to the appropriate wavelengths for transmission and coherent detection. It also sets the requirement for lasers to be easily available at specific wavelengths of interest in the S, C and L (1460–1565 nm) bands. This makes ECDLs that exhibit both low noise, high coherence and often wavelength selectivity as attractive sources for use in coherent telecommunications.

1.2 Single frequency diode laser geometries

External cavities for diode based lasers have long been used to ensure single frequency operation, narrow linewidths, and vastly improved wavelength tuneability, in addition to being able to control and improve other laser properties. These external cavity systems once typically used standard "off-the-shelf" Fabry-Pérot (FP) diode lasers. Now, purpose designed broadband semiconductor gain chips, that are similar in design to

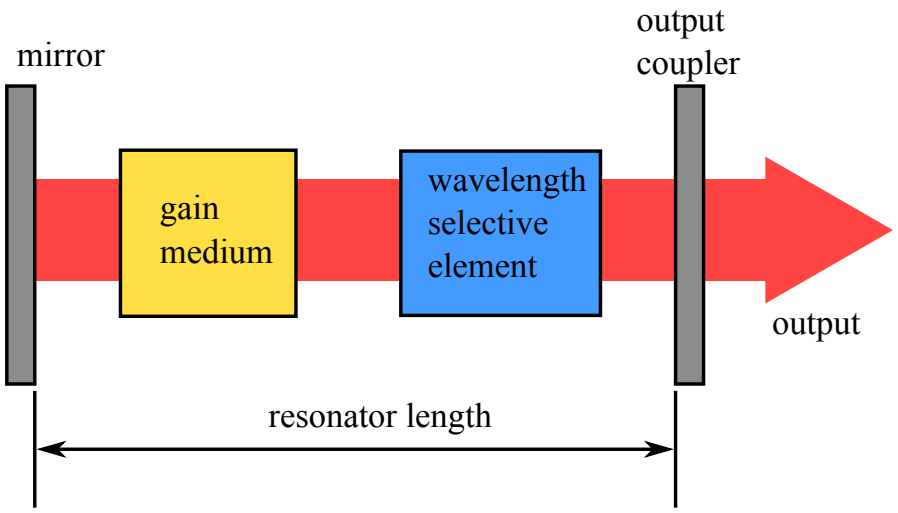

Figure 1.1: Diagram showing the typical components in abstract form of a single frequency laser.

diode lasers but utilise an anti-reflection coating and sometimes an angled facet on one or both facets, have become commonly produced. This allows them to be easily integrated into external cavity configurations with improved characteristics to their small cavity, single die, diode lasers counterparts. To the present date, a large number of creative cavity geometries have been investigated. These external cavities usually share some abstract functional components that are common to most single frequency lasers (Figure 1.1): a broadband semiconductor gain medium, a resonator, and a frequency selective component. In this abstract system, the frequency selective component rejects unwanted resonator modes within the broadband gain. The resonator can either be used to form the general laser resonator when using gain-chips, or a totally external resonator for monolithic diode lasers to provide additional feedback. This section will outline several commonly used external cavity types.

1.2.1 External Fabry-Pérot resonator

One of the earlier and still currently used methods of narrowing linewidth and ensuring single mode behaviour is to utilise weak optical feedback from a stable external FP cavity [6]. When a laser longitudinal mode matches a longitudinal mode of the FP cavity there is additional optical feedback. When utilising an ordinary FP diode laser the differing free spectral ranges (FSRs) of the diode laser cavity and the external cavity forces locking onto a single frequency. A cavity with higher finesse and round trip time results in the most significant reduction of frequency fluctuations and thus greater narrowing of the linewidth of the system [7]. The use of an external FP cavity has shown

to greatly improve laser linewidths, often reaching linewidths of kHz and recently as low as Hz [8]. However these systems require the laser to be electronically stabilised so that the diode laser internal cavity does not drift outside of the FP mode and thereby losing optical feedback locking [9]. In addition these types of cavities have limited tuning ranges and can be difficult to align, especially at high finesses.

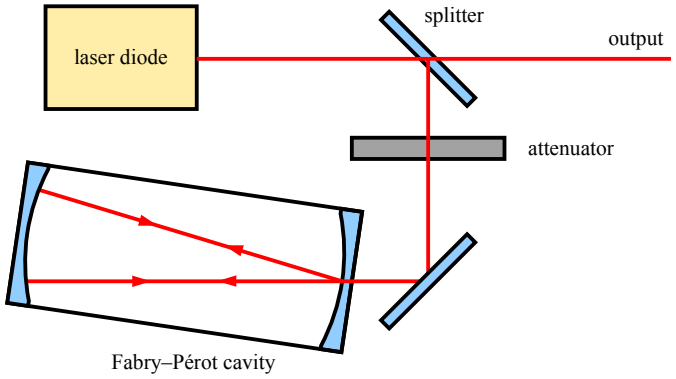

Figure 1.2: Typical layout of FP stabilised laser system [9].

1.2.2 Diffraction grating stabilised lasers

By far the most common and successful tuneable low linewidth ECDL lasers are those based on diffraction gratings. A diffraction grating is a reflective or transmissive optical surface with a structure with period comparable to the optical wavelength. Incident light onto a diffraction grating interferes with itself, due to the periodic grating structure, and diffracts in specific directions given by the relation

$$a[\sin(\theta_m) + \sin(\theta_i)] = m\lambda, \tag{1.1}$$

where a is the grating period, θ_i is the angle of incident light, θ_m is the angle of deflected light of order m and λ is the wavelength of the light.

The wavelength dependence of the direction of reflection can be used to provide feedback to a diode laser, using this wavelength dependence to filter out other undesired longitudinal modes. There are two main geometries used to make a grating based ECDL known as the Littrow and Littman-Metcalf (or just Littman) and these are depicted in Figure 1.3 [10], [11].

A special solution to Equation 1.1 where both θ_i and θ_m are equal with $m = 1$ is known as the Littrow configuration. This configuration where the first order diffraction and

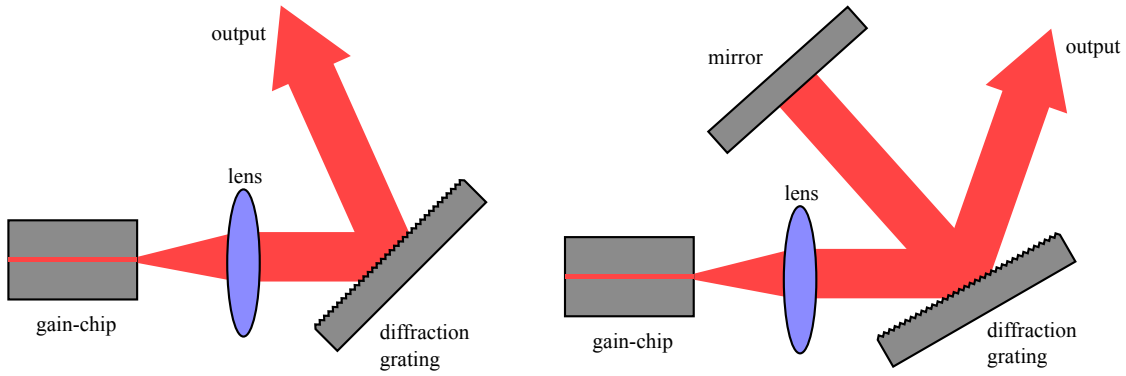

(a) Littrow configuration (b) Littman-Metcalf configuration

Figure 1.3: The two main configurations used in diffraction grating based ECDLs.

incident light are the same angle, denoted by the angle θ_L, is described by the relation (Figure 1.3a)

$$\lambda = 2a \sin(\theta_L). \tag{1.2}$$

This allows the diffraction to be used to provide optical feedback with a gain-chip which has a strong wavelength dependence on the angle of light to the diffraction grating, thus tuning is achieved by changing the angle of light incident on the grating. The output light can be collected from the zeroth order diffracted light, however the direction of this diffracted light is dependent on the angle of the diffraction grating which in many applications is inconvenient. As a result it is typical for gain-chips designed for Littrow geometries use a weakly reflective 10 % coated facet in addition to a completely anti-reflection coated facet. The direction of light collected from the 10 % will therefore be independent of tuning the wavelength.

The Littman configuration uses a fixed diffraction grating and tuning in contrast achieved using a rotating mirror as shown in Figure 1.3b. Tuning occurs by changing the angle of the first order diffraction by rotating the angle of the mirror. Unlike the Littrow system, the output can be easily obtained directly from the diffraction grating using the zeroth order diffraction, where the output direction does not change with tuning. However this system has higher intracavity losses due to additional intracavity reflections off the grating compared to the Littrow configuration.

A modification can be made to these basic configurations to ensure mode hop free tuning over their full tuning ranges. By modifying the cavity length of the system whilst wavelength tuning. This ensures the grating centre wavelength changes at the

exact same rate as the longitudinal mode solution of the cavity. This can usually be achieved by attaching the grating or mirror to the end of a rotating lever. Rotating the lever will then change the laser cavity length and the angle of the grating or mirror. When designed and aligned correctly, this configuration can allow mode hop free tuning over the entire range of the gain-chip bandwidth. The exact geometries that can be used to achieve this are discussed in [12].

1.2.3 Bragg grating stabilised lasers

The first diode lasers were simple designs that utilised cleaved ends as the reflectors forming a simple short cavity FP. However these lasers were highly broadband and would lase on all cavity modes simultaneously within the laser's gain bandwidth. This motivated the first usage of Bragg type reflectors in monolithic diode lasers. The first report of this kind of laser utilised the distributed feedback (DFB) configuration. In this configuration, the Bragg grating is distributed across the length of the active region, resulting in significant bandwidth narrowing [13], [14].

Though these laser were unable to achieve single mode operation until a modified design utilising a $\lambda/4$ phase shift in the grating periodicity was introduced into the centre of the grating structure resulting in reliable single mode devices [15], [16]. This phase shift effectively split the device into two Bragg reflectors allowing the existence of a single longitudinal mode within the structure. Simultaneously being developed was the distributed Bragg reflector (DBR) structure diode laser. This laser configuration utilised a dielectric Bragg reflector(s) that was not part of the active region of the laser but part of the same die. This also resulted in significant bandwidth narrowing and even single frequency operation [17]. In both DFB and DBR lasers the Bragg grating is integrated into the same die, this results in a short cavity length, often <1 mm, as such, typical commercial device linewidths are usually 1–2 MHz [18].

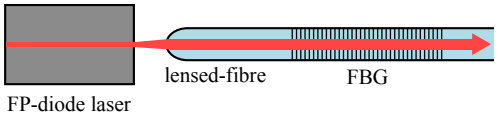

Figure 1.4: Layout of the FP laser stabilised to a fibre Bragg grating (FBG).

The short cavity DFB and DBR lasers resulted in high modulation chirp if directly modulated, and linewidths too broad for coherent telecommunications. These issues motivated the use of a FBG as an external reflector coupled to multi-mode FP diode lasers (see Figure 1.4). In this configuration, the spectral response of the external FBG

cavity could select a single longitudinal mode from the diode laser. By virtue of the long cavity, the lasing mode shows improvements in linewidth and chirp reduction [19], [20]. The main disadvantage with these types of lasers systems comes from the small FSR as a result of using a long external cavity.

The first reported use of integrated planar waveguides with diode lasers were from Ackerman and Olsson [21], [22]. These devices utilised a silicon nitride core, with silica cladding layers on a silicon substrate, deposited using chemical vapour deposition (CVD). These devices were successful at producing a single frequency laser with reduced linewidths <30 kHz. Recently a integrated planar waveguide based ECDL has been made available commercial with narrow linewidths at <3 kHz [23].

1.3 Research Context

The research presented in this thesis was conducted within the context of ongoing research including the author's research group at the University of Southampton's Optoelectronics Research Centre (ORC). This section will describe research occurring in the group and outside that influenced the aims and directions of the work described in this thesis.

The combination of capabilities and facilities in the ORC and the author's group presents a range of fabrication processes for optical device development. The accurate and rapid prototyping of UV-written waveguides and Bragg gratings, in combination with the available cleanroom fabrication capabilities, motivated a collaboration opportunity with Cranfield University, that started in October 2010. The project was to develop a tuneable single frequency planar waveguide diode laser for methane gas sensing. This laser would utilise a tuneable Bragg grating to lock the laser to a defined frequency. The author started in October 2012 and continued the research of this project, that would also serve as a basis for further research, which is described in this thesis.

In parallel to this project, the only other reported glass-based planar waveguide diode laser being investigated is a product that is produced by Redfern Integrated Optics[1], operating at wavelengths of 1530–1565 nm and 1064 nm. Their lasers demonstrated low noise and narrow linewidths; this motivated interest of the noise capabilities of the planar waveguide diode lasers that could be fabricated in the ORC.

The flame-hydrolysis deposition system was setup in 2011, after having been destroyed in a fire in the Mountbatten cleanroom complex at the University of Southampton.

[1] www.rio-lasers.com URL accurate as of September 2016.

The author joined in 2012; in that time, recipes for single mode, photosensitive silica based waveguides were becoming established. Interest for developing germanate based glasses having potential for increased photosensitivity and layer uniformity became a focus for research [24]. To complement this ongoing research the phosphogermanate glass was used as the first optical platform for the waveguide based laser systems outlined in this thesis.

Another researcher in the group, Chris Holmes successfully attached optical fibre to a silicon wafer with glass melt deposited using the flame-hydrolysis deposition system [25]. This new optical platform has the potential to combine the advantages of planar waveguide and optical fibre technologies. This started a new research interest to develop novel devices based on this new optical platform [26]–[30], including utilising this platform in a novel external cavity laser that will be described later in this thesis [31], [32].

1.4 Thesis Outline

This thesis will present the fabrication and results of two types of external cavity diode lasers one on glass-on-silicon planar platform, and the other using the new attached fibre platform. This section will describe the chapters to follow.

Chapter 2 will outline the theoretical physical basis needed to understand the waveguiding optical platform, and Bragg gratings that are used by the lasers investigated in this project. The physical sources and limits of noise in these systems will be considered. As these systems are demonstrated by characterising spectral lines, the spectral line broadening mechanisms are outlined and concludes this chapter.

Chapter 3 details the fabrication processes needed to build the devices developed during this PhD. This includes the fabrication of the optical platforms, optical machining, UV-writing of Bragg gratings and waveguides, lithographic processing and deposition, wire bonding of electrical connections, and finally the assembly and packaging of these systems.

Chapter 4 will describe the experimental results of a laser fabricated for methane gas sensing. Basic laser properties will be presented and the laser noise characterised. A demonstration of the laser's capability for locking and finally a demonstration of the laser's ability to resolve the R4 methane spectral line at 1651 nm will be detailed.

Chapter 5 will outline the experimental results of a single frequency laser based on a new attached fibre optical platform. These results include noise properties and a demonstration of a laser able to resolve the acetylene P13 line at 1533 nm.

Chapter 6 summarises the main conclusions from the work presented in this thesis, and give directions for continued research on these technologies.

Bibliography

[1] H. Hirayama, T. Yatabe, N. Noguchi, T. Ohashi, and N. Kamata, "231–261nm algan deep-ultraviolet light-emitting diodes fabricated on aln multilayer buffers grown by ammonia pulse-flow method on sapphire," *Appl. Phys. Lett.*, vol. 91, no. 7, p. 071 901, 2007.

[2] M. Tonouchi, "Cutting-edge terahertz technology," *Nat. Photon.*, vol. 1, no. 2, pp. 97–105, 2007.

[3] M. Tröbs, S. Barke, J. Möbius, M. Engelbrecht, D. Kracht, L. d'Arcio, G. Heinzel, and K. Danzmann, "Lasers for LISA: overview and phase characteristics," *JPCS*, vol. 154, no. 1, p. 012 016, 2009.

[4] J. Hodgkinson and R. P. Tatam, "Optical gas sensing: a review," *Meas. Sci. Technol.*, vol. 24, no. 1, p. 012 004, Jan. 2013.

[5] G. P. Agrawal, *Fiber-Optic Communication Systems*. John Wiley & Sons, 2002.

[6] B. Dahmani, L. Hollberg, and R. Drullinger, "Frequency stabilization of semiconductor lasers by resonant optical feedback," *Opt. Lett.*, vol. 12, no. 11, pp. 876–878, 1987.

[7] H. Li and H. Telle, "Efficient frequency noise reduction of GaAlAs semiconductor lasers by optical feedback from an external high-finesse resonator," *IEEE J. Quantum Electron.*, vol. 25, no. 3, pp. 257–264, 1989.

[8] W. Lewoczko-Adamczyk, C. Pyrlik, J. Häger, S. Schwertfeger, A. Wicht, A. Peters, G. Erbert, and G. Tränkle, "Ultra-narrow linewidth DFB-laser with optical feedback from a monolithic confocal Fabry-Perot cavity," *Opt. Express*, vol. 23, no. 8, pp. 9705–9709, 2015.

[9] C. E. Wieman and L. Hollberg, "Using diode lasers for atomic physics," *Rev. Sci. Instrum.*, vol. 62, no. 1, pp. 1–20, 1991.

[10] C. J. Hawthorn, K. P. Weber, and R. E. Scholten, "Littrow configuration tunable external cavity diode laser with fixed direction output beam," *Rev. Sci. Instrum.*, vol. 72, no. 12, p. 4477, 2001.

[11] K. Liu and M. G. Littman, "Novel geometry for single-mode scanning of tunable lasers," *Opt. Lett.*, vol. 6, no. 3, pp. 117–118, Mar. 1981.

[12] Y. Cunyun, *Tunable External Cavity Diode Lasers*. World Scientific, 2004.

[13] M. v. Nakamura, K. Aiki, J.-i. Umeda, A. Yariv, H. Yen, and T. Morikawa, "GaAs–$Ga_{1-x}Al_xAs$ double-heterostructure distributed-feedback diode lasers," *Appl. Phys. Lett.*, vol. 25, no. 9, pp. 487–488, 1974.

[14] D. Scifres, R. Burnham, and W. Streifer, "Distributed-feedback single heterojunction GaAs diode laser," *Appl. Phys. Lett.*, vol. 25, no. 4, pp. 203–206, 1974.

[15] K. Sekartedjo, N. Eda, K. Furuya, Y. Suematsu, F. Koyama, and T. Tanbun-Ek, "1.5 μm phase-shifted DFB lasers for single-mode operation," *Electron. Lett.*, vol. 20, no. 2, pp. 80–81, 1984.

[16] K. Utaka, S. Akiba, K. Sakai, and Y. Matsushima, "Analysis of quarter-wave-shifted DFB laser," *Electron. Lett.*, vol. 20, no. 8, pp. 326–327, 1984.

[17] R. Dupuis and P. Dapkus, "Room-temperature operation of distributed-bragg-confinement $ga_{1-x}al_xas$-gaas lasers grown by metalorganic chemical vapor deposition," *Appl. Phys. Lett.*, vol. 33, no. 1, pp. 68–69, 1978.

[18] J. Hecht, *The Laser Guidebook*. McGraw-Hill, New York, NY, 1986.

[19] E. Brinkmeyer, W. Brennecke, R. Ulrich, *et al.*, "Fibre bragg reflector for mode selection and line-narrowing of injection lasers," *Electron. Lett.*, vol. 3, no. 22, pp. 134–135, 1986.

[20] C. Park, C. Rowe, J. Buus, D. Reid, A. Carter, and I. Bennion, "Single-mode behaviour of a multimode 1.55 μm laser with a fibre grating external cavity," *Electron. Lett.*, vol. 21, no. 22, pp. 1132–1134, 1986.

[21] D. Ackerman, M. Dahbura, Y. Shani, C. Henry, R. Kistler, R. Kazarinov, and C. Kuo, "Compact hybrid resonant optical reflector lasers with very narrow linewidths," *Appl. Phys. Lett.*, vol. 58, no. 5, pp. 449–451, 1991.

[22] N. Olsson, C. Henry, R. Kazarinov, H. Lee, and B. Johnson, "Relation between chirp and linewidth reduction in external Bragg reflector semiconductor lasers," *Appl. Phys. Lett.*, vol. 51, no. 2, pp. 92–93, 1987.

[23] K. Numata, M. Alalusi, L. Stolpner, G. Margaritis, J. Camp, and M. Krainak, "Characteristics of the single-longitudinal-mode planar-waveguide external cavity diode laser at 1064 nm," *Opt. Lett.*, vol. 39, no. 7, pp. 2101–2104, Apr. 2014.

[24] M. T. Turvey, P. L. Mennea, P. G. Smith, and J. C. Gates, "Direct UV written waveguides in phosphogermanate planar glass layers fabricated via flame hydrolysis deposition," in *Integrated Photonics Research, Silicon and Nanophotonics*, Optical Society of America, 2016, ITu3A–3.

[25] C. Holmes, J. C. Gates, and P. G. R. Smith, "Planarised optical fiber composite using flame hydrolysis deposition demonstrating an integrated FBG anemometer.," *Opt. Express*, vol. 22, no. 26, pp. 32 150–7, 2014.

[26] C. Holmes, L. Carpenter, J. Gates, C. Gawith, and P. Smith, "Planarized fiber-FHD optical composite," in *SPIE OPTO*, International Society for Optics and Photonics, 2015, pp. 936 907–936 907.

[27] C. Holmes, J. Gates, L. Carpenter, M. A. Kudus, C. Gawith, G. Brambilla, and P. Smith, "Fiber-on-planar mechanical and optical composite," in *The European Conference on Lasers and Electro-Optics*, Optical Society of America, 2015, CE_2_5.

[28] C. Holmes, L. G. Carpenter, J. C. Gates, and P. G. Smith, "Optically integrated fiber: a new platform for harsh environmental sensing," in *Avionics and Vehicle Fiber-Optics and Photonics Conference (AVFOP), 2015 IEEE*, IEEE, 2015, pp. 3–4.

[29] A. Jantzen, C. Holmes, S. Lynch, M. T. Posner, R. Bannerman, and P. Smith, "Tilted Bragg gratings in integrated optical fiber," in *Bragg Gratings, Photosensitivity, and Poling in Glass Waveguides*, Optical Society of America, 2016, BT2B–2.

[30] C. Holmes, S. Lynch, A. Jantzen, L. G. Carpenter, R. Bannerman, S. A. Berry, J. C. Gates, and P. Smith, "Integrated optical fiber: a novel optical platform," in *Australian Conference on Optical Fibre Technology*, Optical Society of America, 2016, AM4C–3.

[31] S. G. Lynch, C. Holmes, S. A. Berry, J. C. Gates, A. Jantzen, T. I. Ferreiro, and P. G. R. Smith, "External cavity diode laser based upon an FBG in an integrated optical fiber platform," *Opt. Express*, vol. 24, no. 8, pp. 8391–8398, 2016.

[32] S. G. Lynch, C. Holmes, S. Berry, J. Gates, A. Jantzen, T. I. Ferreiro, and P. G. Smith, "Narrow linewidth external cavity diode laser using UV-written gratings in an integrated optical fiber platform," in *CLEO: Science and Innovations*, Optical Society of America, 2016, SW4M–7.

- Chapter 2 -

Theory

The single frequency laser systems investigated in this thesis utilise Bragg gratings hosted in dielectric waveguides. These lasers are most useful in applications that require a single, low noise, longitudinal mode. In this chapter the theory of dielectric waveguides and Bragg gratings is presented. A qualitative description of gain-chips is outlined. The sources of phase and intensity noise are described. Finally the physical basis of broadening in gas spectral lines is given.

2.1 Waveguides

Waveguides are devices that allows the transportation, even with bends, and provide a platform for the processing of electromagnetic radiation in a controlled geometry. Optical dielectric waveguides will confine the light to a small 2-dimensional geometry utilising total internal reflection in a dielectric structure. As well as being able to transport light, they provide a means to process the light in ways more difficult in free space, such as Bragg grating based sensors [1], [2] and can reduce or eliminate the need for alignment. The most successful example of a waveguiding technology is the single mode optical fibre that facilitates world wide international communications and the internet. Its primary source of success is the unparalleled low loss for near-infrared radiation transmitted over long distances. A number of optical devices have been developed based on optical fibre technology that include: splitters, modulators, interferometers and filters.

Dielectric planar waveguides are also a successful waveguiding technology. This geometry allows the fabrication and development of devices on wafers, enabling the use

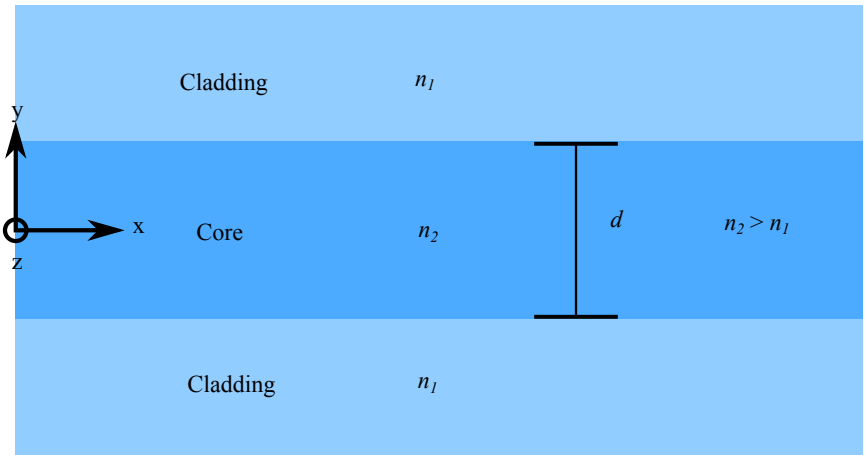

Figure 2.1: Diagram of a symmetric slab waveguide. This simple structure can be solved almost entirely analytically.

of well developed wafer processing technologies that exist due to the semiconductor industry. Two of the most successful examples are the fibre coupled electro-optic modulator (EOM) used in telecommunications that utilises the nonlinear crystal lithium niobate [3] as the host of single mode planar waveguides and the arrayed waveguide grating used in wavelength division multiplexing systems [4]. Planar waveguides have also been incorporated into a number of sensors and microelectromechanical systems [1].

2.1.1 Slab waveguide

To understand how light can be confined using a dielectric waveguide we can consider the simple symmetric dielectric structure as seen in Figure 2.1 where z is the axis of propagation. In this structure the refractive index profile varies only in the y-axis. This structure can be solved by applying the macroscopic Maxwell equations in differential form:

$$\nabla \cdot \boldsymbol{D} = \rho_f, \tag{2.1}$$

$$\nabla \cdot \boldsymbol{B} = 0, \tag{2.2}$$

$$\nabla \times \boldsymbol{E} = -\frac{\partial \boldsymbol{B}}{\partial t}, \tag{2.3}$$

$$\nabla \times \boldsymbol{H} = \boldsymbol{J}_f + \frac{\partial \boldsymbol{D}}{\partial t}, \tag{2.4}$$

where $\boldsymbol{E}$ is the electric field, $\boldsymbol{B}$ is the magnetic field, $\boldsymbol{D}$ is the electric displacement, the equivalent magnetic quantity is $\boldsymbol{H}$, ρ_f is the free charge density, and $\boldsymbol{J}$ is the free

current density. $\boldsymbol{E}$, $\boldsymbol{D}$, $\boldsymbol{B}$ and $\boldsymbol{H}$ are related in a dielectric medium by the following relationships:

$$\boldsymbol{D} = \varepsilon_0 \varepsilon_r \boldsymbol{E} \simeq \varepsilon_0 n^2 \boldsymbol{E}, \tag{2.5}$$

$$\boldsymbol{B} = \mu_0 \mu_r \boldsymbol{H} \simeq \mu_0 \boldsymbol{H}, \tag{2.6}$$

where ε_0 and μ_0 are the permittivity and permeability of free space, ε_r and μ_r are the relative permittivity and permeability of a material respectively and n is the refractive index of a material. It is assumed that in a dielectric that $\varepsilon_r \approx n^2$ and $\mu_r \approx 1$. In this dielectric structure there are no free charge or current densities, and the refractive index can be assumed to be piece-wise constant. Maxwell's equations can then be rewritten as:

$$\nabla \cdot \boldsymbol{E} = 0, \tag{2.7}$$

$$\nabla \cdot \boldsymbol{H} = 0, \tag{2.8}$$

$$\nabla \times \boldsymbol{E} = -\mu_0 \frac{\partial \boldsymbol{H}}{\partial t}, \tag{2.9}$$

$$\nabla \times \boldsymbol{H} = \varepsilon_0 n^2(y) \frac{\partial \boldsymbol{E}}{\partial t}, \tag{2.10}$$

where refractive index profile $n(y)$ of the waveguide is defined by

$$n(y) \equiv \begin{cases} n_1 & y > |d/2| \\ n_2 & y \leqslant |d/2| \end{cases} \tag{2.11}$$

where d is the thickness of the core, n_1 and n_2 are the cladding and core refractive indices respectively. With these modifications, Maxwell's equations can be rearranged to form the wave equations

$$\nabla^2 \boldsymbol{E} = \varepsilon_0 \mu_0 n^2(y) \frac{\partial^2 \boldsymbol{E}}{\partial t^2}, \tag{2.12}$$

$$\nabla^2 \boldsymbol{H} = \varepsilon_0 \mu_0 n^2(y) \frac{\partial^2 \boldsymbol{H}}{\partial t^2}. \tag{2.13}$$

Solutions to each component of the electric field vector $\boldsymbol{E} = E_x \boldsymbol{i} + E_y \boldsymbol{j} + E_z \boldsymbol{k}$ and magnetic field vector $\boldsymbol{H} = H_x \boldsymbol{i} + H_y \boldsymbol{j} + H_z \boldsymbol{k}$ are assumed to have the form

$$E_j(y) = \mathcal{E}_j(y) e^{i(\omega t - \beta_j z)}, \tag{2.14}$$

$$H_j(y) = \mathcal{H}_j(y) e^{i(\omega t - \beta_j z)}, \tag{2.15}$$

where $\mathcal{E}_j$ and $\mathcal{H}_j$ are the electric and magnetic field amplitudes in y for axis $j \in \{x, y, z\}$, with angular frequency ω and propagation constant β. Consider the solution of an oscillating electric field aligned to the x-axis by substituting $E_x(y)$ into Equation 2.12, we obtain the ordinary differential equation (ODE)

$$\frac{d^2\mathcal{E}_x}{dy^2} = (\beta^2 - k_0^2 n^2(y))\,\mathcal{E}_x(y), \tag{2.16}$$

where wave number k_0 is defined as

$$k_0 \equiv \frac{\omega}{c} = \frac{2\pi\nu}{c}, \tag{2.17}$$

and

$$\beta \equiv n_{\text{eff}} k_0. \tag{2.18}$$

The solutions to Equation 2.16 can be divided into three parts for the three different layers. Assuming that $\beta < k_0 n$ for the central layer and the $\beta > k_0 n$ for the surrounding layers leads to the general solutions

$$\mathcal{E}_x(y) = \begin{cases} Ae^{-\alpha_{\text{SW}} y} & y > d/2 \\ B\cos(\kappa_{\text{SW}} y) + C\sin(\kappa_{\text{SW}} y) & -d/2 < y \leqslant d/2\,, \\ De^{\alpha_{\text{SW}} y} & y \leqslant -d/2 \end{cases} \tag{2.19}$$

where A, B, C, D, α_{SW} and κ_{SW} are constants to be solved. From the symmetry of the slab waveguide we can see that solutions will be either an even or odd function, allowing us to simplify our analysis to the $\cos(\kappa_{\text{SW}} y)$ and $\sin(\kappa_{\text{SW}} y)$ terms of Equation 2.19 independently. Applying the continuity condition at the boundary $d/2$ to $\mathcal{E}_x$ and $d\mathcal{E}_x/dy$ leads to the following equations

$$Ae^{-\alpha_{\text{SW}}\frac{d}{2}} = B\cos\left(\kappa_{\text{SW}}\frac{d}{2}\right), \tag{2.20}$$

$$A\alpha_{\text{SW}} e^{-\alpha_{\text{SW}}\frac{d}{2}} = B\kappa_{\text{SW}}\sin\left(\kappa_{\text{SW}}\frac{d}{2}\right). \tag{2.21}$$

Taking the ratio of the equations and multiplying by $d/2$ leads to the relation

$$\frac{\alpha_{\text{SW}} d}{2} = \frac{\kappa_{\text{SW}} d}{2}\tan\left(\frac{\kappa_{\text{SW}} d}{2}\right), \tag{2.22}$$

and applying the same analysis to the solution

$$\frac{\alpha_{\mathrm{SW}} d}{2} = -\frac{\kappa_{\mathrm{SW}} d}{2} \cot\left(\frac{\kappa_{\mathrm{SW}} d}{2}\right). \tag{2.23}$$

These transcendental equations cannot be simultaneously solved as they come from orthogonal components to the general solution of $\mathcal{E}_x$. If Equation 2.19 is substituted into Equation 2.16 to obtain

$$\kappa_{\mathrm{SW}}{}^2 = k_0^2 n_2^2 - \beta^2, \tag{2.24}$$

$$\alpha_{\mathrm{SW}}{}^2 = \beta^2 - k_0^2 n_1^2, \tag{2.25}$$

and these can be rearranged into

$$V \equiv \sqrt{\kappa_{\mathrm{SW}}{}^2 d^2 + \alpha_{\mathrm{SW}}{}^2 d^2} = k_0 d \sqrt{n_2^2 - n_1^2} \tag{2.26}$$

where V is called the normalised frequency. This is a dimensionless parameter that completely characterises the entire slab geometry shown in Figure 2.1. This relates κ_{SW}, α_{SW}, n_1 and n_2. Rearranging with Equation 2.22 and Equation 2.23 we obtain the equations

$$\frac{\kappa_{\mathrm{SW}} d}{2} \tan\left(\frac{\kappa_{\mathrm{SW}} d}{2}\right) = \sqrt{\frac{V}{4} - \frac{\kappa_{\mathrm{SW}}{}^2 d^2}{4}}, \tag{2.27}$$

$$-\frac{\kappa_{\mathrm{SW}} d}{2} \cot\left(\frac{\kappa_{\mathrm{SW}} d}{2}\right) = \sqrt{\frac{V}{4} - \frac{\kappa_{\mathrm{SW}}{}^2 d^2}{4}}, \tag{2.28}$$

which providing the even and odd mode solutions respectively parametrised by V. This can be solved graphically as seen in Figure 2.2 by plotting the left hand side (LHS) against the right hand side (RHS) of Equations 2.27 and 2.28. Intercepts between curves represent valid solutions to the wave equation. It can be seen from Equation 2.26 that V and thus the number of solutions to the wave equation increases with the size of the core of the slab, as well as a greater refractive index difference between the core and cladding. From these graphical solutions it can be seen that to achieve a single mode waveguide V must be less than the zero intercept of Equation 2.23 leading to $V \leqslant \pi$.

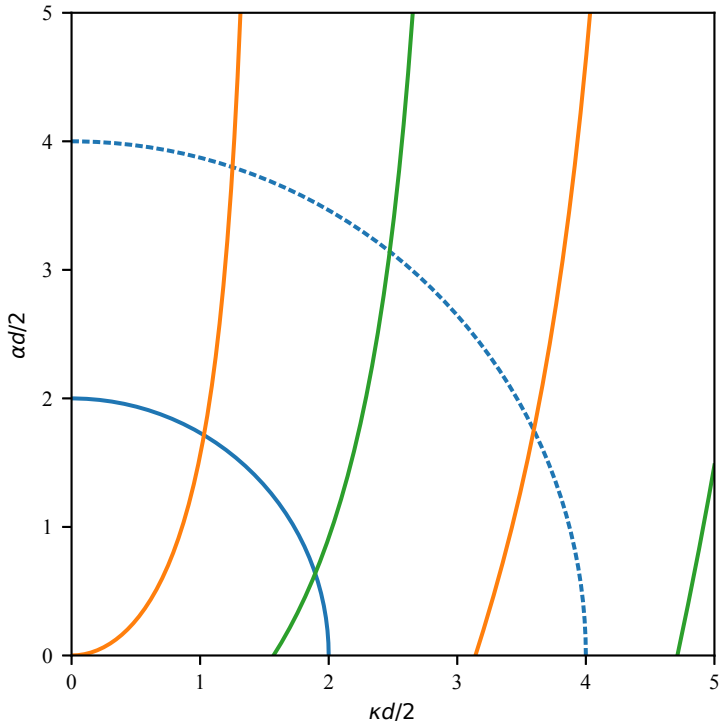

Figure 2.2: Geometric solution to the slab waveguide. The orange is the semi-circle generated by the LHS of Equations 2.27 (even) and green for LHS of Equation 2.28 (odd). The blue solid and dashed lines indicate the curves generated by the RHS Equations 2.27 and 2.28 for values $V = 4$ and $V = 8$ respectively. Intercepts of the blue curves with other curves indicate valid solutions to the wave equation.

To obtain the magnetic field of the waveguide apply Equation 2.9 to the electric field giving

$$\begin{pmatrix} H_x \\ H_y \\ H_z \end{pmatrix} = \begin{pmatrix} -\frac{\beta_x}{\mu_0 \omega} E_x \\ 0 \\ \frac{1}{i\omega\mu_0} \frac{\partial E_x}{\partial y} \end{pmatrix}. \tag{2.29}$$

The mode solved in this waveguide is known as transverse-electric (TE) as the electric field vector has no z-axis component but a small magnetic one. Using the same procedure described above to solve the TE mode solution can be used to determine transverse-magnetic (TM) solution starting with a magnetic field exciting in the x-axis plane. As the TE and TM modes have perpendicular polarisations, a frequent abuse of language and convention in the literature is to refer to the linear polarisation of the electric field to the horizontal and vertical planes as TE and TM respectively.

2.2 Bragg gratings

The external cavities that are considered in this thesis use a Bragg reflector to form part of the overall cavity structure and act as the frequency selective element in the cavity. This section presents a simplified wave vector argument for Bragg gratings to understand their origin. To understand the relationship between wavelength spectrum and the Bragg grating structure, the coupled mode equations are derived that can be used to understand and predict their spectra.

A Bragg grating is a spatially periodic structure of refractive index changes in a dielectric material as depicted in Figure 2.3. Light incident on this structure, normal to the grating periods, undergoes a number of Fresnel reflections at the interfaces between changes of the refractive indices. The light will undergo numerous internal reflections in both the forward and reverse directions. Depending on the light's wavelength, the incident and reflected optical field phases can add up constructively forming a strong reflection at resonance; this wavelength is known as the Bragg wavelength. Off resonance, the light passes almost completely unreflected, as most of the reflected fields interfere constructively and destructively in a quasi-random manner, leading to a total field that is overall very weak in the reverse direction. The design of the Bragg grating's index structure can be engineered to control the spectral features and phase response of the Bragg grating.

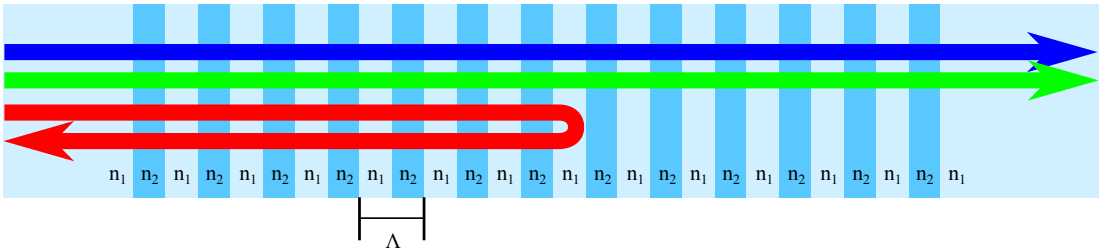

Figure 2.3: Broadband light, incident from the left, indicated by the blue, green and red arrows is selectively reflected. When wavelength of the light and the grating period Λ satisfy the phase matching condition Equation 3.4 it is reflected.

It is this wavelength dependence that makes Bragg gratings so useful as they can be used to make optical bandstop and bandpass filters, the latter when used with a circulator. In realised devices, the material host of the Bragg grating is typically sensitive to a number of environmental physical properties resulting in a change in the response of the Bragg grating, making them ideal for use in sensing applications. Most relevant to this research, Bragg gratings exhibit excellent properties to be used as the feedback reflector in an external cavity diode laser, due to their wavelength dependent reflection

and the ability to tailor that reflection to the design of the cavity. As a result this research utilises Bragg gratings as the essential wavelength dependent reflector the for external cavities. An understanding of Bragg grating theory is required to understand the reflection spectra and features.

2.2.1 The Bragg Condition

The condition at which peak resonance occurs in a Bragg grating is known as the Bragg condition. This condition is fulfilled when the wave vectors of the incident optical field $\boldsymbol{k}_i$, and the wave vector of the reflected optical field $\boldsymbol{k}_r$, relate to the Bragg grating k-vector $\boldsymbol{K}_{\mathrm{Br}}$ with the relation

$$\boldsymbol{k}_i - \boldsymbol{k}_r = \boldsymbol{K}_{\mathrm{Br}}, \tag{2.30}$$

where the vectors $\boldsymbol{k}_i$ and $\boldsymbol{k}_r$ indicate the incident and reflected waves of a waveguide with effective index n_{eff}, $\boldsymbol{k}_q$ is defined as

$$\boldsymbol{k} \equiv n_{\mathrm{eff}} k_0 \hat{\boldsymbol{u}}_q, \tag{2.31}$$

where $q \in \{i, r\}$ and the Bragg grating vector is defined by

$$\boldsymbol{K}_{\mathrm{Br}} \equiv \frac{2\pi}{\Lambda}. \tag{2.32}$$

where Λ is the grating period. If we consider the case of collimated light incident on a grating, that is parallel to the Bragg grating vector, causing a parallel but counter propagating reflected wave leads to the Bragg condition

$$\lambda_{\mathrm{Bragg}} = 2 n_{\mathrm{eff}} \Lambda, \tag{2.33}$$

where we have redefined λ_{Bragg} as the phase matched wavelength.

2.2.2 Coupled mode theory

The Bragg condition from Equation 2.33 only defines the wavelength point of peak reflection of the Bragg grating for an unchirped weak grating. In reality a Bragg grating has a finite spectral width, and can be fabricated with arbitrary chirp profiles leading to

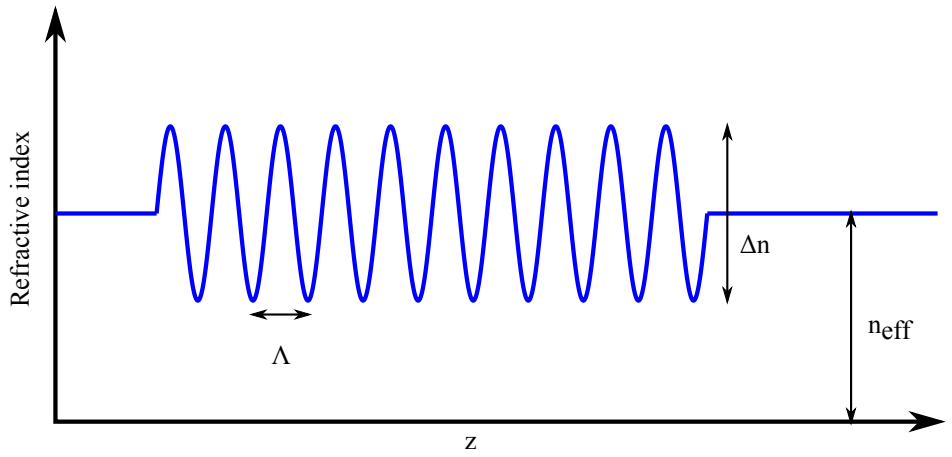

Figure 2.4: An example of an index profile that can be solved using coupled mode theory.

more complex spectral responses. There are a number of methods that can be used to predict and understand the spectral responses of these gratings. On of these methods is known as coupled mode theory. This theory models modes that have been solved by the wave equation and looks at the coupling between specific modes in the presence of a perturbation such as a Bragg grating. In this situation a Bragg grating couples light between forward and backward confined modes of a waveguide and can be extended to multimode waveguides. The derivation of the coupled mode equations given in this section is based off methods covered by [5]–[7] but has adapted to the buried single mode UV-written waveguides produced by the direct UV-writing method and demonstrate some of basic spectral responses produced.

The effective index of a single mode waveguide can be described by

$$n_{\text{eff}}(\boldsymbol{r}) \equiv \overline{n}_{\text{eff}} + \Delta n(\boldsymbol{r}), \tag{2.34}$$

where $\overline{n}_{\text{eff}}$ is the steady state effective index of the waveguide itself and $\Delta n(\boldsymbol{r})$ is defined by

$$\Delta n(\boldsymbol{r}) \equiv \delta n(\boldsymbol{r}) \cos\left(\frac{2\pi}{\Lambda} + \phi(z)\right), \tag{2.35}$$

where δn is the sinusoidal amplitude component of the effective index profile and ϕ is the chirp profile. The polarisation is related linearly with $\varepsilon_r(\boldsymbol{r})$ which can be approximated by $\varepsilon_r \simeq n^2$. We can therefore write the relative permittivity assuming $\Delta n n \ll \overline{n}_{\text{eff}}$

$$\begin{aligned} \varepsilon_r(\boldsymbol{r}) &= (\overline{n}_{\text{eff}} + \Delta n(\boldsymbol{r}))^2 \\ &= \overline{n}_{\text{eff}}^2 + 2\overline{n}_{\text{eff}}\Delta n(\boldsymbol{r}) + \Delta n^2(\boldsymbol{r}) \\ &\approx \overline{n}_{\text{eff}}^2 + 2\overline{n}_{\text{eff}}\Delta n(\boldsymbol{r}), \end{aligned} \tag{2.36}$$

From this expansion we can consider the problem a perturbation to a steady state relative permittivity. Therefore, the overall polarisation $\boldsymbol{P}$ induced by the electric field $\boldsymbol{E}$ can therefore be defined as

$$\boldsymbol{P}(\boldsymbol{r}) \equiv P_{\text{unpert}} + P_{\text{Br}} \tag{2.37}$$

where

$$\boldsymbol{P}_{\text{unpert}} \equiv \varepsilon_0 n_{\text{eff}}^2 \boldsymbol{E} \tag{2.38}$$

$$\boldsymbol{P}_{\text{Br}} \equiv 2\varepsilon_0 \overline{n}_{\text{eff}} \Delta n(\boldsymbol{r}) \boldsymbol{E} \tag{2.39}$$

$$. \tag{2.40}$$

Rewriting the the wave equation of the electric field in matter in terms of the polarisation leads us to

$$\underbrace{\nabla^2 \boldsymbol{E} = \mu_0 \varepsilon_0 \frac{\partial^2 \boldsymbol{E}}{\partial t^2} + \mu_0 \frac{\partial^2 \boldsymbol{P}_{\text{unpert}}}{\partial t^2}}_{\text{Unperturbed wave equation}} + \underbrace{\mu_0 \frac{\partial^2 \boldsymbol{P}_{\text{Br}}}{\partial t^2}}_{\text{Perturbation}}, \tag{2.41}$$

The unperturbed part of Equation 2.41 is an equivalent way of representing the wave equation described in Equation 2.12. The solutions for a dielectric waveguide, for the unperturbed wave equation indicated in Equation 2.41 can be written as

$$\begin{aligned} E(\boldsymbol{r},t) = \frac{1}{2} \sum_u \left[M_u(z) \mathcal{E}_u(x,y) e^{i(\omega t - \beta_u z)} + N_u(z) \mathcal{E}_u(x,y) e^{i(\omega t + \beta_u z)} \right] \\ + \int_0^\infty M_\rho(z) \mathcal{E}_\rho e^{i(\omega t - \beta_\rho z)} + N_\rho(z) \mathcal{E}_\rho e^{i(\omega t + \beta_\rho z)} \, d\rho, \end{aligned} \tag{2.42}$$

where $M_u(z)$ and $N_u(z)$ are the envelope functions of the forward and backward propagating modes in z of the uth confined mode where u is an integer, ρ indexes the cladding modes where ρ is a continuous number, $\mathcal{E}_u$ and $\mathcal{E}_\rho$ are the transverse field distributions. Only a single mode waveguide will be considered and coupling into cladding modes will be assumed to be negligible and therefore disregarded. The factor $1/2$ is necessary as we are using complex forms of the fields and carrying the conjugate implicitly. Substituting Equation 2.42 into Equation 2.41, and considering only a single mode, we can identify that the group

$$\nabla^2 \left(\mathcal{E}(x,y) e^{i(\omega t - \beta z)} \right) - \mu_0 \varepsilon_0 \overline{n}_{\text{eff}}^2 \frac{\partial^2}{\partial t^2} \left(\mathcal{E}(x,y) e^{i(\omega t - \beta z)} \right) = 0, \tag{2.43}$$

as it is a solution to the homogeneous wave equation. Then by applying the slowly varying wave approximation ($\partial^2 M_u/\partial z^2 \ll \beta_u \, \partial M_u/\partial z$) we arrive at

$$-i\beta\frac{dM}{dz}\mathcal{E}(x,y)e^{i(\omega t-\beta z)} + i\beta\frac{dN}{dz}\mathcal{E}(x,y)e^{i(\omega t+\beta z)} = \mu_0\frac{\partial^2 \boldsymbol{P}_{\mathrm{Br}}}{\partial t^2}. \tag{2.44}$$

The time averaged Poynting vector $\langle S_z \rangle$ can be written for a TE solution as

$$\langle S_z \rangle = \frac{1}{2}\iint_{-\infty}^{\infty} E_x H_y^* \, dx \, dy. \tag{2.45}$$

For convenience we set the value $\mathcal{E}$ such that the z-component of the time averaged Poynting vector is 1 W leading to the normalisation condition

$$-\frac{\beta}{2\mu_0\omega}\iint_{-\infty}^{\infty}\mathcal{E}(x,y)\mathcal{E}^*(x,y)\,dx\,dy = \delta(n,m), \tag{2.46}$$

where $\delta(n,m)$ is the Kronecker delta function. To remove the $\mathcal{E}(x,y)$ terms from the LHS of Equation 2.44 we utilise the normalisation condition Equation 2.46, by multiplying Equation 2.44 by a test field $\mathcal{E}(x,y)^*$ and then integrating over the transverse area of the mode to give

$$\frac{dM}{dz}e^{i(\omega t-\beta z)} - \frac{dN}{dz}e^{i(\omega t+\beta z)} = -\frac{i}{2\omega}\iint_{-\infty}^{\infty}\frac{\partial^2 \boldsymbol{P}_{\mathrm{Br}}}{\partial t^2}\mathcal{E}^*(x,y)\,dx\,dy. \tag{2.47}$$

Substituting Equation 2.39 into Equation 2.47 and expanding the electric field $E(t)$ gives

$$\begin{aligned}&\frac{dM}{dz}e^{-i\beta z} - \frac{dN}{dz}e^{i\beta z}\\ &= i\omega\varepsilon_0\overline{n}_{\mathrm{eff}}\cos\left(\frac{2\pi}{\Lambda}z+\phi(z)\right)\left[M(z)e^{-i\beta z}+N(z)e^{i\beta z}\right]\iint_{-\infty}^{\infty}|\mathcal{E}^2(x,y)|\delta n(\boldsymbol{r})\,dx\,dy.\end{aligned} \tag{2.48}$$

From this equation we can see that all terms contain rapidly oscillating factors, however some groups of terms oscillate in phase together. Taking the synchronous groups out into separate equations is called the *synchronous approximation* [8]. This is done by multiplying Equation 2.48 by $e^{i\beta z}$, then applying the rotating wave approximation to eliminate remaining rapidly oscillating terms. This process is applied again to the same

equations by multiplying with $e^{-i\beta z}$ thereby providing the two coupled mode equations

$$\frac{dM}{dz} = i\kappa N(z)e^{i[\Delta\beta z - \phi(z)]}, \tag{2.49}$$

$$\frac{dN}{dz} = -i\kappa M(z)e^{-i[\Delta\beta z - \phi(z)]}, \tag{2.50}$$

where

$$\Delta\beta \equiv 2\beta - \frac{2\pi}{\Lambda}, \tag{2.51}$$

$$\kappa \equiv \frac{\omega\varepsilon_0\overline{n}_{\text{eff}}}{2}\iint_{-\infty}^{\infty}|\mathcal{E}^2(x,y)|\delta n(\boldsymbol{r})\,dx\,dy. \tag{2.52}$$

From Equations 2.49 and 2.50 it can be seen that maximum coupling is achieved when the argument of the rapidly rotating terms is zero. This leads to the equation

$$2\beta = \frac{2\pi}{\Lambda} + \phi(z). \tag{2.53}$$

For an unchirped grating where the chirp parameter $\phi(z) = 0$, we can see that this is simply solved to give us the Bragg condition Equation 2.33 we solved earlier using a vector argument.

To eliminate the rapidly rotating complex terms the equation is recast using new variables that encapsulate the rapidly rotating terms, simplifying the equations and making them more efficient to solve numerically. The new variables are defined $R_{\text{cm}}(z) \equiv M(z)\exp(i\frac{1}{2}[\Delta\beta z - \phi(z)])$ and $S_{\text{cm}}(z) \equiv N(z)\exp(-i\frac{1}{2}[\Delta\beta z - \phi(z)])$ and then rewriting Equations 2.49 and 2.50 in terms of $R_{\text{cm}}(z)$ and $S_{\text{cm}}(z)$ gives the final form of the coupled mode equations

$$\frac{dR_{\text{cm}}}{dz} = -i\sigma R_{\text{cm}}(z) + i\kappa S_{\text{cm}}(z), \tag{2.54}$$

$$\frac{dS_{\text{cm}}}{dz} = -i\kappa R_{\text{cm}}(z) + i\sigma S_{\text{cm}}(z), \tag{2.55}$$

where

$$\kappa(z) \equiv \frac{1}{2}\Delta\beta - \frac{1}{2}\frac{d\phi}{dz}. \tag{2.56}$$

2.2.2.1 Solving the coupled mode equations

There are a number of different approaches to solving the coupled mode equations (Equation 2.54). For a grating whose refractive index modulation amplitude is constant, and the grating fringes are constant period, can be solved analytically. However for many gratings where an arbitrary apodisation function is utilised, where the apodisation function refers to the refractive index modulation amplitude, prevents the grating from being solved analytically. In these situations the apodised grating can be discretised into short uniform gratings of different strengths to approximate the shape of the apodisation function. Another approach, and the approach used in this thesis, is to solve the equations by numerically integrating them.

Initially it may seem that these equations are most appropriately solved as boundary value equations. However if we recognise that we are only interested in the reflectivity and transmission of these gratings we can solve the equations as an initial value problem. Casting the problem this way allow us to use more efficient numerical integrators such as the Runge-Kutta method for initial value problems.

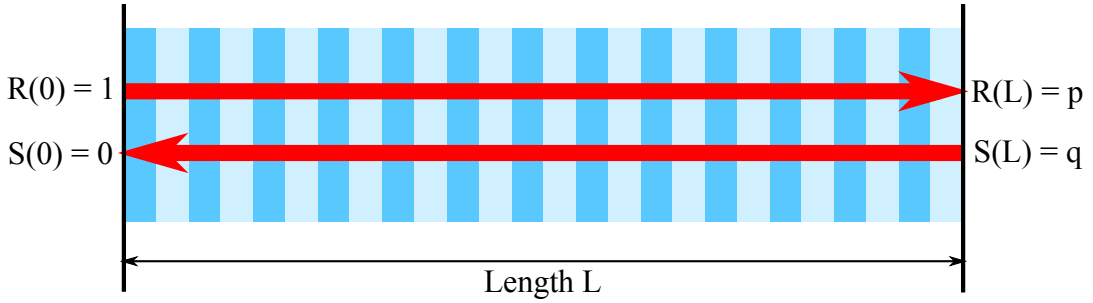

Figure 2.5: Index profile of grating showing boundary conditions used to solve the coupled mode equations as an initial value problem.

Figure 2.5 illustrates how this can be solved as an initial value problem. If we consider a forward travelling mode incident on a Bragg grating of length where $R_{\mathrm{cm}}(0) = 1$ and a reverse travelling wave where $S_{\mathrm{cm}}(0) = 0$. Solving the modes to obtain $R_{\mathrm{cm}}(L) = p$ and $S_{\mathrm{cm}}(L) = q$, the power reflected can be determined from $|p/q|^2$ and the power transmitted from $1 - |p/q|^2$. Figure 2.6 shows some examples of the reflection spectra of solved gratings. It can be seen that the apodisation function has a profound effect, in the case of a Gaussian, the side lopes are suppressed significantly at the expense of a lower reflectivity and a broadening of the central lobe.

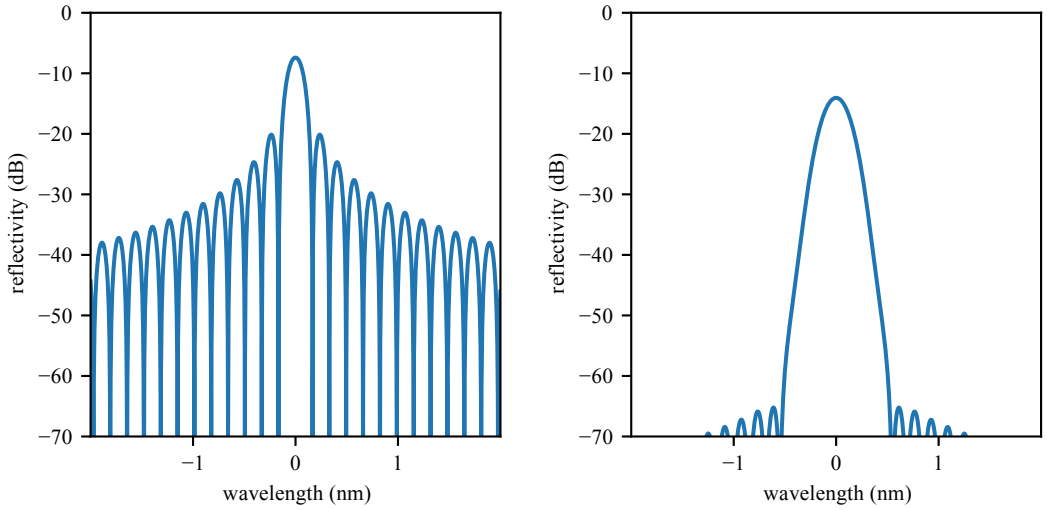

(a) An unapodised or uniform grating.

(b) A Gaussian apodised grating.

Figure 2.6: Coupled mode equations solved using the Runge-Kutta method. Both gratings were length 5 mm, with δn is 4.5×10^{-5} and centre wavelength 1550 nm.

2.3 Semiconductor gain chips

Semiconductor gain devices or chips used in external cavity diode lasers (ECDLs) operate almost identically to diode laser chips with minor differences. Diode lasers are devices that use injected carriers, namely electrons and holes, in semiconductors to achieve population inversion allowing for amplification by stimulated emission. As injected carriers are used this effectively means the devices are pumped using a simple electrical current making these devices highly convenient in many applications. The primary difference of gain chips to diode lasers is there is built-in optical feedback and therefore it is unable to lase on its own. In this thesis multiple quantum well gain chips are used as the optical amplifier in all ECDL devices and so a brief qualitative outline of semiconductor band theory pertaining to gain chips is presented in this section. A more detailed description of band theory and semiconductor lasers can be found in these references [9]–[11].

2.3.1 Band theory of semiconductors

The distinction of semiconductors from conductors and insulators can be understood by considering what is known as their *band* structure. An individual atom has discrete energy levels that its electrons can occupy that are determined from solutions to

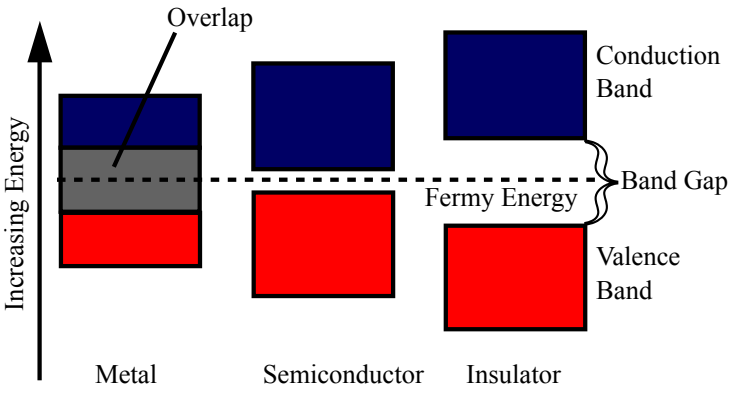

Figure 2.7: Band-gap diagram of metals, semiconductors and insulators. Metals have high conductivity due to overlapping conduction and valance bands, whereas insulators have very large band gaps. Diagram modified from inductiveload used under CC BY-SA 2.5.

Schrödinger's equation. If we consider multiple identical atoms covalently bonded into a crystal lattice, the number of available energy levels multiplies with the number of atoms in the system. These new energy levels do not occupy the same energy levels but detune and band around the energies of a 1-atom system. At macroscopic scales these bands of energy levels can be modelled as a continuum of states simplifying their analysis.

The valance and conduction bands are the bands of most interest in semiconductors as these govern most of the properties of interest in semiconductor devices. The valance band is defined as the highest energy band that is fully occupied with electrons at 0 K. The conduction band is similarly defined as the lowest energy band that is fully occupied with holes (absences of electrons) at 0 K. At higher temperatures electron carriers are excited from the valence band to the conduction band leaving a vacancy known as a hole carrier, a type of quasiparticle, in the valance band. The statistics of these excitations can be described using the Fermi-Dirac distribution. In conductors the bands overlap so that carriers (holes and electrons) can easily transition between adjacent energy levels when excited by a static electric field. Semiconductors occur when the bands are separated by a relatively small energy gap known as the band gap; as there are still a small number of thermally excited electrons in the conduction band (and holes in the valence band), the material is still able to conduct albeit with higher resistance. Insulators are materials that have very large band gaps such that virtually none of the carriers have been excited across the band leaving few adjacent transitions available for electrical conduction. These material types are indicated in Figure 2.7

Photons can excite electrons from an occupied state to a vacant state. To satisfy laws of conservation of energy and momentum, the difference between the two energy levels

involved must exactly match the energy and momentum of the photon. To consider this we must observe the Energy momentum diagram of two different types semiconductors Figure 2.8.

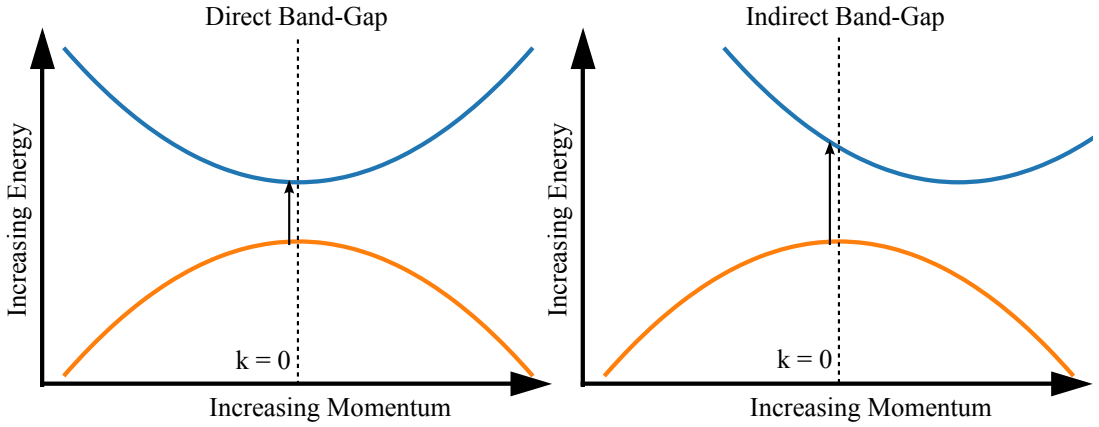

(a) In direct semiconductors, the momentums of the energy minima and maxima of the conduction and the valance bands respectively are identical.

(b) In indirect semiconductors, the momentums of the energy minima and maxima of the conduction and the valance bands respectively are different.

Figure 2.8: Energy-momentum plots of direct and indirect semiconductors.

Direct band gap semiconductors are defined by having identical energy minima and maxima of the conduction and valance bands respectively. Indirect band gaps have different energy minimas and maximas. Optical transitions at the band gap energy are much more likely in direct semiconductors as photons have a very small momentum compared to their energy so easily satisfy conservation laws for transitions in direct semiconductors. Indirect semiconductors usually require both a photon and phonon interaction to satisfy the conservation laws, phonons have comparatively much higher momentums compared to their energy; as both a photon and a phonon are needed in this kind of interaction it is significantly less likely to occur.

Most optical semiconductors devices are fabricated using direct semiconductor materials due to the energy-momentum relationship. Most direct semiconductor materials are group III-V compound semiconductor such as GaAs and InP. As direct band gap materials can efficiently absorb and generate photons they are always used to make light emitting diode (LED)s and lasers.

2.3.2 Heterostructures and quantum wells

The band structure of an optoelectronic device can be engineered in order to confine electrons to desired parts of the device, promote population inversion conditions, and

make radiative recombination (the combination of an electron and hole pair carriers across the band gap) more likely. This usually involves engineering the bands to trap electrons within the active region of the device at an intended set of energy states. For efficient laser and gain devices it is also important to engineer the refractive index of semiconductors to confine light to the active region, the region where radiative recombination occurs, maximising the overlap of the optical mode and the active region.

To this end one of the most ubiquitous optoelectronic band structures used in diode lasers is known as the double heterodyne structure. This type of device sandwiches a lower band gap material between two higher band gap materials. The resulting bands show a drop in potential in the active region of the device forming a potential well. Injected electrons (and holes) will be trapped in the potential well in a small volume of material rather than diffusing elsewhere and recombining. Trapping of electron and holes in the this small region leads to a large population inversion necessary for laser devices. Additionally this type of structure means generated photons experience a higher refractive index in the active region than outside leading to confinement of the optical mode providing excellent overlap with the active region.

As mentioned before, band theory models the densely packed states as a continuum, however the states within a band are not uniformly distributed across the band. Bands however can be described by a density of states distribution function as seen in Figure 2.9. For low threshold and efficient lasing a high density of states needs to exist at the operating photon energy. In bulk lasers such as a standard double heterostructure laser the density of states increases approximately with the square root of the energy level as seen in Figure 2.9. As the device has carriers injected the lowest energy states of the conduction band have to fill up first. These states are too low density to support laser action but must be filled first before the states of the operating laser photon energy are filled.

Quantum wells are a structure that can greatly improve the efficiency of semiconductor amplifiers. These structures are a potential well whose width is similar to the de Broglie wavelength thus confining electrons to a 2-dimensional plane. This alters the density of states function favourably by making the function step-wise with energy, also shown in Figure 2.9. As there is a high density of states at the band gap edge, injected carriers immediately contribute to lasing action improving the laser threshold and efficiency, additionally the quantum well attracts a higher concentration of carriers. By comparison, in bulk semiconductors, the density of states at the band edge is zero. A final advantage of these structures is they allow tuning of the device bandgap width

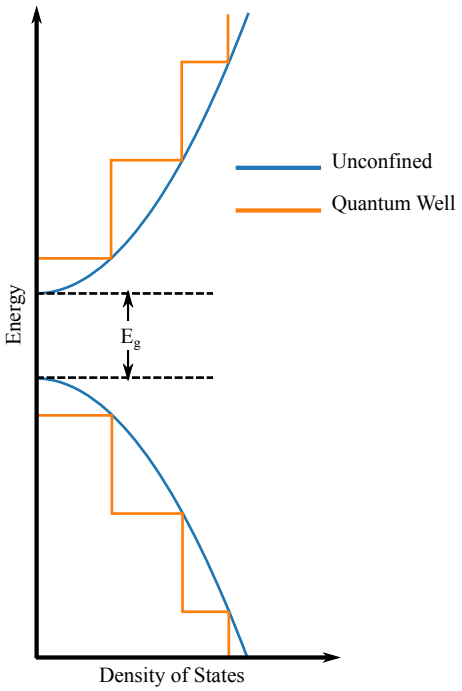

Figure 2.9: Density of states plot comparing the density of states in bulk semiconductor to quantum well structure that confines electrons to a plane.

by varying the width of the quantum well moving the steps in the stair-case function. These structures are implemented as a type of heterostructure by wedging a narrower direct band gap material between two wider band gap materials. As the quantum well structures are so thin they do not provide a large active area so there is relatively small overlap with the device's optical mode. To optimise the efficiency of these devices multiple quantum wells can be implemented in series improving the overlap with the optical mode and compounding the the number of available states at the band edge improving the device efficiency, these devices are known as multiple quantum wells (MQW). The quantum wells in a MQW device must be separated with enough width to prevent quantum tunnelling between wells (Figure 2.10).

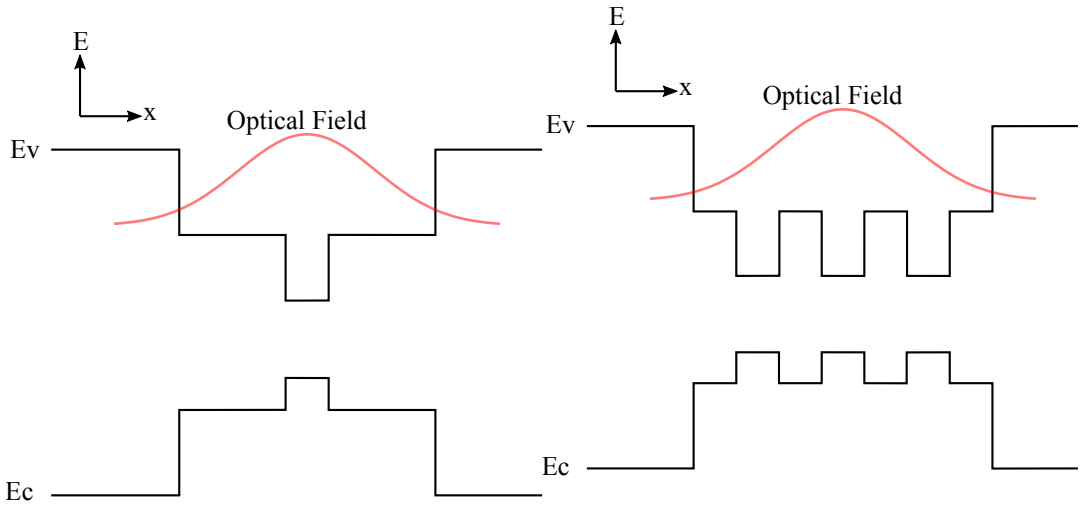

(a) A single quantum well device. The quantum well only has limited overlap with the optical mode.

(b) A multiple quantum well device. Multiple quantum wells allow greater overlap with optical mode as well as compounding the number of states available at the band edge.

Figure 2.10: Illustrations of band structures of single and multi quantum well structures.

2.4 Laser noise

Like any engineered system, noise is an important attribute in lasers as it affects the performance of the system in various applications, for example in telecommunications it will directly affect the bit error rate (BER). Typically, modulation schemes will employ phase or amplitude based modulation, or both in the case of quadrature amplitude modulation (QAM). This emphasises the importance of properly characterising the noise properties in a laser as this will limit its applications.

In this section the mathematical definitions and assumptions needed to analyse laser noise are given. Relative intensity noise will be defined and some of the physical processes outlined. Finally phase noise and linewidth will considered, their mathematical relationship defined, and an outline of some of the underlying physical processes described.

2.4.1 Mathematical formulation

A laser can be considered as the optical analogue of an electronic radio frequency (RF) oscillator. Indeed the analysis techniques used on electronic oscillators have been adopted by the optics community for the analysis of CW laser noise. The laser is treated

simply as an electronic oscillator that exhibits fluctuations of its wave amplitude and fluctuations of its phase oscillations.

In this analysis, it is worth defining some mathematical quantities and definitions to rigorously and meaningfully model laser or oscillator noise. For convenience of analysis the noise present in a signal will be considered a random walk that is wide-sense stationary and ergodic. Qualitatively, a wide-sense stationary signal is one where the expectation of the process and its autocorrelation is time independent, where the autocorrelation function $R_x(\tau)$ is defined by

$$R_x(\tau) \equiv \int_{-\infty}^{\infty} x(t)x(t+\tau)\,dt. \tag{2.57}$$

The ergodicity requirement, refers to ability to estimate a random process' statistical moments from a single instance of that random process. As it happens these are quite accurate assumptions to make about real world processes and the processes that will come under consideration in this research. Frequently throughout this thesis a random process will be analysed through its power spectral density (PSD) function. This function provides the expected power distribution with frequency f of the random process. As such the PSD R_x of a random process $x(t)$ is defined as

$$S_x \equiv \lim_{T\to\infty} \mathbb{E}\left[\frac{1}{T}\left|\int_0^T x(t)e^{2\pi i f t}dt\right|^2\right], \tag{2.58}$$

where $\mathbb{E}$ is the expectation operator, t is time, f is frequency, and T is the integration time. Typically the PSD is given in units of Hz^{-1}, representing the power contained in a 1 Hz idealised bandpass filter.

In practice there are a number of ways in which the PSD in equation Equation 2.58 can be estimated. For example, a radio-frequency Spectrum-Analyzer (RFSA) sweeps a bandpass filter across a given noise electrical signal producing a PSD. An RFSA will rarely have a bandpass filter with 1 Hz bandwidth, however this can be corrected to produce a more accurate estimate. For most of the signals in this research the signal is a digitally sampled signal and is digitally post processed, utilising the fast Fourier-transform (FFT), to produce an estimated PSD.

When considering the analysis of noise from an optical signal from a single frequency laser, such as the lasers considered in this thesis, at any point in space the optical field $E(t)$ can be modelled as

$$E(t) = E_0[1+\alpha(t)]\cos(2\pi\nu_0 t + \phi(t)), \tag{2.59}$$

where ν_0 is central optical frequency, $\alpha(t)$ and $\phi(t)$ are instantaneous amplitude and phase fluctuations. It is these two terms that contribute to the noise of the optical field and are what governs its suitability for various applications where noise is a limiting factor. Lasers, in addition to these properties also exhibit polarisation instability, however this will not be considered as this is usually only a significant issue in vertical cavity surface emitting lasers (VCSELs) where their polarisation selectivity is weak. In contrast, for edge emitting devices that are considered here, exhibit a strong gain dependence on the polarisation resulting in a highly polarised output.

The standard metric that is given for fluctuations in intensity ($\alpha(t)$) is known as relative intensity noise (RIN). Phase fluctuations ($\phi(t)$) uses several metrics, the two most common given is the phase noise PSD, and more commonly the linewidth. It is these noise metrics that will be outlined in this section.

2.4.2 Relative intensity noise

Intensity noise is an important limiting properties for many laser applications; for example in amplitude modulation schemes for telecommunications the intensity noise directly affects the resolvable resolution and thus the number of distinct quantisation levels that the laser amplitude can be divided into.

The intensity signal of a laser can be expressed by

$$\mathcal{P}(t) = \overline{\mathcal{P}} + \delta\mathcal{P}(t), \tag{2.60}$$

where $P(t)$ is the laser power output in time, $\overline{\mathcal{P}}$ is the mean optical power output and $\delta\mathcal{P}(t)$ is the additive optical intensity noise in time t with a mean of 0.

The most common metric of intensity noise for a single frequency laser is given by a RIN PSD where the noise power PSD is normalised to the square of the average power and is therefore defined as

$$\text{RIN} \equiv \frac{R_{\delta i}(f)}{\overline{I_{\text{pd}}}} = \frac{R_{\delta\mathcal{P}}(f)}{\overline{\mathcal{P}}}, \tag{2.61}$$

where $S_{\delta i}$ is the PSD of the photocurrent noise with frequency f, $\overline{I_{\text{pd}}}$ is the mean photocurrent, $S_{\delta\mathcal{P}}$ is the PSD of the additive *optical power* noise, and $\overline{\mathcal{P}}$ is the mean optical power. The RIN is usually given in units of dBc/Hz. A point of confusion is how the RIN is presented since the noise PSD measures the spectral density of the square of

the optical noise power. This is done for convenience as typically the measurement is performed by using a RFSA to measure the spectrum of the generated photocurrent.

There are several physical origins of intensity noise, including spontaneous emission noise from the laser gain-medium itself, and shot noise introduced from the quantised nature of the optical field. These effectively act as white noise sources that introduce small signal modulation to the cavity photons and carriers, leading to noise features determined by the small signal response of the laser dynamics, usually producing a strong noise feature at the relaxation oscillation resonance. $1/f$ noise found at lower frequencies has been attributed in lasers to mode partition noise, which is most significant in lasers that have other competing modes, where power fluctuates between the active modes [12]. These noise effects are more prominent noise in diode lasers without external cavities, including distributed Bragg reflector (DBR) and distributed feedback (DFB) as they often have a lower side-mode suppression-ratio (SMSR) and a stronger relaxation oscillation peak due to the short cavities compared to ECDLs.

In external cavity diode lasers, these noise features have been observed to be suppressed. This suppression often includes the reduction of the relaxation oscillation resonance that is additionally often shifted to much higher frequencies >2 GHz [13], [14], similar behaviour has been shown in simulated feedback regimes [15]. The more dominant sources of noise often come from vibrations and thermal expansion from changes in the environment. This has led to great efforts to isolate external cavity diode lasers from environmental effects. In some extreme examples ECDLs for use in optical clocks have combined measures such as encapsulation in a solid rigid shell, vibration isolation, Invar components, thermal stabilisation, and vacuum chambers [13], [16].

The noise and instabilities from optical feedback is important as many applications may require immunity to this kind of noise for example, laser diodes used in optical disk drives get back-reflections from the disk. These form unwanted external cavity modes, that can cause significantly greater fluctuations between competing modes [12], [17]. These sources of noise can be solved simply through sufficient isolation often as high as >50 dB, which can be achieved using Faraday isolation.

2.4.2.1 Shot noise limit

At high frequencies, usually higher than the relaxation oscillation resonance, the RIN is often limited by the shot noise limit also known as the standard quantum limit. This limit arises from the discrete nature of photons and it is also encountered in electronics due to the discretisation of charge. The optical power can be visualised as a train of

travelling photons. When incident through a partially reflective surface, for example, the train must be partitioned into photons that were either transmitted or reflected. This partitioning, if assumed to be uniformly random, leads to a Poisson process. In the case of a laser's output coupler, the mean number of transmitted photons and variance is the average power $\overline{\mathcal{P}}$, leading to a shot noise PSD of

$$S_P = 2h\nu\overline{\mathcal{P}}\Delta f. \tag{2.62}$$

Where Δf is the noise bandwidth. Then using the definition of RIN this gives

$$\mathrm{RIN}_{\mathrm{shot}} = \frac{2h\nu\Delta f}{\overline{\mathcal{P}}}. \tag{2.63}$$

An alternative derivation that uses more rigorous quantum mechanical argument to describe the shot noise or partitioning noise is given by [18].

2.4.3 Linewidth and phase noise

Linewidth and phase noise are two intimately related metrics that are both determined entirely from the $\phi(t)$ term found in Equation 2.59. For applications that utilise lasers in interferometers or spectroscopy the characterisation of $\phi(t)$ can determine the capability of laser for application. In this section, the fundamental source of linewidth will be outlined, the effects of external feedback, and other sources of instability will be covered, finally a discussion of using the phase noise PSD as a comprehensive measure of the linewidth and its relationship to fundamental linewidth.

2.4.3.1 The Schawlow-Townes linewidth

The linewidth of the laser has been the traditional metric for determining the phase fluctuations $\phi(t)$. When a laser's spectral line is viewed using an optical spectrum analyzer (OSA) the laser might appear as a perfectly monochromatic line within the limits of the OSA resolution. In reality, with arbitrarily good resolution, a laser "line" would in fact have a shape and finite width, its linewidth. Though stimulated emission generates photons with the exact same phase and direction as the incident field, the presence of spontaneous emission perturbs the field leading to a quantum limit on the linewidth.

The first theory of quantum limited laser phase noise and linewidth developed before even the first optical laser is known as the Schawlow-Townes linewidth [19]. It was found that this quantum limit produced a line shape function that was Lorentzian in shape.

$$\delta\nu_{\mathrm{ST}} = \frac{h\nu\beta L_{\mathrm{tot}} T_{\mathrm{oc}}}{2\pi\tau_{\mathrm{rt}}\mathcal{P}_{\mathrm{out}}}, \tag{2.64}$$

where $\delta\nu_{\mathrm{ST}}$ is the full-width at half-maximum (FWHM) of the resulting Lorentz function, ν is the frequency of the laser, L_{tot} is the total losses, T_{oc} is the output coupler transmission, τ_{rt} is the resonator round trip time, and $\mathcal{P}_{\mathrm{out}}$ is the output power of the laser.

In reality it is very difficult to measure the Schawlow-Townes limit of a laser due to other stronger noise sources on the laser noise. In addition, it was later found by Henry that in diode lasers the Schawlow-Townes limit is enhanced due to the coupling between the diode laser gain and refractive index [20]. A spontaneous emission event would change the concentration of photons within the cavity. This event perturbs the laser cavity power away from steady state, in response the laser attempts to restore the cavity power back, which is reflected by a change of the laser's gain. The coupling between gain and refractive index in the laser gain medium leads to an additional change of refractive index inducing a phase shift to the overall laser field. This phase perturbation has no restoring force unlike the intensity, so the phase of laser's optical field undergoes a random walk. The relationship between the gain and the refractive index of the laser gain medium is expressed by

$$\alpha \equiv \frac{dn}{dn'}, \tag{2.65}$$

where n' is the imaginary index and accounts for the gain of the cavity. Taking this coupling effect into account, the modified Schawlow-Townes limit changes to [20]

$$\delta\nu_{\mathrm{ST}} = \frac{h\nu\beta L_{\mathrm{tot}} T_{\mathrm{oc}}}{4\pi\tau_{\mathrm{rt}}\mathcal{P}_{\mathrm{out}}(1+\alpha^2)}, \tag{2.66}$$

where α is the linewidth enhancement factor that accounts for the relationship between gain and refractive index. Accounting for this coupling between gain and refractive index has given much better agreement with experiment. However there are still other factors that often exaggerate the linewidth beyond what is typically measured. When the Lorentzian linewidth is measured experimentally it is often referred to in the literature as the *fundamental linewidth* or *intrinsic linewidth*.

2.4.3.2 External feedback effects

Weak optical feedback also has a huge impact on the linewidth of a diode laser. Diode lasers can be sensitive to feedbacks > -50 dB of the output. This suggests that even in a pigtailed laser, using clean and well polished flat facet fibres with return losses as low as 50 dB, can be too high. Depending on the amount of optical feedback and the phase, a weak optical feedback can result in either a narrowed or broadened linewidth. A number of behaviour regimes have been observed for a laser receiving weak optical feedback [21], [22]. If designed properly, weak optical feedback can result in significantly reduced linewidths. Uncontrolled optical feedback from external components motivates the use for properly isolating the laser using a Faraday isolator.

However strong optical feedback, such as in an external cavity diode laser utilising an anti-reflection coated facet, shows improved stable linewidths. From Equation 2.66 the round trip time of a diode laser will be proportional to cavity length L_a. If the diode laser has an anti-reflection coating applied to one facet and its length extended by an external cavity of length L_{ext}, this will result in a linewidth reduction according to

$$\delta\nu = \delta\nu_0 \frac{\delta\nu'}{\Delta L_a} \times \frac{\Delta L_a}{\delta\nu} = \frac{L_a^2}{(L_a + L_{ext})^2}, \tag{2.67}$$

where $\delta\nu_0$ represents the original linewidth of diode laser, and $\delta\nu$ is narrowed linewidth [9]. From Equation 2.67 it is clear that the lengthening of the cavity will result in a significant reduction in the linewidth. For a gain-chip that is length L_a =1 mm and an external cavity that is length L_{ext} =10 mm the reduction in the linewidth would be ~120. Laser diodes on their own typically have linewidths of MHz, so a diode laser with a 1 MHz linewidth in its own right, if incorporated into an 10 mm long external cavity with an anti-reflection coating, it will have a linewidth ~8 kHz.

A longer cavity also reduces the sensitivity of the cavity to variations in its length. Such variations can occur as a result of longer term instabilities such as those cause by vibrations and thermal drift. This can be seen if we consider a small change in the length L of a cavity and its effect on a longitudinal mode solution frequency ν

$$|d\nu| = \frac{\nu}{L}|dL| \tag{2.68}$$

where $d\nu$ is a change longitudinal mode frequency, and dL is a change in the cavity length. The additional length gained by using external cavities demonstrate an improvement in frequency stability.

2.4.3.3 Other Stability Factors

It is rare to obtain a measurement of the linewidth that is limited to the value of the modified Schawlow-Townes linewidth (Equation 2.66), especially if the linewidth measurement is made "directly" through fitting of the intensity distribution of beating two laser lines. External optical feedback can play a significant role in the measured linewidth of the laser. In addition to these sources of noise, perhaps the most significant source of phase instability, especially at lower frequencies, is due to vibrations and thermal drift. This is a limiting factor in many ECDLs that utilise moving mechanical parts such as the Littrow and Littman configurations. In these systems there are many entry points for noise to interact with the system; these include thermal expansion of the materials especially metallic materials, large vibrationally conductive parts are susceptible to acoustic vibrations causing cavity length variation, and noise from actuators. These sources of instability have motivated improved geometries [23], environmental isolation [16], [24], and new optical platforms for ECDLs, to obtain highly stable ECDLs [14].

2.4.3.4 Phase noise

The phase noise metric refers to determining the PSD of $\phi(t)$. Both the linewidth and phase noise PSD metrics are derived from the same term $\phi(t)$, however the phase noise provides a more comprehensive measurement and can be used to fully determine the fundamental linewidth of a laser. If $\alpha(t)$ from Equation 2.59 is assumed to be zero, in single frequency lasers this a reasonable assumption due to their low intensity noise, the autocorrelation function $R_E(\tau)$ of Equation 2.59 becomes [25], [26]

$$R_E(\tau) = E_0^2 e^{i2\pi f_0 \tau} e^{-2\int_0^\infty S_{\delta\phi}(f)\frac{\sin^2(\pi f \tau)}{f^2} df} \tag{2.69}$$

where $\delta\phi$ is the fluctuations in frequency that is defined as the derivative of $\phi(t)$ with t, also known as the *frequency noise*. The Fourier transform of Equation 2.69

$$R(\nu) = 2\int_{-\infty}^{\infty} R_E(\tau) e^{-2\pi\nu\tau} d\tau, \tag{2.70}$$

where ν is the optical frequency. The Wiener–Khinchin theorem states that the Fourier transform of a function's autocorrelation gives the PSD of that function. It is difficult however to integrate Equation 2.70 analytically. However if we consider a white

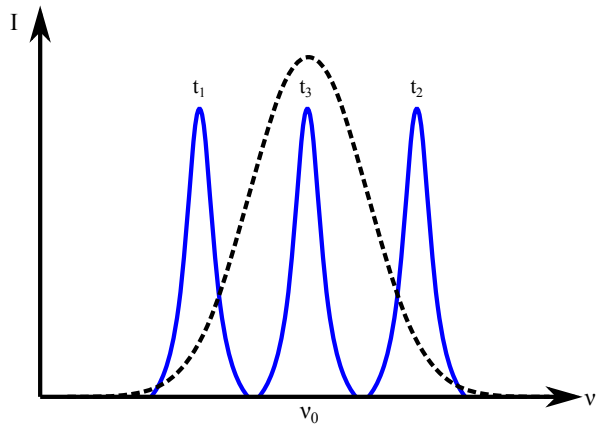

Figure 2.11: A visualisation of how the fundamental line moves and results in a wider apparent fundamental line. The blue fundamental line is depicted at different time instants t_1, t_2 and t_3, resulting in an overall measured line shape shown in black [27]

.

frequency noise spectrum $S_{\delta\phi} = \frac{\delta\nu}{\pi}$, a Lorentzian line shape is obtained with FWHM of $\delta\nu$ [26].

With the knowledge that a white noise spectrum in the frequency noise PSD, which is $\frac{\delta\nu}{\pi f^2}$ in phase noise, can be used to determine the fundamental linewidth from phase noise PSDs. Attempts to measure the fundamental linewidth directly usually provide overestimates of the linewidth. The reason for this, is that the fundamental line can be thought of as "moving" in time during the measurement, resulting in a smeared line shape, as depicted in Figure 2.11.

If the phase noise PSD can be measured, the fundamental linewidth can be determined independently of any fluctuations. A simple method to compute the linewidth from a phase noise PSD is to fit to a noise model such as [27]

$$R_\phi(f) = \frac{\delta\nu}{\pi f^2} + \frac{k_f}{\pi f^3} + \frac{k_r}{\pi f^4}, \tag{2.71}$$

where k_f is the flicker noise, and k_r is the random walk. Representing the phase fluctuations using a PSD of the phase noise imparts the most information. This representation makes it clear what frequency or phase modulation schemes could be used to achieve the greatest signal-to-noise ratio (SNR), for instance, in telecommunications. In addition it is simple to determine the Lorentz linewidth with high accuracy. This is a frequently quoted metric, as large but slow drifts that are typical in free running lasers generally do not distort the curve fitting of the phase or frequency noise PSD.

2.5 Infrared spectroscopy

Electrons confined in a molecule display a discrete set of energy levels that are permitted. These energy levels are predicted by the Schrödinger equation. Optical spectroscopy is concerned with the interaction between molecules and electromagnetic radiation. A photon incident on a molecule can be absorbed when the energy difference matches the photon energy:

$$h\nu = \mathcal{E}_n - \mathcal{E}_m, \tag{2.72}$$

where $\mathcal{E}_n$ and $\mathcal{E}_m$ are two energy levels. However not all transitions are allowed and depend on the particular pair of transitions as governed by transition rules. In the visible spectrum these optical absorption typically excite electronic transitions. Infrared spectroscopy, however, is concerned with vibrational and rotational mode excitations.

These spectral resonances are narrow and specific. This specificity makes them useful as wavelength references and provides an excellent means to optically detect gas without the uncertainty introduced from crosstalk which is a common problem in electrochemical based gas sensors. A laser with a sufficiently narrow linewidth (~MHz) and matching wavelength will be strongly absorbed by a target gas inferring its presence.

A class of techniques of particular interest in sensing and spectroscopy is known as tunable diode-laser spectroscopy (TDLS). These techniques utilise the tuneabiltiy, low RIN and narrow linewidths of diode lasers to scan and interrogate gas samples. Though the techniques usually use single frequency lasers, they are not limited to them. This type of gas sensing has the potential to sense ultra low concentrations (as low as ppb) and is usually gas specific [28].

Two standard techniques in TDLS can either be a simple relatively slower sweep of the laser across the spectral line, looking for the dip in intensity. Due to the lower frequencies of scanning, this can be limited by the higher noise (usually $1/f$ noise) typically found in lasers near DC frequencies, though it is possible to post process through averaging and careful digital filtering to reduce the background noise. To vastly improve the signal to noise ratio a frequency modulation technique can be employed. The technique applies a small sinusoidal modulation to the signal as it sweeps slowly across the absorption line, harmonics of the modulation signal can be lock-in detected [28], [29]. This has the advantage of moving signal detection away from the higher DC noise region by detecting harmonics and making it easier to modulate at higher frequencies as a triangle wave is not used that contains higher harmonic

components. An additional advantage is the use of lock-in detection that effectively limits detection to a narrow band filter rejecting most noise (Figure 2.12).

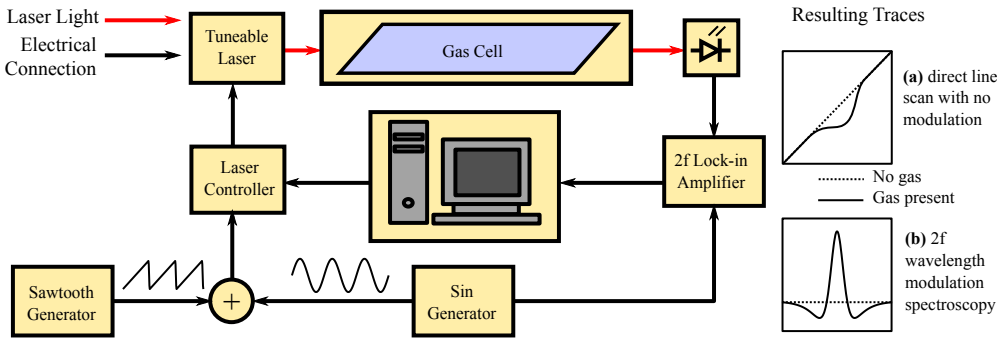

Figure 2.12: System diagram of a common TDLS setup. Both direct scanning and wavelength modulation methods are included. In direct scanning method the sine generator is simply turned off (a) Signal obtained from direct scanning, dip shows location of line. (b) Signal obtained from looking at the second harmonic of the gas line using a frequency modulated diode-laser. Figure inspired from [28]

A small frequency modulated signal is applied to the absorption line and put through a photodiode connected to a lock-in amplifier. The lock-in amplifier will be able to detect harmonics of the signal. This can be reasoned by expressing the absorption with a Taylor series expansion about the fundamental frequency ω_0

$$\alpha_{\mathrm{ab}}(\omega) = \alpha_{\mathrm{ab}}(\omega_0) + \alpha_{\mathrm{ab}}{}'(\omega_0)(\omega - \omega_0) + \alpha_{\mathrm{ab}}{}''(\omega_0)(\omega - \omega_0)^2 + \cdots \tag{2.73}$$

where α_{ab} is the coefficient of absorption. If the fundamental frequency is located at the peak of the absorption line, the second term of Eq. 2.73 will be strongest due to the parabolic shape of the peak. A frequency modulation of $A\sin(\omega_{\mathrm{fm}}t)$ at ω_0 will lead to $A^2\sin^2(\omega_{\mathrm{fm}}t)$, which using simple trigonometric identities gives a second harmonic $2\omega_{fm}$ term that can be detected on a lock-in amplifier. Since the system is being modulated at a frequency ω_{fm}, the system is distanced from the high noise $1/f$ region.

2.5.1 Broadening mechanisms

Spectral absorption lines are not perfectly sharp and have a non-zero width due to a number of broadening mechanisms. Fundamentally, gas lines are broadened due to the quantum uncertainty of atomic energy levels. In practice however this broadening mechanism is small and the most significant broadening mechanisms are collision and Doppler broadening, which arise from the dynamic motions of molecules and can be

reasoned classically. In this section a theoretical description of the these broadening mechanisms will be described.

2.5.1.1 Natural broadening

Though the fundamental nature of natural broadening is quantum, it can be modelled classically by considering the emitting electron as a damped oscillator. During an electron transition to a lower energy state a field is emitted. We consider this field to decay exponentially with time. Taking the Fourier transform of the decaying field we obtain a Lorentzian profile

$$I_{\mathrm{L}}(\omega) = I_0 \frac{\gamma_{\mathrm{n}}\omega}{(\omega_0^2 - \omega^2)^2 + (\gamma_{\mathrm{n}}/2)^2} \tag{2.74}$$

Where γ_{n} is the FWHM of the natural broadened profile. This type of broadening is known as natural or lifetime broadening. It is the most fundamental broadening mechanism. Generally this broadening mechanism is not the dominant broadening mechanism and can only be observed when other broadening mechanisms have been eliminated.

2.5.1.2 Collision broadening

Collision broadening, also known as pressure broadening or self broadening is the result of collisions between emitting molecules in a gas. When a molecule is undergoing an emission and collides with another molecule it will undergo an abrupt and random phase change to its emitted field. As the pressure or density of a gas effects how likely a molecule is to collide the FWHM, γ_{c}, of this broadening mechanism is often given in units of $\mathrm{cm}^{-1}\,\mathrm{atm}^{-1}$ (note that the wave number unit cm^{-1} is a common unit used in spectroscopy for describing spectra in the frequency domain). This type of broadening can be thought of being similar to natural broadening as it is effectively reasoned as the average lifetime an emitting molecule has to radiate before a collision event occurs disrupting the phase. As a consequence it is also described with a Lorentzian line shape. This type of broadening is generally the most dominant type at atmospheric pressures and room temperatures.

2.5.1.3 Doppler broadening

Doppler broadening arises from the Doppler frequency shifts of the molecules moving within the gas as a result of their thermal kinetic energy. As emission and absorption spectra are measured along a linear path, we consider the one-dimensional Doppler shifted frequency

$$\omega = \omega_0 \left(1 + \frac{v}{c}\right), \tag{2.75}$$

where ω_0 is the unshifted angular frequency, v is the molecular velocity. At a temperature T the kinetic energy distribution of the molecules in a gas are described by the Maxwell-Boltzmann distribution [30]

$$n_{\text{at}}(v)\, dv = N_{\text{at}} \sqrt{\frac{m}{2\pi kT}} e^{-\frac{mv^2}{2kT}}, \tag{2.76}$$

where $n_{\text{at}}(v)\, dv$ is the number of atoms within the velocity span dv, N_{at} is the total number of atoms, m is the mass of a molecule, T is the temperature and k is the Boltzmann constant. The emission strength of a transition will be proportional to the number of atoms at the shifted frequency ($I \propto n_{\text{at}}(v)(\omega)\, d\omega$). Thus combining Equations 2.75 and 2.76 leads to the emission distribution

$$I_{\text{G}}(\omega) = I_0 e^{-\frac{mc^2(\omega-\omega_0)^2}{2kT\omega_0^2}}, \tag{2.77}$$

which has FWHM of

$$\Delta\omega_{\text{G}} = \frac{2\omega_0}{c} \sqrt{2 \ln 2 \frac{kT}{m}}. \tag{2.78}$$

2.5.2 Voigt spectral profile

A simple method to determine the overall spectral profile where there are multiple significant broadening mechanisms, is to compute the convolution integral between each of the different broadening mechanisms. The convolution of the Lorentzian line shapes as a result of natural and collision broadening is also a Lorentzian, leading to a simple FWHM expression of $\Delta\omega_{\text{L}} = \gamma_{\text{n}} + \gamma_{\text{c}}$.

At lower pressures Doppler and pressure broadening effects can be comparable. At these pressures the line shape can neither be described as a Lorentzian or Gaussian but

the convolution of the two distributions. This distribution is known as a Voigt profile

$$I_{\text{Voigt}}(\omega) = \int_{-\infty}^{\infty} I_{\text{Gaussian}}(\omega') I_{\text{Lorentz}}(\omega - \omega')\, d\omega'. \tag{2.79}$$

The integral in this profile cannot be computed analytically. However using an empirical formula the FWHM can be accurately approximated by [31]

$$\Delta\omega \simeq 0.5346\Delta\omega_{\text{L}} + \sqrt{0.2166\Delta\omega_{\text{L}}^2 + \Delta\omega_{\text{G}}^2}. \tag{2.80}$$

2.6 Conclusion

The theoretical concepts featured in this chapter give an understanding of the physics that underpin fabrication and experimental results considered in this thesis.

The basics of wave guidance has been considered with an example of a simple solution to a slab waveguide. An understanding of this theory is essential as it underpins the guidance mechanisms used in this thesis. The relationships between waveguide geometry, the effect on single mode guidance and the effective index that are solved for slab waveguides, approximately illustrate the similar relationships in the channel waveguides fabricated in this thesis.

The nature of Bragg grating reflection has been considered. A simple wave vector model has been given to show the phase matching conditions and derive the Bragg condition. To understand how to model and predict the reflection and transmission spectra of a Bragg grating, a derivation of coupled mode theory has been given, derived from Maxwell's equations, with some examples of simulated grating spectra of different apodisations. This theory was used to help design and predict the reflectivity and spectral shapes of laser reflectors used in this thesis.

The physical origins of laser noise has been considered for both intensity and phase noise. The relationship between phase noise and linewidth has been discussed. The nature of the spontaneous noise contribution to phase noise has also been covered. A discussion of environmental noise sources was given to explain the noise seen in practice.

The physical nature of spectral lines was discussed. Some experimental methods that can be used to characterise them. Finally, natural, pressure and Doppler broadening processes and their aggregation are discussed to indicate the physical origin of the spectral line shapes observed in this thesis. The next chapters will present the experimental

work performed for this thesis. Chapter 3 will outline all the fabrication methods used in this research, Chapters 4 and 5 will cover the characterisation of the assembled external cavity diode lasers.

Bibliography

[1] C. Holmes, J. C. Gates, L. G. Carpenter, H. L. Rogers, R. M. Parker, P. A. Cooper, F. R. M. Adikan, C. B. Gawith, P. G. Smith, and S. Chaotan, "Direct UV-written planar Bragg grating sensors," *Meas. Sci. Technol.*, vol. 26, no. 11, p. 112 001, 2015.

[2] Y.-J. Rao, "In-fibre Bragg grating sensors," *Meas. Sci. Technol.*, vol. 8, no. 4, pp. 355–375, Apr. 1997.

[3] E. L. Wooten, K. M. Kissa, A. Yi-Yan, E. J. Murphy, D. A. Lafaw, P. F. Hallemeier, D. Maack, D. V. Attanasio, D. J. Fritz, G. J. McBrien, *et al.*, "A review of lithium niobate modulators for fiber-optic communications systems," *IEEE J. Sel. Topics. Quantum Electron.*, vol. 6, no. 1, pp. 69–82, 2000.

[4] M. Smit, "New focusing and dispersive planar component based on an optical phased array," *Electron. Lett.*, vol. 24, no. 7, pp. 385–386, 1988.

[5] A. Yariv, "Coupled-mode theory for guided-wave optics," *IEEE J. Quantum Electron.*, vol. 9, no. 9, pp. 919–933, Sep. 1973.

[6] R. Kashyap, *Fiber bragg gratings*. Academic press, 2009.

[7] A. Ghatak and K. Thyagarajan, *An introduction to fiber optics*. Cambridge university press, 1998.

[8] T. Erdogan, "Fiber grating spectra," *J. Lightw. Technol.*, vol. 15, no. 8, pp. 1277–1294, 1997.

[9] L. A. Coldren, S. W. Corzine, and M. L. Mašanović, *Diode Lasers and Photonic Integrated Circuits*, 2nd ed., K. Chang, Ed. John Wiley & Sons, 2012.

[10] G. Parker, *Introductory Semiconductor Device Physics*. CRC Press, 2004.

[11] P. Epperlain, *Semiconductor Laser Engineering, Reliability and Diagnostics: A Practical Approach to High Power and Single Mode Devices*. John Wiley & Sons, 2013.

[12] M. Yamada, "Theory of Mode Competition Noise in Semiconductor Injection Lasers," *IEEE J. Quantum Electron.*, vol. 22, no. 7, pp. 1052–1059, 1986.

[13] D. Kuksenkov, H. Temkin, and S. Swirhun, "Polarization instability and relative intensity noise in vertical-cavity surface-emitting lasers," *Appl. Phys. Lett.*, vol. 67, no. 15, pp. 2141–2143, 1995.

[14] K. Numata, M. Alalusi, L. Stolpner, G. Margaritis, J. Camp, and M. Krainak, "Characteristics of the single-longitudinal-mode planar-waveguide external cavity diode laser at 1064 nm," *Opt. Lett.*, vol. 39, no. 7, pp. 2101–2104, Apr. 2014.

[15] K. I. Kallimani and M. O'Mahony, "Relative intensity noise for laser diodes with arbitrary amounts of optical feedback," *IEEE J. Quantum Electron.*, vol. 34, no. 8, pp. 1438–1446, 1998.

[16] S. Vogt, C. Lisdat, T. Legero, U. Sterr, I. Ernsting, A. Nevsky, and S. Schiller, "Demonstration of a transportable 1 Hz-linewidth laser," *Appl. Phys. B*, vol. 104, no. 4, pp. 741–745, 2011.

[17] M. Ahmed and M. Yamada, "Influence of instantaneous mode competition on the dynamics of semiconductor lasers," *IEEE J. Quantum Electron.*, vol. 38, no. 6, pp. 682–693, Jun. 2002.

[18] Y. Yamamoto and N. Imoto, "Internal and external field fluctuations of a laser oscillator: Part I–Quantum mechanical Langevin treatment," *IEEE J. Quantum Electron.*, vol. 22, no. 10, pp. 2032–2042, 1986.

[19] A. L. Schawlow and C. H. Townes, "Infrared and optical masers," *Phys. Rev.*, vol. 112, no. 6, p. 1940, 1958.

[20] C. Henry, "Theory of the linewidth of semiconductor lasers," *IEEE J. Quantum Electron.*, vol. 18, no. 2, pp. 259–264, Feb. 1982.

[21] K. Petermann, "External optical feedback phenomena in semiconductor lasers," *IEEE J. Sel. Top. Quantum Electron.*, vol. 1, no. 2, pp. 480–489, 1995.

[22] R. Tkach and A. Chraplyvy, "Regimes of feedback effects in 1.5-μm distributed feedback lasers," *J. Lightw. Technol.*, vol. 4, no. 11, pp. 1655–1661, 1986.

[23] J.-M. Breguet, S. Henein, I. Kjelberg, M. Gumy, W. Glettig, S. Lecomte, D. Boiko, and V. Mitev, "Tunable extended-cavity diode laser based on a novel flexure-mechanism," *Int. J. Optomechatronics*, vol. 7, no. 3, pp. 181–192, 2013.

[24] M. G. Tarallo, N. Poli, M. Schioppo, D. Sutyrin, and G. Tino, "A high-stability semiconductor laser system for a ^{88}Sr-based optical lattice clock," *Appl. Phys. B*, vol. 103, no. 1, pp. 17–25, 2011.

[25] T. Udem, J. Reichert, R. Holzwarth, and T. Hänsch, "Absolute optical frequency measurement of the cesium D1 line with a mode-locked laser," *Phys. Rev. Lett.*, vol. 82, no. 18, p. 3568, 1999.

[26] G. Di Domenico, S. Schilt, and P. Thomann, "Simple approach to the relation between laser frequency noise and laser line shape.," *Appl. Opt.*, vol. 49, no. 25, pp. 4801–7, Sep. 2010.

[27] S. Camatel and V. Ferrero, "Narrow linewidth CW laser phase noise characterization methods for coherent transmission system applications," *J. Lightwave Technol.*, vol. 26, no. 17, pp. 3048–3055, 2008.

[28] J. Hodgkinson and R. P. Tatam, "Optical gas sensing: a review," *Meas. Sci. Technol.*, vol. 24, no. 1, p. 012 004, Jan. 2013.

[29] W. Demtröder, *Laser Spectroscopy: Vol. 2: Experimental Techniques*, 4th ed. Springer, 2008.

[30] W. Demtröder, *Laser Spectroscopy: Vol. 1: Basic Concepts and Instrumentation*. Springer, 2013.

[31] J. J. Olivero and R. Longbothum, "Empirical fits to the Voigt line width: a brief review," *J. Quant. Spectrosc. Radiat. Transf.*, vol. 17, no. 2, pp. 233–236, 1977.

- Chapter 3 -

Fabrication

3.1 Introduction

This chapter details the processes used to fabricate the optical platforms used in this research; precision optical dicing of the devices, fabrication of UV-written Bragg gratings and waveguides, the fabrication of micro-heating elements used for Bragg wavelength tuning, assembly of the external Bragg reflector into an external cavity diode laser (ECDL) system, and finally the miniaturisation of these systems into a small, compact and stable packages.

It is worth noting that in this section and throughout the rest of thesis, reference is often made to the *external cavity*. This often refers to the chip hosting the reflector that forms a cavity in conjunction with the gain chip, neither of which are cavities in their own rights, though the context will make this clear.

First the flame-hydrolysis deposition process will be described. This is the process that is used to fabricate the glass layers used in the planar platform and has been recently developed to produce the planar-fibre composite platform known as integrated optical fibre (IOF). These platforms form the basis for the laser external cavities demonstrated in this thesis. The chemical composition, process steps, and optimisation techniques will be described for both of these platforms.

The dicing and shaping of the wafers into the appropriate geometry for the chips will be covered. In addition the technique used to dice the facets of the chips to achieve an optical quality facet will be detailed. Characterisation of the chips' facets using white light interferometry will be discussed. The section also investigates process optimisations needed for the IOF platform.

The follow section describes the UV-writing process that is used to inscribe waveguides and Bragg gratings simultaneously into the planar and IOF platforms will be discussed. The process will be described in detail, including the characterisation of the platform hosting the inscribed gratings.

The design and fabrication of the micro-heating system used to tune the Bragg wavelength of the external cavity will be covered. This system consists of small heating elements deposited in close proximity to the core containing the grating structure. This section will, in addition, describe the modelled thermal characteristics of the system.

Finally the assembly of the various prototype systems will be discussed. Details of the assembly procedure will be covered on packaging the device into a compact housing and the reasoning for doing so.

3.2 Flame hydrolysis deposition

The flame-hydrolysis deposition (FHD) process is similar to and based on the successful approach to the well-established fibre preform fabrication processes. Fibre preforms are fabricated using two common techniques known as modified chemical vapour deposition (MCVD) and outside vapour deposition (OVD). These processes are favoured as the precursors are liquid and can be easily purified through fractional distillation (<1 ppm) and allowing for high purity preforms to be fabricated [1]. These processes use oxidisation or hydrolysis of the precursors forming oxide aerosols that are deposited onto the preform as a type of soot. The soot is then sintered into a uniform glass layer at high temperature. Silica for example is formed by the oxidation or hydrolysis of $SiCl_4$ through the equations

$$SiCl_4 + O_2 \longrightarrow SiO_2 + 2\,Cl_2 \tag{3.1}$$

$$SiCl_4 + 2\,H_2O \longrightarrow SiO_2 + 4\,HCl\cdot \tag{3.2}$$

The planar waveguide analogue of these processes is known as FHD and it is most similar to the OVD process that uses a hydrogen-oxygen flame to form the oxide aerosols that are deposited onto the substrate. FHD is the process used in this research for the deposition of glass layers to form the vertical structures of the planar waveguides. Usually the glass layers are deposited on silicon wafers with a thermally grown silica

layer that acts as the underclading layer of a waveguide. The same FHD process is used to attach fibres for the IOF platform.

The deposition of glass layers onto prefabricated thermally grown silica-on-silicon wafers was carried out by the author including the discussed optimisation of layer design discussed in Section 3.2.3.1. In addition, the author helped pioneer and optimise the process for integrated optical fibre fabrication process.

3.2.1 System overview

In this process the system is made up of three main components: the gas delivery system, the FHD chamber and the furnace.

The gas deliver system contains the various precursors used in the process. These precursors are kept as liquids in glass bubblers where nitrogen gas is fed or "bubbled" through a glass vessel containing the liquid precursor that carries some as a vapour and is then transported to the hydrogen oxygen flame at the torch. The nitrogen gas for each bubbler uses a mass flow controller (MFC) that allows the careful control of the feed rate of each precursor. According to the desired recipe the precursors used are $SiCl_4$, PCl_3, $GeCl_4$, that are liquid and can be transported as vapour using bubblers and BCl_3 which is gaseous and readily oxidises and hydrolyses to GeO_2.

The FHD chamber contains the turntable and torch as depicted in Figure 3.1. The precursors are deposited as oxide soot onto the turntable and wafers, whilst venting the other gas as waste. The turntable is heated to 180 °C to prevent water and HCl from condensing and ensure they are vented. Moisture build up on the turntable can cause the soot to crystallise and introduce an unwanted infrared (IR) absorbing OH groups into the glass lattice when later sintered. The turntable itself is made of silicon carbide and can hold six 15 cm wafers. Whilst in operation the turntable rotates and the flame is translated radially between the centre of the turntable and the table edge. The radial and rotational speed is controlled to ensure uniform distribution of soot onto the table. The number of passes which is the number of times the flame is translated across the table in a recipe, can be used to determine the thickness of the glass melt after sintering.

After the process is finished, the wafers are then transferred to a furnace where the soot is sintered into an uniform glass lattice. The temperature profile of the furnace has important consequences on the properties of the sintered glass layer as will be discussed in the next section.

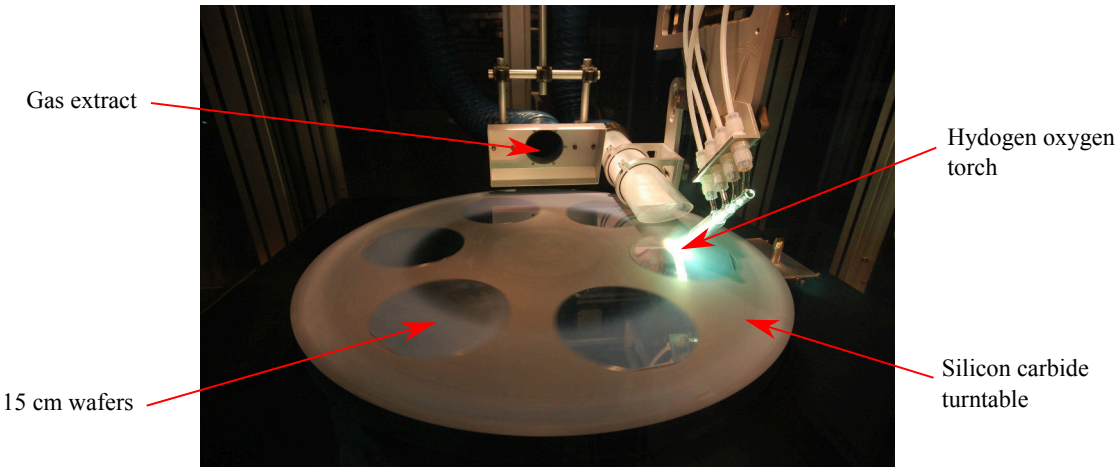

Figure 3.1: Labelled photograph of the FHD chamber. The photo depicts the turntable holding 6 wafers with the torch depositing precursor oxides onto the surface. The flame is burns green as a result of the strong green emission lines due to the presence of boron in one of the precursors.

3.2.2 Control of wafer properties

The FHD system allows the control of numerous properties of the layers. Layer thickness, layer refractive index, melt temperature and photosensitivity can all be controlled by modifying various aspects of recipes. Where photosensitivity refers to capability of the material to change its refractive index when exposed to UV light and is covered in more detail in Section 3.4.1. Though it is known how changing various parameters in a process affect the properties of the final wafer it is difficult to predict to what extent and so recipes must be developed empirically from previous FHD depositions.

Controlling the concentration of various dopants has the greatest effects on the overall properties of the wafer varying every property of the layer. Germanium can be used to make the layer highly photosensitive by introducing bond defects into the glass lattice. These defects introduce an absorbing band at 240 nm, that when exposed to UV light at this wavelength, causes a permanent increase to the refractive index [2]. The effects on the final glass properties of each layer are indicated in Table 3.1. By careful consideration and iterative development, recipes can control layer refractive index, glass transition temperature (T_g) and photosensitive independently. It is possible, for example, to fabricate a three layer wafer where the core layer is highly photosensitive despite no refractive index difference between layers. This structure is known as a zero Δn waveguide and is useful for mode matching to silica fibres.

The furnace must reach a sufficient temperature so that the soot can phase change to a melt. High temperature and long sintering times allow the melt to reflow and form a

Dopant	Refractive Index	Glass Transition Temperature	Photographsensitivity
Boron	-	- -	+*
Germanium	+	-	+ +
Phosphorus	+	-	-

*Only in the presence of Germanium

Table 3.1: Table indicating the various effects as a result of adding the dopant to the silica glass. As the effects are nonlinear and highly dependent on other recipe parameters only the general effects are indicated. - indicates a lowered value, - - significantly lowered, + an increased value, and + + significantly increased value.

uniform layer. Holding the melt at high temperatures for too long however can lead to dopants, particularly phosphorus, diffusing into lower layers resulting in indistinct layers. To help reduce this diffusion the recipe for a layer is designed so that subsequent layers melt at lower temperatures further reducing the migration of precursors into other layers. Extended sintering can also lead to unwanted crystallization of the glass.

This process can be repeated for multiple layers, for example creating a core and upper cladding layer. Normally an underclad is not deposited as the thermally grown silica layer is used instead known a thermally oxidised (THOX) wafer. This silica layer is extremely pure and so only melts at high temperatures (>1600 °C) preventing dopants from diffusing into the layer forming helping to form distinct layers.

The layer thickness are checked and measured using a prism coupling system from the Metricon Corporation. This system couples 633 nm laser light via a prism into the top layers of the FHD produced wafers. As various angles are tried different levels of coupling are achieved depending on the refractive index of the layer and the thickness of the layer.

3.2.3 Planar phosphogermanate optical platform

For the devices based on the planar platform, the glasses used in the fabrication of the planar wafer that will later be processed to form the external cavity chip, use a phosphogermanate glass for the core and a doped silicate as the overclad. As stated earlier germanium typically increases photosensitivity however there is a limit to the quantity of germanium that can be added to silicate glasses. Alternatively phosphogermanate that is free of silicon, allows for a high concentration of germanium and also has a low T_g of ~550 °C [3]. Photosensitivity is critical for the core layer as it corresponds to greater refractive index changes when exposed to UV light during UV-writing. The

UV-writing process will be discussed in Section 3.4. The P_2O_5 present in the glass significantly decreases the T_g and viscosity of the glass during sintering allowing for extremely uniform layers in terms of layer smoothness and flatness. The uniformity is an important factor when considering losses as a significant source of losses in planar waveguides comes from scattering of light due to waveguide variation. The uniformity is also essential for the repeatability of UV-writing of waveguide and Bragg grating structures.

The THOX silicon wafers are purchased commercially as growing these is a costly process that takes over a week for layers thicker than 10 µm using a high temperature furnace in an atmosphere of H_2O [4]. The substrate wafers are ~1 mm thick with a ~15 µm thermally grown silica layer that acts as the underclad of the waveguide. The layer must be sufficiently thick to prevent the effervescent field of the propagating mode from interacting with the high index and silicon introducing a high propagation loss.

Once the phosphogermanate layer is sintered the overclad must be deposited. This is a silicate based recipe that uses phosphorous and boron dopants to reduce the sintering temperature and lower the refractive index below the phosphogermanate layer. Although the overclad has a significantly higher T_g and must be sintered at a higher temperature than the phosphogermanate core T_g, there is little diffusion between the layers.

3.2.3.1 FHD design optimisation

The waveguides produced for the planar devices from the combined FHD and UV-writing processes can be modelled using a package called FIMMWAVE[1]. The film mode matching (FMM) method was used to solve the waveguides. This solver is a semi-analytic method that is most suitable for structures that can be accurately described as a stack of layers such as the UV-written, FHD fabricated planar waveguides. This method is often more efficient than others that rely upon discretising the entire structure, such as the finite element and finite difference methods. A theoretical description is beyond the scope of this thesis, and the author recommends [5] for further reading.

Semiconductor based waveguides in lasers usually have a comparably small mode-field diameter (MFD) due to high indices typical of semiconductors when compared with dielectric glasses. The gain chips used in this research are InP based devices available from Thorlabs. The chip will need to butt couple into the external cavity chip so that

[1]Product URL accurate as of September 2016: www.photond.com/products/fimmwave

even with perfect optical alignment and surface roughnesses, the difference in mode fields between both chips ensures there will be significant losses. The FHD process allows for the control of the core layer thickness in the phosphogermanate based external cavities, and therefore can be optimised to provide maximal coupling to the gain chip. To determine the optimal structure of the final waveguide structure once the FHD and UV-writing processes are done, the complete expected waveguide structure was modelled for various values of refractive index and layer thickness that could be deposited using FHD.

The mode field of the gain chip was approximated using a simple elliptical Gaussian model, rather than empirically determined or using a numerically solved description due to a lack of knowledge of the exact structure. Using the angular divergence values of the output beam from the gain chip specifications, an estimate of the near field elliptical Gaussian field could be determined. By computing overlap integrals using the elliptical Gaussian model for the gain chip with the solved mode field using the FMM method, for all reasonable parameters that could be fabricated using FHD, an optimal design could be determined (Figure 3.2).

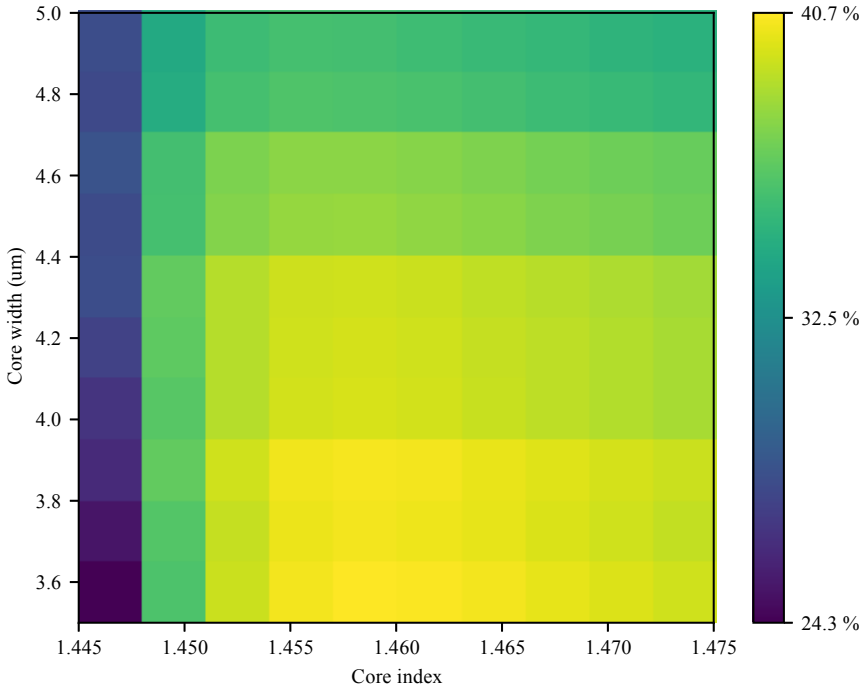

Figure 3.2: Colour map indicating coupling efficiencies for various core layer thicknesses and core refractive indices where the cladding index is 1.445. Only thicknesses and refractive indices that could be reasonably deposited using FHD and that maintained single mode behaviour were considered.

From Figure 3.2 it is clear that the FHD process is limited as the highest suggested mode coupling is 40 %. Where there is no distinction of refractive index between layers (i.e. where the core index is 1.445) leads to a much lower coupling efficiencies. As the core refractive index is increased, the coupling efficiency also rapidly increases and settles with little change after an index of 1.452. Decreasing core thicknesses generally improves coupling efficiency due to the decreasing size of the MFD. The plot shows an optimum at a core refractive index of 1.458 and a core thickness of 3.5 µm however in reality there will be diffusion up between layers during sintering effectively enlarging the intended MFD. With this in mind, rather than trying to achieve the precise optimal values produced in the plot, the most effective approach would be to aim for a structure with a small core and the highest core refractive index achievable on the FHD system. Though a coupling efficiency of 40 % is suggested it is unlikely the value will actually be this high due to the aforementioned diffusion, but also alignment errors and imperfect surface roughness between the facets.

3.2.4 Planar-fibre composite optical platform

The attached fibre to wafer composite coined as integrated optical fibre (IOF) uses the FHD process to attach a fibre using a glass melt. This is a recently developed platform that takes advantage of the highly mature fibre fabrication whilst incorporating it into a planar layer utilising planar advantages such as its rigidity, mechanical strength and thermal stability [6].

The FHD process steps for IOF are similar to conventional planar waveguide fabrication. The IOF substrate is a thermally-oxidised silicon wafer that has a ~6 µm thick silica layer. This layer is necessary to prevent certain precursors that are deposited during the FHD process from reacting with the silicon substrate leading to a brittle and deformed surface that does not successfully sinter into a glass layer. A silica based cladding recipe is used for the melt as this has less photosensitivity, permitting more UV light to penetrate into the core of the fibre. The recipe is also designed to sinter into a glass at lower temperatures. If the fibre is taken to too high a temperature the fibre becomes brittle and unsuitable, this is likely to be due to devitrification of the glass [7], [8]. The FHD deposition appears to protect the fibre somewhat from the effects of devitrification, this could be a result of the precursors migrating into the fibre lattice changing the conditions that it devitrifies. Another possibility is the presence of the soot prevents nucleation on the surface. The fibre used is a highly photosensitive optical fibre sold by Thorlabs called GF4A. This fibre, unlike the planar waveguides, does not need to be hydrogen loaded to increase its photosensitivity since its intrinsic photosensitivity

is sufficient for UV-writing. Hydrogen loading will be discussed in more detail in Section 3.4.1.

The recipe for fabricating IOF wafers is as follows:

1. The fibres are cut into lengths slightly shorter than the wafer so the fibres do not protrude over. If too long they can be knocked off more easily or simply do not fit in the furnace.

2. The fibres are mechanically stripped of their protective polymer coating using fibre strippers. Soaking in acetone to ease stripping is not preferable as this results in a residue that appears to reduce fibre adhesion to the wafer whilst sintering and induces nucleation points causing devitrification [8].

3. Fibres are cleaned with lens tissue soaked in propanol or methanol as neither of these leave polymer residues. Whilst the fibre is being held, minimal contact must be made as this transfers impurities to the fibre that leads to devitrification.

4. Fibres are carefully held with tweezers by the end over the wafer and dropped onto the wafers minimising organic contamination from the tweezers. Dropping the fibres allows them to relax and remain as straight as possible. The fibres appear to electrostatically attract to the wafer and so adjusting the fibres to straighten them succeeds only to kink the fibres making UV-writing process difficult and can likely to introduce contaminants onto the fibre that contribute to devitrification.

5. The remainder of the FHD process is performed as usual however only using several FHD passes of the flame as a thick layer of glass is unnecessary followed by sintering of the soot in the furnace using the usual recipe for the blend of precursor. In the case of phosphogermanate only 3 layers are used using the a standard core furnace recipe that goes up to 1200 °C.

Once taken out of the furnace the fibres should be adhered to the wafers. As they are bonded with glass they are rigid and maintain a high level of mechanical strength that makes them suitable for physical machining without damage. GF4A Photosensitive fibres are used in this research and the photosensitivity is preserved after processing. Photosensitivity and UV-writing will be discussed later in Chapter 3.4

3.3 Precision dicing of optical platforms

Once the FHD process is completed the wafer will need to be cut into a suitable geometry. The wafers are cut into shape using a dicing process, a standard process in the semiconductor industry. The wafer dicing machine used is a Loadpoint MicroAce 3 using nickel-bonded diamond-grit blades sourced from DISCO. The machine is versatile and as well as dicing wafers into rectangular chips that are suitable for further processing, the dicing procedure and parameters can be optimised to achieve a dicing regime known as ductile dicing that is characterised by excellent surface roughness of the diced material walls, avoiding the need for a polishing process step [9].

In this section the geometrical requirements of the external cavity chips will be discussed and how dicing is used to achieve this. The ductile dicing process will then be discussed and how that is used to obtained excellent surface roughness on the facets of the external cavities without the need for polishing.

All physical machining and the characterisation of surface roughnesses discussed in this section were all undertaken by the author. The ductile dicing process for optical waveguides was developed by Lewis Carpenter [9].

3.3.1 Geometrical shaping

The dicing saw can be accurate to around 10 µm and is ideal for machining the desired geometrical shape of the various devices used in this research. All the geometrical shaping of the devices was cut using a commercial nickel bonded diamond blade. The diamond grit size used for the geometrical shaping is <6.4 µm. This allowed for quick machining of the desired shape. In this research two types of external cavity chips were fabricated, the first device used UV-written waveguides and Bragg gratings in a planar glass-on-silicon structure, the second type used UV-written gratings in the photosensitive attached fibre of the IOF platform.

After FHD processing the wafer is diced up into a number of rectangular chips. In the case of planar waveguides almost the entire wafer is divided up into rectangular chips of various sizes, a typical chip dimensions would be 20×10 mm, though many other sizes are used only limited by the size of the wafer. After this stage the appropriate diced chips go through further processing, usually UV-writing, though depending on the intended device processing can include photolithography, deposition, or etching.

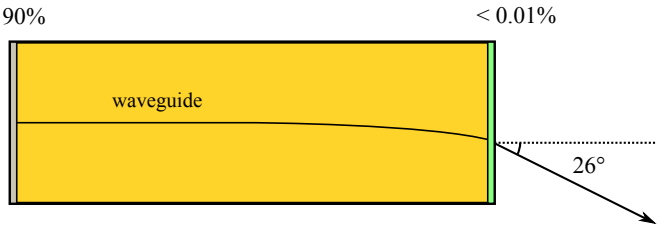

Figure 3.3: Diagram showing approximate geometry of the internal waveguide of the 1650 nm gain chip die. One edge is coated to have high reflectivity, the other emission end is antireflection coated. The radiation of the primary emission side also exits at an angle to prevent back-reflections into the waveguide.

In the final laser device the silicon-on-silica external cavity chip will be butt-coupled to the gain chip. As a result the final reflector device needs to accommodate a number of geometrical constraints. The gain chip is a $1.5 \times 1.5 \times 0.64$ mm chip that is mounted on a metallic heat-sink. The gain chip was designed to only reflect at one interface, to achieve this an anti-reflection coating is added to one facet and the waveguide exits at an angle to prevent reflection from coupling back into the waveguide as seen in Figure 3.3. The angled facet to the waveguide has the advantage that when the gain chip is operated as a laser it prevents an unwanted internal cavity from forming as the only desired cavity should be formed by the 90% end facet reflector and the Bragg-reflector. To properly couple between the gain and grating chips, the grating chip must be angle cut according to Snell's law to maximise angular coupling. The exit angle of the gain chip is specified and taking into consideration the index of the external cavity the angle computes to 17.7° for the 1651 nm planar laser and the 13.3° for the lasers at 1533 nm and 1560 nm.

To collect radiation outcoupled from the Bragg reflector efficiently and independently of drift, a commercial V-groove assembly angle polished to 8°, is adhered to the external cavity device using optically transparent UV curing adhesive. The 8° angle is essential to prevent reflections coupling back into the laser. This required an additional angled interface to be diced, given the refractive indices are well matched the angle is also 8°. This dice was not ductile as the adhesive refractive index is well matched, reducing the refractive index contrast of any roughness on the facet which helps to prevent scattering losses on at the facet.

As stated before the gain chip does not emit orthogonally from the facet as a consequence of minimising the amount of light reflected from the facet into the gain chip. The gain chip comes premounted to a metal heatsink plinth-like structure and is mounted with a tilt such that emission from the gain chip is orthogonal to the heatsink plinth as can be seen in Figure 3.6. As the gain chip itself is not square against the edge of the plinth

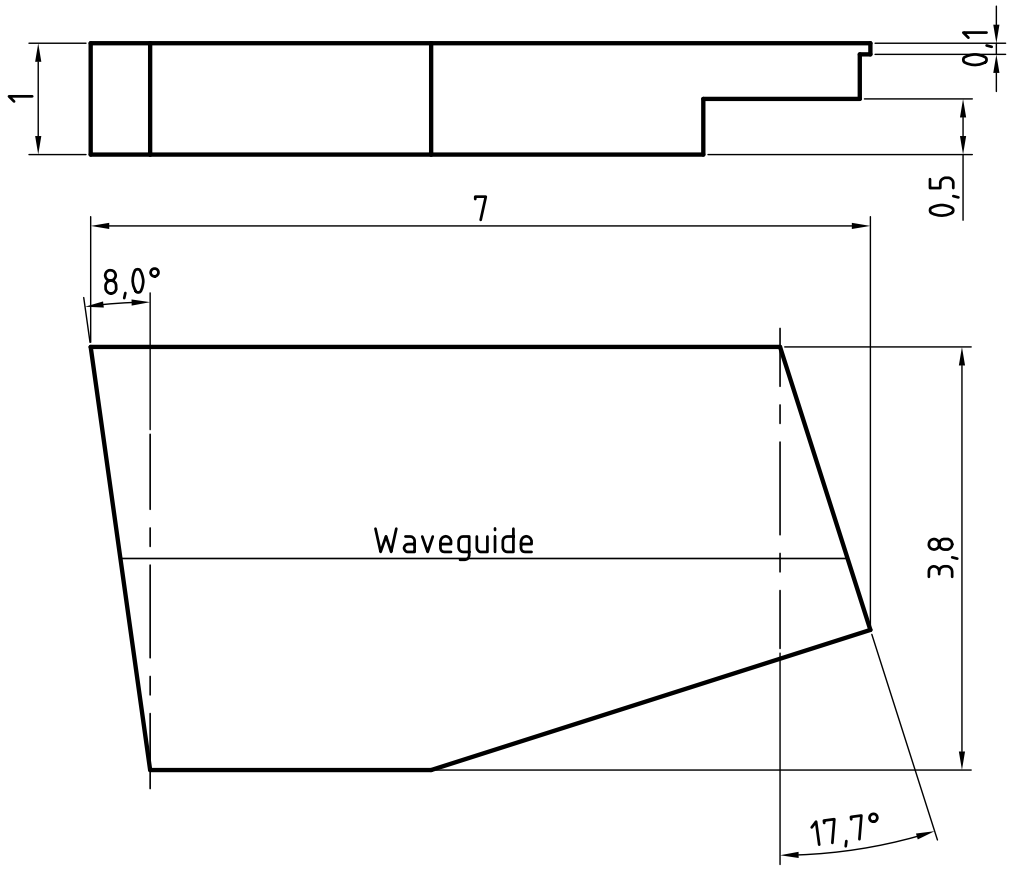

Figure 3.4: CAD drawing of the 1651 nm planar-waveguide external cavity chips. The front facet is angled at 17.7° in order to correctly satisfy Snell's law with the 1650 nm gain chip. The stepped strucuture helps accommodate the gain-chip heat-sink. This device uses a ~150 µm deep, ductile dice cut to achieve a optical quality facet. All measurement are in units of mm unless otherwise specified.

there is a step that protrudes from underneath the gain chip. The geometrical shape of the external cavity must clear the heat sink when it is butt-coupled to the gain chip. The gain chip is 780 µm thick and so the tip of the external cavity device must be thinner than this if it is to clear the heatsink, so a 1 mm × 0.5 mm step is diced out as can be seen in Figure 6.1. The width of the tip of the gain chip needed to be narrowed so as to clear the wall of the heat sink that the gain chip is mounted against. The final product after dicing can be seen in Figure 3.5 as well as the gain-chip it is butt coupled to.

On further iterations of the design of the external cavity chips, the corners of the side that would butt-couple to the gain chip were bevelled. This gives greater clearance to compensate for any angular error after machining during the alignment procedure. The bevels can been seen in the CAD drawing of the IOF chip (Figure 3.7).

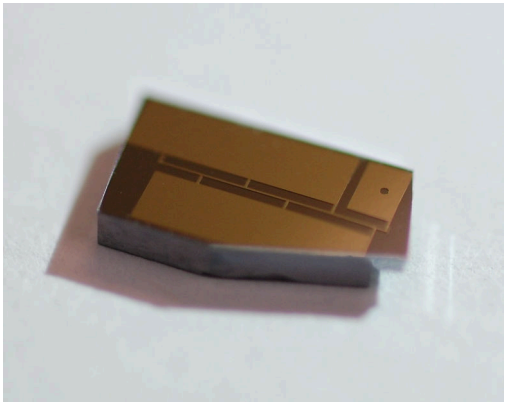

(a) The final product of the diced chip with thermal heaters is shown, the angles and step in the structure can be seen, these are needed to clear the gain chip heat sink

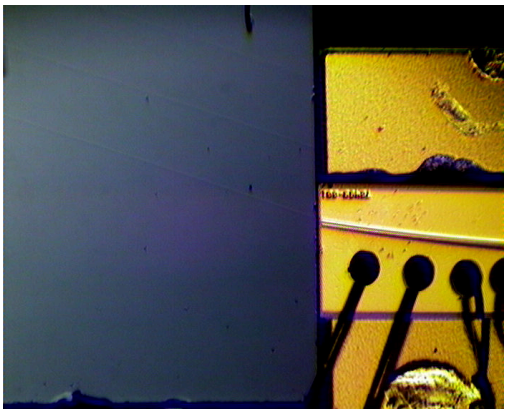

(b) A photograph of the grating-chip butt coupled to the gain chip. The waveguide of the external cavity chip on the left are aligned to the waveguide on the gain chip.

Figure 3.5: Photographs of planar external cavity.

3.3.2 Facet preparation

3.3.2.1 Surface roughness

The quality of a surface plays a fundamental role in the transmission and reflection of optical beams interacting with the surface. Small scale irregularities (<20 nm) in the surface present the optical beam with an imperfect surface causing uncontrolled scattering of the optical beam, effectively creating an insertion loss. These irregularities are referred to as surface roughness. This has important consequences for the transmission of light between interfaces of two materials with significantly differing refractive indexes. For example transmitting light between an air and silica interface, where there is a substantial difference of refractive index, surface roughness could contribute significant scattering losses at that interface. This has a direct consequence on the efficiency of coupling light into and out of a waveguide facet.

It is useful to have a metric that can give an indication to the magnitude of facet roughness, such as the average size of the features that deviate from the surface. Consider a straight line profile through a rough surface that is sampled at a regular interval giving us the "signal" $z_{i,j}$ where the indices i and j indicate sample number of the surface in the orthogonal axes. This function can be considered a signal, permitting the use of a number of statistical tools that we can use to derive a metric for the surface roughness.

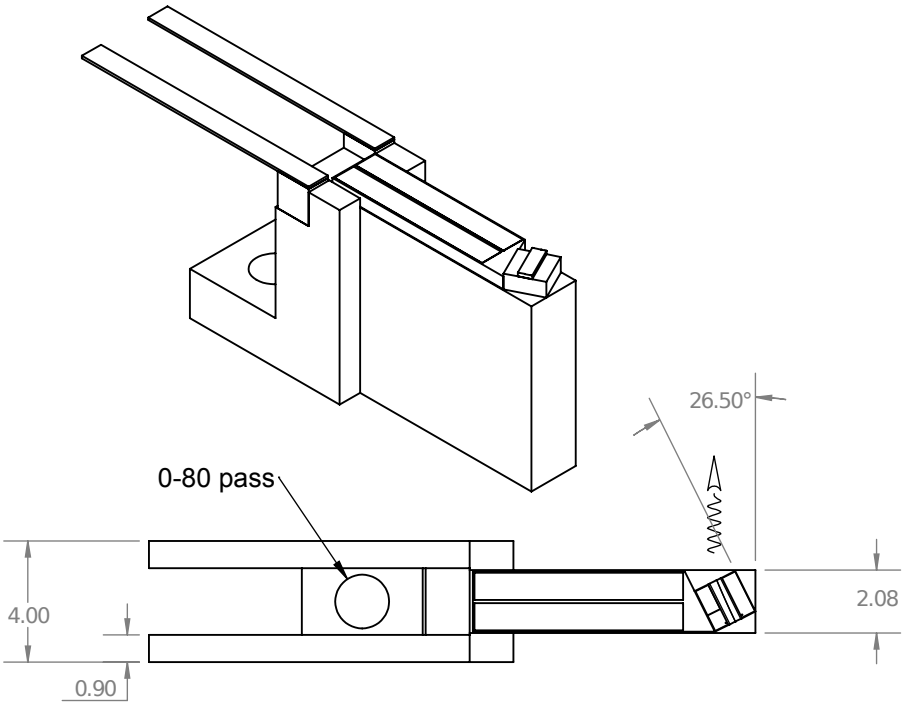

Figure 3.6: CAD diagram of the heatsink structure for the gain chip that operates at 1650 nm. The emission from the gain chip is indicated by the curvy line, which is indicates the low non-reflective facet that will be butt-coupled to external cavity device. Due to the tilt of the gain chip on the heatsink there is a small step that must be accommodated in order to clear the heatsink when aligning the external cavity device to the gain chip. Adapted from [10].

A common metric for measuring surface roughness profiles is the S_q parameter that is defined as

$$S_q \equiv \sqrt{\frac{1}{N+M}\sum_{i}^{N}\sum_{j}^{M} z_{i,j}^2}, \tag{3.3}$$

where N and M are the number of points in the x and y axes, z_i are the sampled vertical points. In this research we use the S_q parameter which simply computes the values over a profiled surface. According to theory to minimise the amount of light that is scattered diffusely the S_q value must be a value much smaller than the wavelength of light considered [11].

This metric is quite limited as it only considers one statistical moment and does not consider the spatial frequency components of the surface that have an affect on the interaction of light onto the surface. Despite the limitations, the metric provides a simple method of comparing the relative roughnesses of various prepared optical surfaces.

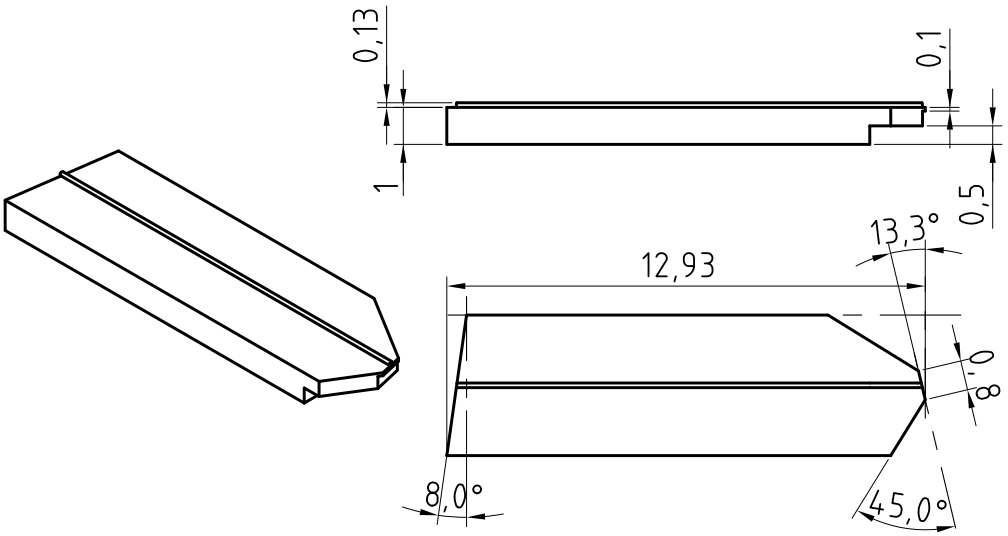

Figure 3.7: CAD drawing of both the 1533 nm and 1560 nm IOF external cavity chips. The front facet is angled at 13.3° in order to correctly satisfy Snell's law with the 1550 nm gain chip. A design improvement was introduced with this chip where the edges of the facet has bevelled corners to provide greater clearance during alignment. The stepped strucuture helps accommodate the gain-chip heat-sink. This device uses a ~150 µm deep, ductile dice cut to achieve a optical quality facet. All measurement are in units of mm unless otherwise specified.

3.3.2.2 Ductile dicing for optical quality facets

dicing roughness facets are usually achieved using mechanical polishing techniques and often includes a chemical-mechanical polishing finish. Though these techniques achieve excellent surface roughnesses, as low as 0.2 nm, these techniques are slow and require a great deal of preparation and numerous process steps, by decrementing the size of the grit size until the desired roughness is achieved. An alternative to polishing is to dice the material in the ductile regime providing comparable surface roughness in far fewer process steps.

Material removal during dicing can be classed into two machining regimes known as the ductile and brittle machining regimes. Brittle machining removes material by propagating subsurface cracks that intersect, dislodging material and leading to a high roughness surface with subsurface damage. In the ductile regime the material undergoes plastic flow, this regime is characterised by low subsurface damage and low surface roughness. Ductile regime requires precise machining parameters to achieve, otherwise brittle machining is the most likely regime [12].

The dicing parameters needed to achieve ductile dicing have largely been determined in previous research [9], [12]. The previous research was performed on silica layers on

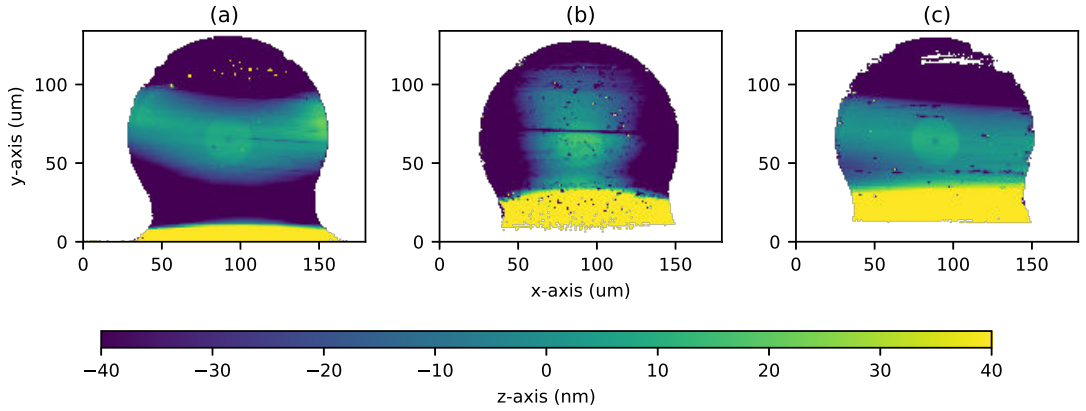

Figure 3.8: The diagram shows a set of three dices to determine the optimal DoC to use. (a) is diced 100 µm past the fibre into the silicon layer, (b) is 50 µm past, and (c) does not dice below the fibre at all. The dices were performed with a spindle speed of 25 krpm, using a diamond blade with a translation speed of 1 mm s^{-1}. The profiles were taken using a ZeScope from ZeMetrics, a white light interferometer. The z-scale has been limited to ±40 nm centred on the core.

silicon, the same as the planar waveguide external cavity device being used, however some optimisation of the depth of cut (DoC) was needed for ductile dicing of IOF, as it is not clear how the changing the DoC would affect maintaining a ductile dicing regime. Dicing too deep can prevent the ductile dicing regime, whereas dicing only as deep as the fibre height from the surface may not provide enough side walls to stabilise the blade during cutting. Once the optimal parameters for the dicing recipe have been chosen, the results are highly consistent.

The ductile dicing test consisted of dicing three cuts, on the same IOF, at three different points along the chip. The three cuts were made using a nickel-bonded diamond-grit blade. Each cut was progressively deeper by ~50 µm. The diamond-grit particle size was <5.6 µm, which is finer than the blade grit that is used when dicing for geometrical shaping. Before each dice, the blade was dressed on a commercial dressing board from sourced from DISCO. The dressing procedure consists of dicing a hard sacrificial material such as silicon carbide. The dressing is a more aggressive procedure than used in standard cuts, by intentionally wearing the blade, making the blade concentric thereby eliminating any errors associated with mounting and manufacturing. The dressing process also wears away the bonding material, revealing fresh diamonds for cutting [13].

The three different cuts gave quite different surface finishes as seen in Figure 3.8. Usually when cutting glass planar waveguides there are side walls at all times that help to stabilise the blade. The ZeMetrics white light interferometer was used to determine

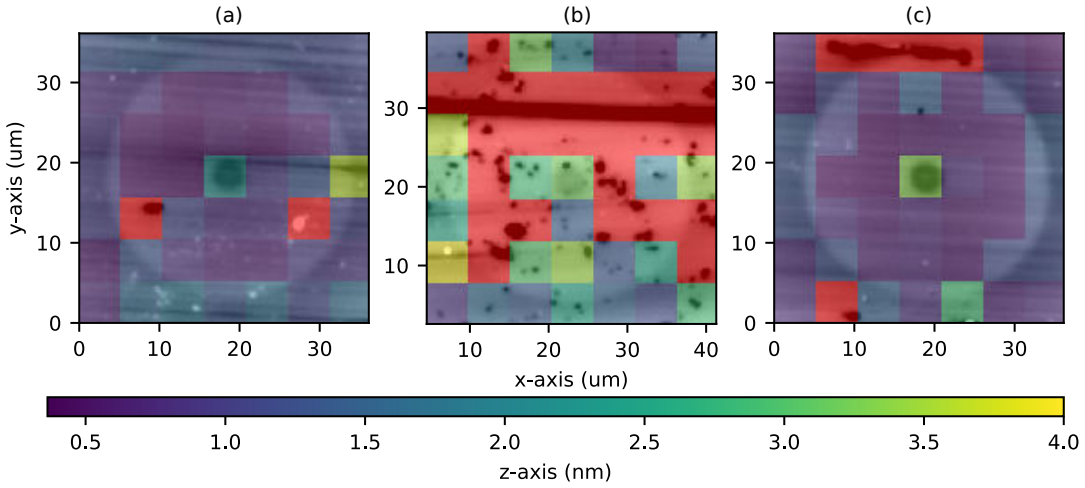

Figure 3.9: The diagram shows the same set of three dices as in Figure 3.8 in respective order to determine the optimal DoC to use. These profiles are zoomed onto the core with a colour coded grid overlay showing RMS roughness. Each grid square has length 5.16 µm and is linearly levelled. The average S_q value of the squares around the core for (a) is 0.78 nm, (b) is 12.8 nm, and (c) is 0.84 nm. The are these values are calculated over represent approximately the area covering the majority of the single-mode profile.

surface roughness profiles. Figure 3.9 shows the zoomed images around the core with a colour coded grid overlaid. For each grid square the surface has a linear deviation removed and then the S_q value computed using Equation 3.3. From the figure, dicing ~100 µm into the substrate, leads to optimal dicing conditions. The shallowest cut operates in the ductile regime as indicated by the S_q value of 0.84 nm, though there is damage around the edge of the fibre; this could be caused by instability from not having side walls present during dicing. Dicing 50 µm into the substrate leads to the most damage to the facet, failing to maintain a reliable ductile regime indicated by the pitting, this could also be related to a lack of stability of the dicing blade due to short side walls.

The best diced surface roughness achieved was compared with the roughnesses of a cleaved fibre using a Fujikura fibre-cleaver, and a commercially available polished PM V-groove pigtail from OzOptics Figure 3.10. Both the cleaved fibre and commercially polished V-groove have superior surface roughness that are <1 nm. Cleaving utilises the propagation of a fracture, producing extremely smooth surfaces whereas the polishing process of the commercial V-groove is a highly optimised process. It is important to note the advantage of replacing the time intensive, and laborious polishing process step with a relatively fast ductile dicing that can be incorporated with the other dicing processing.

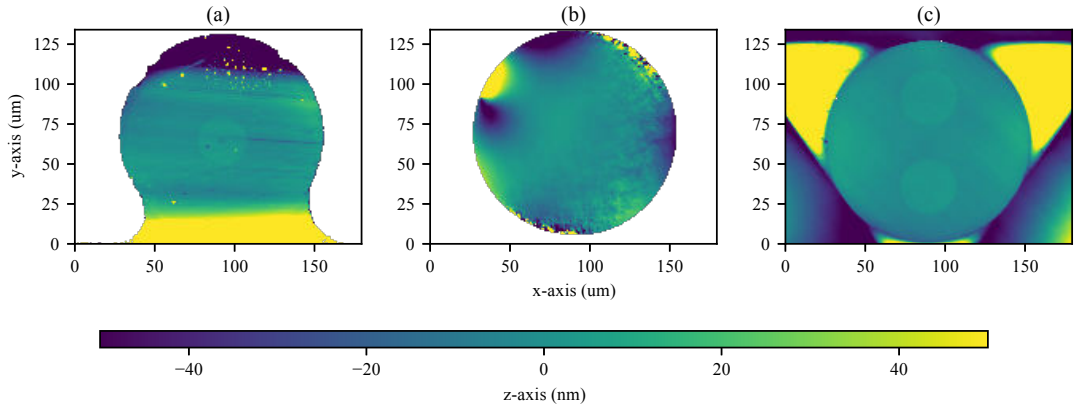

Figure 3.10: Plots showing the surface profiles of various facets: (a) diced IOF with S_q =2.5 nm (b) cleaved SMF-28 fibre with S_q =0.61 nm (c) polished PM V-groove pigtail with S_q =0.48 nm. The S_q values are computed over a circle centred on the core, 20 µm in diameter, which is approximately twice the MFD at 1550 nm. In each measurement the region that is used in the S_q computation has been levelled using a cubic surface.

3.4 UV-writing

UV-writing is the process that exploits the photosensitivity present in some materials resulting in changes of refractive index. This process can be used to rapidly create waveguides and Bragg gratings in glass-on-silicon wafers or pre-existing waveguides such as fibres.

In this section the nature of material photosensitivity in glasses is outlined, the direct UV-writing process used in this thesis explained and the how the process is used to produce waveguides and Bragg gratings in glass-on-silicon chips and the fabrication of gratings in the IOF platform.

All UV-writing carried out in this thesis and explained in this section was done by the author. The original UV-writing processes were developed by the author's research group in prior work [14], [15], however based on Dr Chris Holmes' work [6], the author helped develop and optimise the process to reliably produce UV-written gratings in the IOF platform.

3.4.1 Photosensitivity

Some glass materials when exposed to deep UV-Wavelengths (244 nm), can undergo changes in refractive index as a result of changes to the lattice, typically increasing the refractive index. This reaction to UV light is known as photosensitivity. Photosensitivity can be introduced by adding germanium dopant into the silica lattice structure, introducing germanium dioxide defect sites.

Using the FHD process described in Section 3.2 the vertical structure of the waveguides can be constructed such that there is germanium present in the core layer. In this research we use a phosphogermanate core layer that allows a high germanium content of up to 80 %. The GeO_2 lattice defects absorb light at around 241 nm. When high intensity light at the same wavelength is introduced, the material undergoes changes that correspond to changes of the refractive index [16].

Hydrogen loading can greatly increase the photosensitivity of a sample. In this technique the sample is left in a high pressure hydrogen atmosphere [17]. Hydrogen molecules diffuse into the sample lattice over time. The physical mechanism of why this increases photosensitivity is not well understood. However it has been suggested that in the presence of UV light, the hydrogen dissociates and forms Si−OH or Ge−OH groups in the lattice [18]. As the hydrogen has only diffused into the glass lattice, the gas molecules will eventually diffuse out of lattice once the sample is removed from the H_2 rich environment into atmosphere, a process known as outgassing. Fortunately, this process can be slowed to a negligible rate by storing the sample in a very cold environment such as in a container of liquid nitrogen (LN_2). Once UV-writing processing is complete, the refractive index changes are permanent, and only very small changes to the written refractive index occur once outgassing has finished.

3.4.2 Direct UV-writing

The technique described in this research uses an argon-ion laser that has a strong transition at 488 nm. This laser line is doubled to 244 nm using a barium borate (BBO) crystal, which is close to the high Ge absorption in the sample. The UV-writing system itself focuses two beams whose path lengths differences are well within the coherence length, onto a single spot within the photosensitive sample core. In order to form a stable and static set of interference fringes it is important that there is minimal difference between the arm lengths. These fringes are used to define the periodic refractive index

change that forms a Bragg grating. The Bragg wavelength λ_{Bragg} relates to refractive index changes of period Λ

$$\lambda_{\text{Bragg}} = 2n_{\text{eff}}\Lambda, \tag{3.4}$$

where n_{eff} is the effective index of waveguide. This process therefore allows the UV-writing system to simultaneously write Bragg gratings and waveguides.

During the waveguide writing process the writing system translates the sample across, the spot stays fixed with a static interference fringe pattern. The translation of the sample effectively blurs out the interference pattern exposed onto the surface, thus no periodic refractive index pattern occur. To switch the system into a grating writing mode the system can use a modulation scheme to continuously reinforce the exposed interference pattern as the sample is translated. Two modulation schemes that have been successfully used are the acoustic-optic modulator (AOM) or electro-optic modulator (EOM). The AOM scheme is the simplest and rapidly switches the laser on and off such that the interference pattern is always constructively reinforcing the previous interference fringes as the sample is translated underneath the spot. Apodisation, the modulation of the refractive index fringe strength, can be achieved changing a combination of the sample translation speed and the duty cycle of the AOM helping to ensure fluence matching. The EOM method uses phase control of one arm of the beam to control the interference pattern of the spot. This method will be described in more detail in the next section.

The Bragg wavelength of the gratings is defined primarily by the interference pattern. Varying the angle of the beams when they interfere can be used to change the spatial periodicity Λ of the interference pattern. This angular relationship is given by

$$\sin\theta = \frac{\lambda_{\text{UV}}}{2\Lambda}, \tag{3.5}$$

where θ is the half angle between the two beams and λ_{UV} is the wavelength of the UV laser light (244 nm). This method however is hard to vary during the writing process in a stable manner. However as the UV-writing spot is small (5 µm), this allows for a wide detuning range. Writing at the Bragg wavelength determined by Equation 3.5, the modulation frequency must be selected so that at a particular translation speed the written index fringes constructively reinforce. This frequency however can be perturbed to write gratings at other Bragg wavelengths due to the small spot size, detuning by as much as 250 nm [19].

3.4.3 EOM PHASE MODULATION

The EOM method that is used in this research changes the beam path length of one of the arms during the UV-writing process as can be seen in Figure 3.11. Changing the phase will shift the position of the interference fringes on the focused spot. By careful control of the phase, like with the AOM, the fringe positions can be controlled to reinforce index changes as the sample is translated across. The advantage of this approach is that the technique is intrinsically fluence matched throughout the apodisation profile.

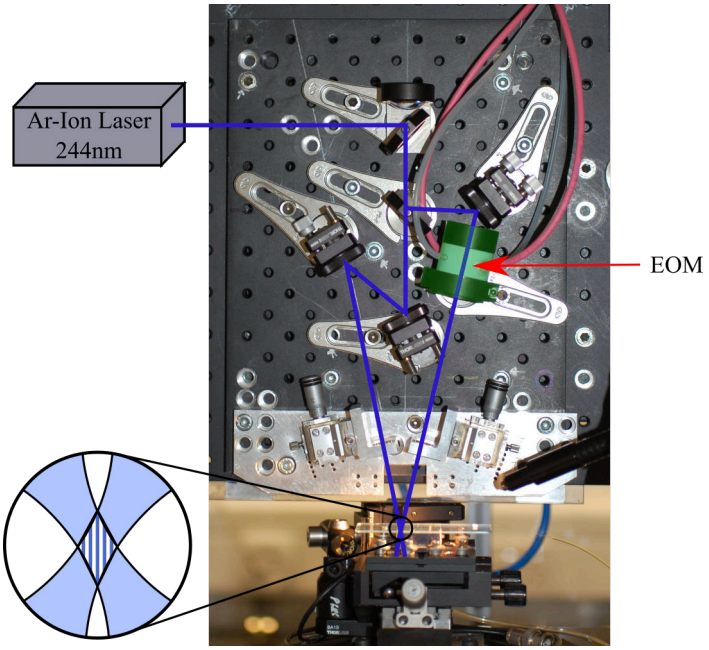

Figure 3.11: Photograph of UV-writing interferometer bread-board with false colour overlay. The 244 nm laser beam paths are indicated in blue. Both arms of the setup are matched as closely as possible to stay within the coherence length. The interference of the beams produces a periodic intensity pattern that is used to define the Bragg gratings as indicated by the close-up inset diagram. Photograph taken courtesy of Dr James Gates.

3.4.4 1651 nm WAVEGUIDE AND GRATING CHARACTERISATION

It is important to characterise the waveguides and gratings in the two planar and IOF platforms used in this research. Characterisation of the platforms is needed so that gratings of a particular strength and wavelength can be written with high accuracy. This is especially important when the gratings need to match spectroscopic lines such as acetylene or methane.

Little previous research using the UV-writing system had been made in the past on phosphogermanate cores and wavelengths close to 1651 nm. This was a prerequisite step before writing the final grating reflector for the laser in order to match the R2 methane gas line. The grating must be placed within ~0.5 nm of 1651 nm and the reflectivity must be high (~80 %). If the periodic grating structure is too strong or long the reflection peak begins to saturate, broadening the reflection spectrum. This places tight tolerances on the grating design so careful characterisation of the wafer is necessary, such as finding the dispersion effects of fluence. The dispersion system uses a broadband source that is guided to the sample and the reflection is measured using an optical spectrum analyzer (OSA) (Figure 3.12). With a polarised source the system under test can be measured for transverse-electric (TE) and transverse-magnetic (TM) response using a 90° mating-sleeve, all the measurements in this section use this system.

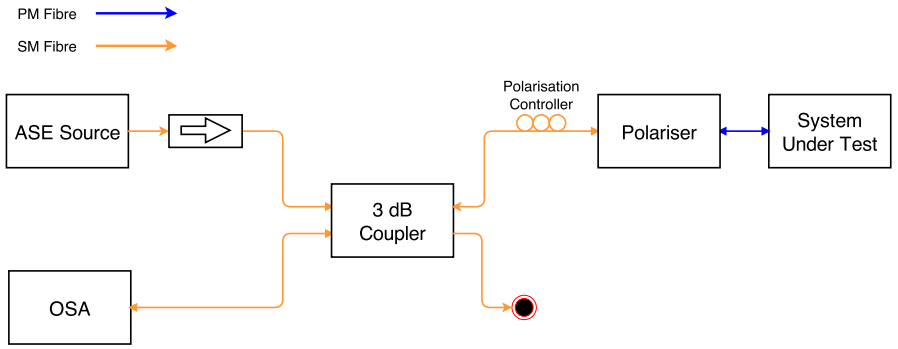

Figure 3.12: System level diagram of characterisation setup. Data from the OSA is collected over GPIB to a computer for data processing. The OSA used is an ANDO 6317b.

3.4.4.1 Dispersion measurement

The dispersion is perhaps the most important characteristic to determine as this allows the fundamental mode's effective index at 1651 nm to be calculated accurately. With the effective refractive index known the correct grating period can be calculated for a grating at 1651 nm. Characterising dispersion involves writing a series of Gaussian-apodised gratings with various grating-periods based on a estimate of the refractive index at 1651 nm. The spectra of the waveguides containing the gratings are taken, with this data Gaussian functions can be fitted to the reflection peaks and a much more accurate value of the refractive index determined [20]. Figure 3.13a shows a typical spectra of the chip, and figure 3.13b shows the calculated dispersion around 1651 nm. This dispersion of the value of n_{eff} is a combination of material and waveguide dispersions.

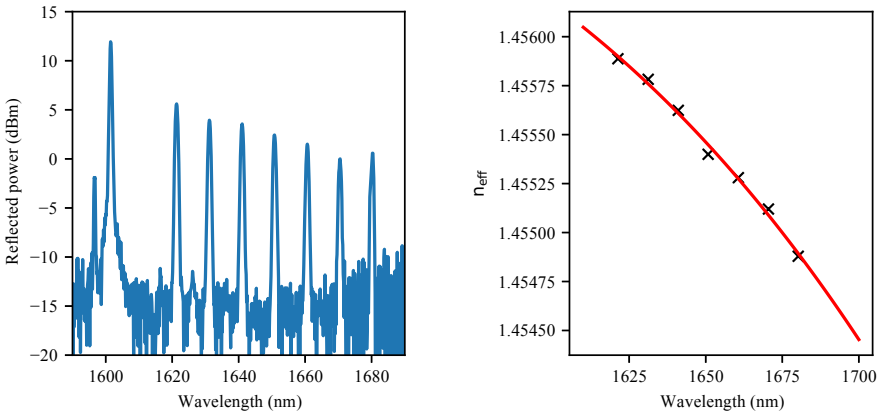

(a) Raw grating data collected using a broadband ASE source. The gratings are gaussian apodised. Noise features on the left most grating, which is the grating nearest the coupling side, come from some of the cladding mode reflection coupling back in.

(b) Dispersion curve, change in n_{eff} with λ_{Bragg}. Sellmeier curve has been fitted to the data points.

Figure 3.13: Reflection spectrum and determined dispersion plot.

3.4.4.2 Fluence measurement

Fluence refers to the total UV energy density delivered to the waveguide. The fluence needs to be characterised to correctly write suitable gratings. The gratings need a maximal reflection, whilst ensuring the spectrum does not saturate. Saturation tends to broaden the full-width at half-maximum (FWHM) bandwidth of the grating and will result in a grating with a reflectivity near 100 %. Characterising the fluence is achieved by writing a number of waveguides with gratings at different fluences, then characterising and numerically fitting gratings in each waveguide. Figure 3.14 shows the results of varying the fluence. It is also important to note how the n_{eff} changes with changing fluence, as this will directly affect the Bragg wavelength of any written gratings, as shown in Figure 3.14a. The n_{eff} generally shows little variation between waveguides however the absolute reflectivity, as seen in Figure 3.14b, has high variability. This is largely due to variation of coupling losses when measuring each waveguide in turn. Despite the variability it can still be seen that a fluence of 12 kJ cm^{-2} would be most suitable as this is the point where saturation starts to onset (in figure 3.14a the curve gradient starts to decrease and in 3.14b it can be seen that the reflective power starts to follow a general decrease).

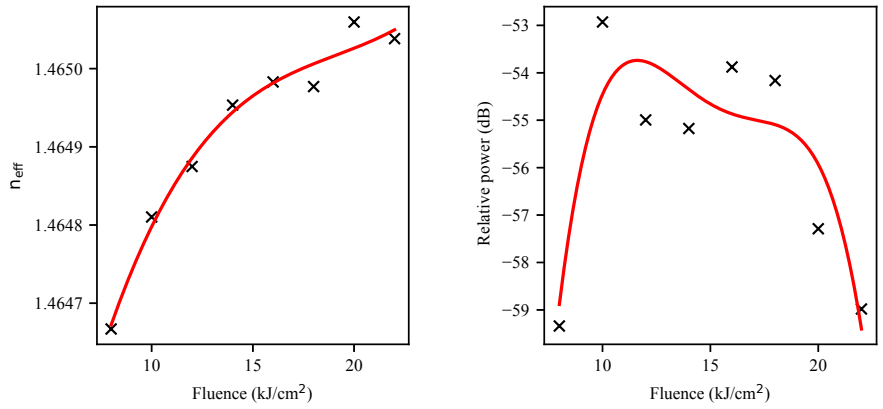

(a) Plot showing how the n_{eff} changes with increasing or decreasing fluence.

(b) Changes in the Bragg grating reflection with changes in fluence.

Figure 3.14: Fluence curves

3.4.4.3 Loss measurement

Bragg gratings can be also used to measure the loss of a waveguide using an *in situ* method [21]. Using the same Bragg-grating arrangement as used for a dispersion chip the strength of each grating is measured from both ends of the chip. Fitting known loss equations to the logarithmic ratio of the amplitudes of each grating and using the absolute locations of each grating the relationship thereof is described by [21]

$$\ln \frac{R_i'}{R_i''} = \ln \nu - 4\alpha_{\text{ab}} x_i, \tag{3.6}$$

where R_i' and R_i'' are the measured reflectivity of the grating i at position x_i. ν includes factors such as losses associated with coupling into and out of the waveguide and is not used in the transmission loss calculation. The LHS is plotted against the RHS of Equation 3.6 as seen in Figure 3.15. From the slope it can be seen that the slope of the plot is linearly related to the loss by the term $-4\alpha_{\text{ab}} x_i$. This method has the advantage that it is independent of the effects of insertion loss, losses associated with detuning and probe power instability, reducing the error of the value. The primary source of error in the value comes from fitting Gaussian functions to the data to determine the strength of the grating, weak gratings do not tend to fit well due to noise from low signal-to-noise ratio (SNR) received from the OSA. The loss value for phosphogermanate waveguides in this instance is (1.350 ± 0.002) dB cm^{-1}, this is a much higher value than expected compared to previously produced waveguides in the author's research group [22] with the lowest value recorded in silica at 0.235 dB cm^{-1}. These waveguides however use a small core layer, with higher indices

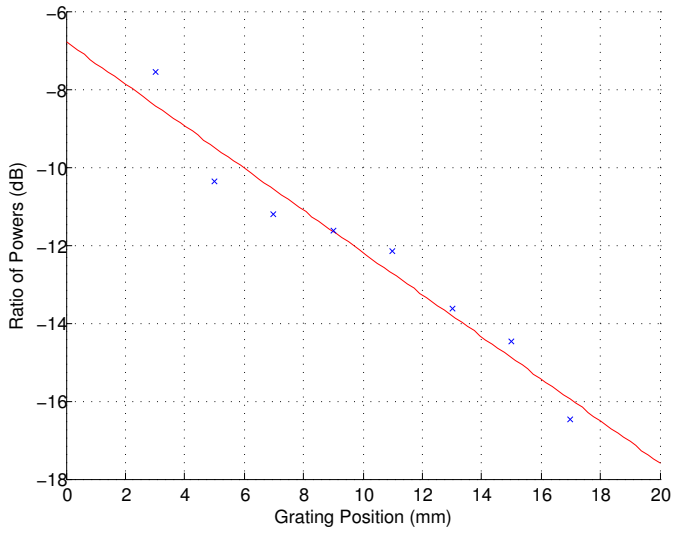

Figure 3.15: Line fitting of loss measurement from data taken on OSA. Once the ratio of grating amplitudes have been taken, a line is fitted whose slope is linearly related to the loss.

Though the loss value is quite high due to the short cavity length the loss contribution from round trip loss of the external cavity will be ~0.9 dB which given a peak gain of 23 dB is acceptable.

3.4.4.4 Birefringence measurement

The planar waveguides deposited using FHD contain stresses between layers, the waveguides were also designed to have strong vertical confinement to improve coupling into the small mode of the gain chip; these two effects affect the refractive index seen by polarisations of the waveguide leading to leading to significant birefringence. Characterisation of this birefringence improves the accuracy that gratings can be written, which for instance, is important when trying to match spectral lines. Using the system shown in Figure 3.12, the polarisation can be switched from the TM mode by using a 90° mating-sleeve to activate the TE mode. Cross-correlation of the TE and TM spectrum was taken showing clearly the change in wavelength leading to a measured birefringence of $\Delta n \approx 4.4 \times 10^{-4}$ (Figure 3.16).

The birefringence and the small difference in reflectivity between the polarisation typically has little effect on the polarisation that laser chooses to lase upon. It is typical, for reasons that will be discussed in Section 4.3.1, for diode based lasers to operate on the TE polarisation.

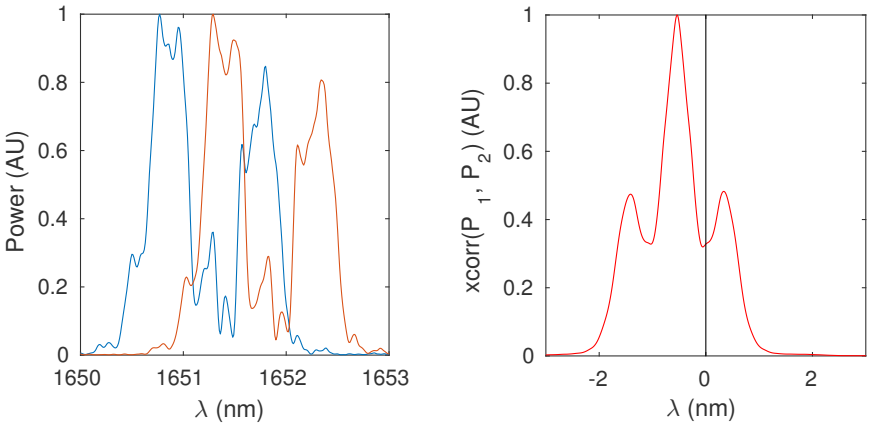

(a) Raw grating spectra of a grating pair used to determine birefringence at 1651.

(b) Cross correlation of the same Bragg-grating before and after the change in polarisation of light. The distance from 0 to the peak shows the change in the Bragg wavelength as a result of the change in polarisation.

Figure 3.16: Birefringence data.

3.4.4.5 Annealing

The thermal stability of gratings is vitally important if they are to be used in a laser cavity and with thermal tuning. If the grating refractive index were to change significantly it could pull the grating too far from the methane gas line making it ineffective for the purposes of methane gas sensing. UV written structures have previously shown ageing and that can be accelerated when exposed to high temperatures [23]. Annealing can be used to make the gratings stable over long time periods and high temperatures by thermally ageing them. When annealed sufficiently the actual working wavelength with time and temperature will be far more stable.

As mentioned before a new phosphogermanate core wafer was being used. The thermo-optical characteristics had not been measured. Some UV-written hydrogen loaded gratings were placed in an oven of 160 °C and taken out periodically to check the change in Bragg wavelength (several measurements are shown in Figure 3.17).

In previous work on hydrogen loaded fibre Bragg gratings, a logarithmic relationship is used to fit accurately between the induced index change and the time spent annealing [24].

A logarithmic law was assumed and is supported by Baker for hydrogen loaded Bragg gratings. Extrapolating the plot to 20 hours leads to a slope of 2.173 pm/h. These

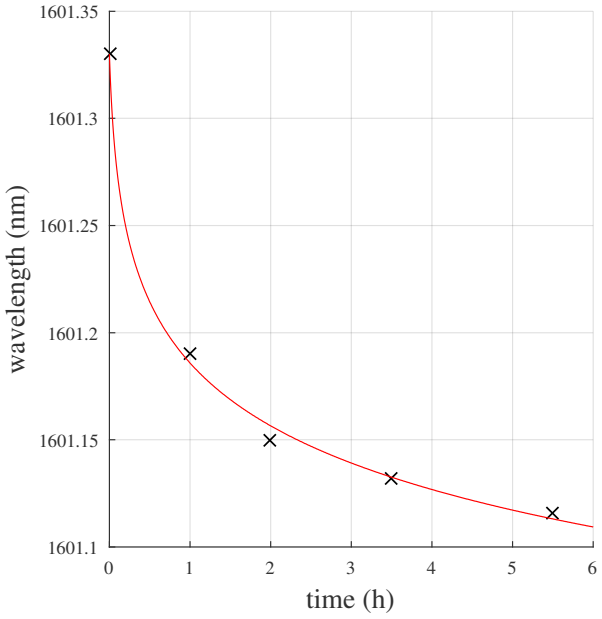

Figure 3.17: The change in wavelength as the grating was annealed with temperature of ~160 °C.

annealing time and temperature was decided to be sufficient as the true core temperature should be lower and for shorter durations.

3.4.5 Writing into IOF

Writing into optical fibre presents additional challenges compared to writing waveguides in planar chips. The cylindrical geometry of fibre presents a non-planar surface that is astigmatic, making it difficult to to achieve optimal focuses of the beam. In addition the internal walls of the fibre provide additional reflection points though this will be mitigated as FHD processing of the fibre will significantly reduce the uniformity of the outermost fibre walls. As a result the UV-light will effectively fill the fibre cross-section rather than concentrating the power into the core effectively increasing the fluence required to write. Nonetheless the laser coherence is maintained and the system still fabricates functional Bragg gratings. It is likely that a consequence of this would be that this would lead to a reduction in detuning bandwidth as the effective spot size that interacts with the core would increase due to the defocusing; though this requires further investigation.

Another challenge to writing into IOF is the straightness of the fibre. The UV-writing system at the time of writing this thesis, has no means to compensate for bends in

the fibre it is writing, so long gratings can run off the length of the fibre if it bends sufficiently. Even when carefully placed on the wafer during the FHD process there is typically a shallow bend that occurs along the fibre.

Despite these challenges the IOF platform provides a mechanically rigid optical platform with a highly uniform waveguide structure along its length that facilitates accurate writing of Bragg gratings.

3.4.5.1 Characterisation of IOF

As with planar waveguides, writing gratings accurately at precise wavelengths such as an absorption line for acetylene at 1530.37 nm or at twice the wavelength of rubidium at 1560.50 nm requires that the fibre is characterised accurately.

The advantage of using a fibre based platform rather than planar for targeting specific wavelengths is that they have an extremely uniform and well specified waveguide structure due to the well established and optimised drawing tower technology used for their fabrication. Planar waveguides show a comparatively high variation of layer thickness: the stresses in the wafer introduce a slight bow to the wafer, additionally after the FHD deposited glass has been sintered the layers are not perfectly flat and contain small surface variations.

The loss and dispersion of the waveguide can be established in a single waveguide as they require the same arrangement of gratings for their measurement. As the losses are expected to be low, a much longer waveguide is used; in this research a 9 cm long waveguide is used for increased accuracy in the measurement.

3.4.5.2 Dispersion measurement

The most important characteristic to determine accurate writing of the gratings was to determine the dispersion characteristics of the IOF waveguide. To determine this dispersion a series of twenty 6 mm unapodised Bragg gratings attempted to be written into fibre at various nominal wavelengths. Five gratings of the twenty failed to write, likely due to impurities present during sintering process after FHD. The resulting dispersion curve can be seen in Figure 3.18. With this information it should be possible to accurately write gratings at specific wavelengths.

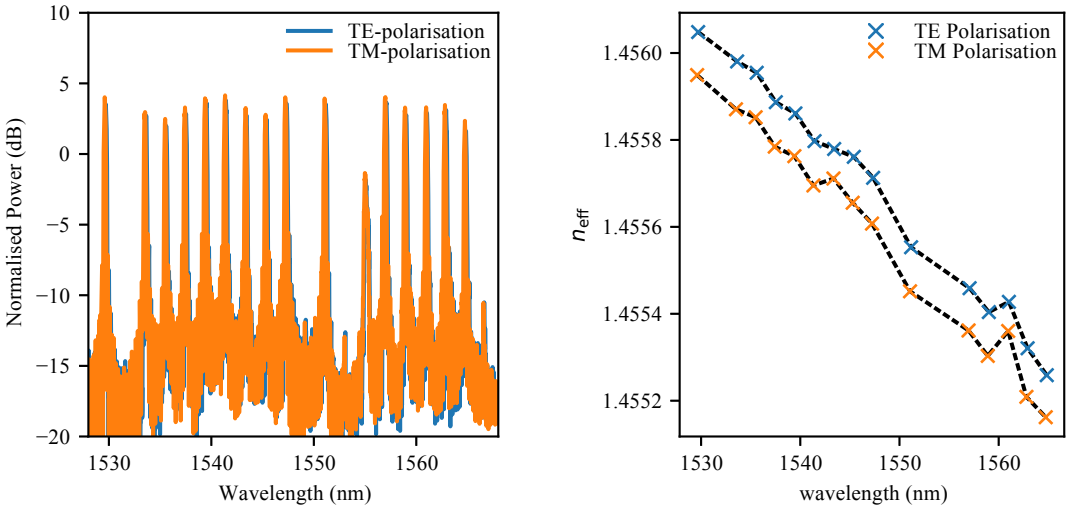

(a) OSA spectrum of the UV-written Bragg gratings. Both TE and TM polarisations (as defined by planar waveguide optics) are included.

(b) The n_{eff} dispersion plot of the TE and TM polarisations.

Figure 3.18: Plots showing the raw OSA collected data and the computed dispersion from the 9 cm long characterisation chip.

3.4.5.3 Loss measurement

As this platform is based on fibre it ought to retain the ultra low propagation losses of fibre waveguides that to date have not been obtained in any other UV-written planar research. The lowest loss waveguides fabricated in direct UV-writing are as low as $<0.2\,\text{dB cm}^{-1}$ [25]. The GF4A fibre supplier does not provide data on the propagation losses though it is expected to be much higher than standard telecommunications fibre due to the presence of boron in the core to enhance photosensitive of the fibre. Despite this the propagation losses should be much lower when compared to typical UV-written planar waveguides. Additional loss will be expected after sintering due to devitrification, however the length of fibre used in this research is short (<10 cm) so losses over this length, due to devitrification, are unlikely to be seen [7].

The loss measurement technique is the same used as that for planar waveguides. To minimise the error for measurements, many gratings were written over a long chip >7 cm. The loss was determined to be $<3 \times 10^{-2}\,\text{dB cm}^{-1}$, only a upper limit of the losses could be determined as the losses were so small. The losses of this chip were contrasted with the best recorded losses found in our planar UV-written gratings; both sets of data are plotted in Figure 3.19.

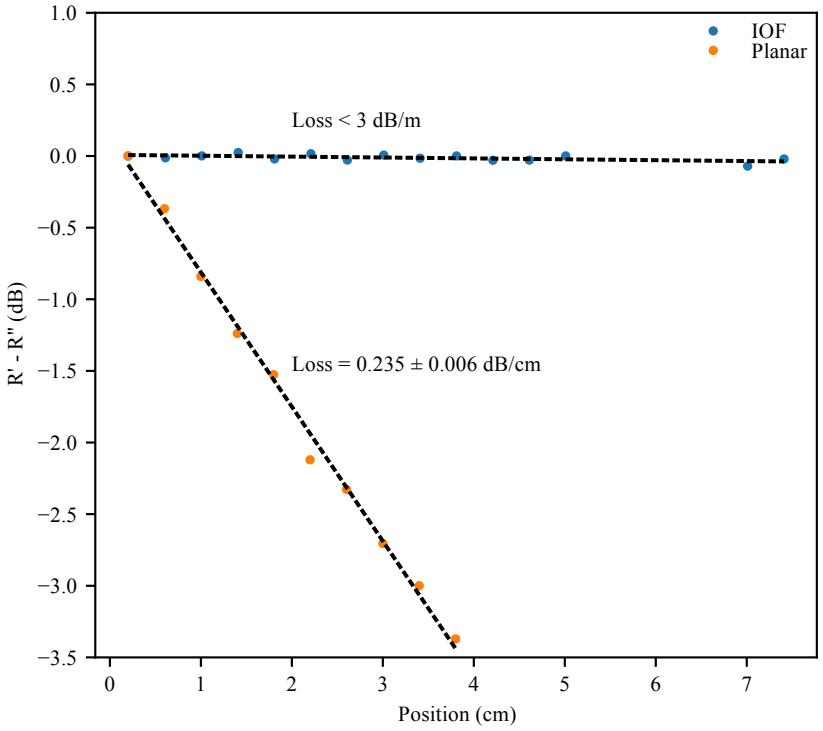

Figure 3.19: A comparison of the losses as light travels through the waveguide in IOF compared to be best recorded losses in our silica waveguides [22]. The IOF has far superior losses clearly retaining the advantages of the fibre based technology.

3.4.5.4 Birefringence measurement

GF4A, a radially symmetric fibre does not have any intrinsic birefringence, however after the FHD process, there is an observable birefringence. It is likely that asymmetric stresses are introduced after the soot has been sintered, resulting in an induced birefringence through similar mechanism to stress rods in polarisation maintaining (PM) fibre. During UV-writing the beams may not fill the section of core being written uniformly, breaking the symmetry of the refractive index structure further affecting birefringence of the waveguide. A sample with several gratings written at a number of different fluences was fabricated; the birefringence of these different gratings is shown in Figure 3.20. From this plot the birefringence decreases with UV-writing strength; the induced birefringence from UV-writing seems to counter the intrinsic birefringence attributed to attaching the fibre to the substrate.

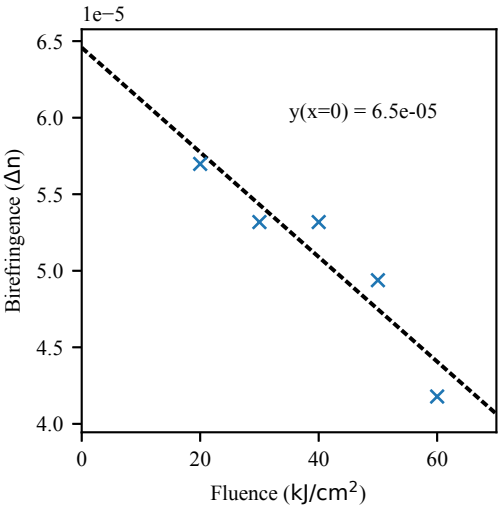

Figure 3.20: The change of birefringence as a function of UV-writing fluence.

3.5 Wavelength tuning micro-heating assembly

This section will describe the process for fabricating the micro-heaters used for thermal tuning of a Bragg grating's working wavelength, including COMSOL modelling of the thermal, electrical and temporal responses of the device.

The author fabricated all micro-heating assemblies discussed in this thesis including COMSOL modelling. The fabrication process was developed by the author alongside the author's colleague Paolo Mennea, who also developed the mask design.

The working wavelength of a Bragg grating is a function of refractive index and periodicity of the refractive index structure. This allows Bragg gratings to be exploited for use in sensing applications particularly in strain and temperature sensing [26], [27]. A consequence for Bragg gratings is the working wavelength can be intentionally moved, in this research the temperature is used to manipulate the wavelength. Temperature affects the refractive index and grating period by exploiting the thermo-optic effect and thermal expansion respectively. The Bragg wavelength change $\Delta\lambda_{\text{Bragg}}$ is related to the temperature change by the equation [28]

$$\Delta\lambda_{\text{Bragg}} = \lambda_{\text{Bragg}}(\alpha_L + \xi)\Delta T, \tag{3.7}$$

where λ_{Bragg} is the Bragg wavelength, α_L is the linear coefficient of thermal expansion, and ξ is the thermo-optic coefficient of the waveguide, and α_L is the coefficient of linear

thermal expansion. For silica the value of $(\alpha_L + \xi)$ value is approximately ~13 pm K^{-1}, this value is also similar for the phosphogermanate glass FHD wafer used in this project.

Heating the grating allows the laser to operate on a wider range of wavelengths by tuning the grating spectrum and also shifts the active longitudinal mode of the laser. The heating microstrip is designed so that it can be rapidly modulated.

The heater design in this device consists of a strip of nichrome deposited directly over the Bragg grating of the device where it is heated with an electric current. The silicon substrate of our device has a high thermal conductivity (149 W m^{-1} K^{-1}) compared with silica (1.4 W m^{-1} K^{-1}). This allows the silicon substrate to function as a heat sink rapidly dispersing the heat. As glass has much lower thermal conductivity than silicon, the FHD-deposited upper clad was made to be thin (7 µm) helping to transport the heat to the waveguide. These steps are important for localised heating of the microstrip and for rapid modulation of the waveguide.

The heating element is estimated to be 300 nm thick based on surface profiling measurements taken on the actual deposited thickness. To obtain an estimation of the measurements of the waveguide structure a commercial Metricon prism coupler system is used to determine the layer thicknesses. The system uses a glass prism that is pressed into the surface of a clean wafer. Laser light is directed into the prism at a range of angles. As the angles are swept the light couples into the planar waveguides at various angles. The points at the which coupling is achieved can be used to infer the thicknesses and refractive indices of the waveguide structures. Based on measurement from the Metricon system the upper cladding, core and under cladding were estimated to be 7 µm, 3 µm and 15 µm respectively.

3.5.1 Modelling heat flow and time response

To aid the design process of the thermal heaters, a COMSOL model was developed of the expected cross-section based on a priori knowledge and measurements. This model helped develop a suitable geometry that could be fabricated practically. Figure 3.21 shows a heat-map model of the fabricated heaters. The heat-map represents the steady state response when 0.4 W of heat is generated from the heater, leading to an average temperature of ~91 °C in the core region.

The time response of heater element was modelled in COMSOL. Specifically the cross section of the wave guide and heating element is modelled. By modelling how the heat transfers to the core and and how well the heat is sunk through the rest of the structure

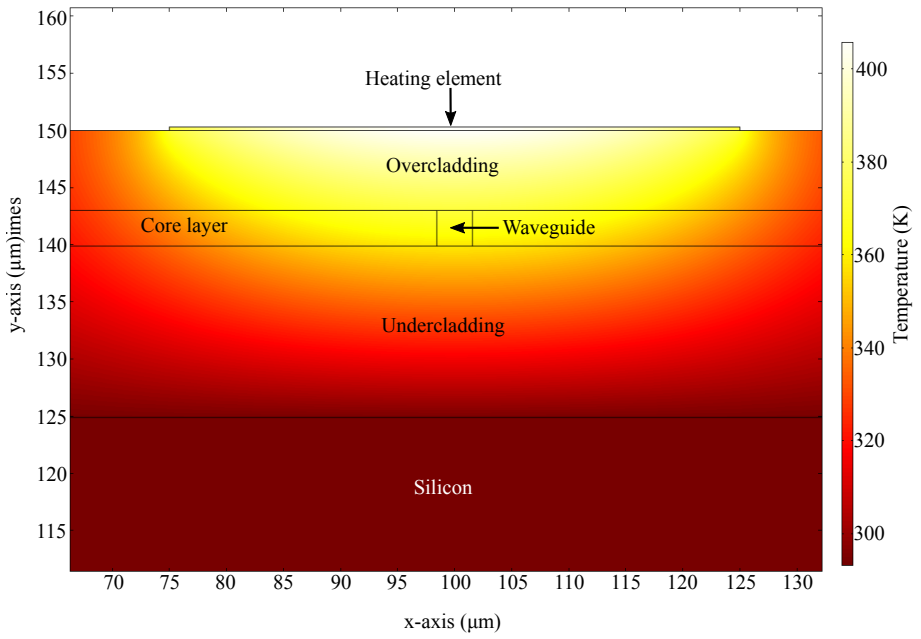

Figure 3.21: Heat map of thermal heating of device with heating element. Core region is square in middle. The very thin rectangle at the top is the heating element itself. The bottom rectangle is the silicon substrate.

the frequency response of the system can be determined. The frequency response of this device was determined by modulating the COMSOL model with a 200 µs square pulse. The average heat over the area of the core was plotted in time where the time data was fitted using a linear time-invariant (LTI) model. The model was assumed to be a simple low pass filter model which in the time domain is represented as

$$T_0 + T_{\max}\left[H(t)\left(1 - e^{\frac{t}{\tau}}\right) - H(t - t_{\text{pulse}})\left(1 - e^{\frac{(t-t_{\text{pulse}})}{\tau}}\right)\right], \tag{3.8}$$

where $H(t)$ is the Heaviside step function, τ is the time constant, t_{pulse} the length of the rectangular pulse, T_{ss} is the steady-state temperature of the core reached from this input pulse and T_0 is the ambient (room) temperature. The fit of this LTI to the time data can be seen in Figure 3.22a.

This model can be transformed into the frequency domain and has the frequency response function

$$\frac{1/\tau}{2\pi i f + 1/\tau}, \tag{3.9}$$

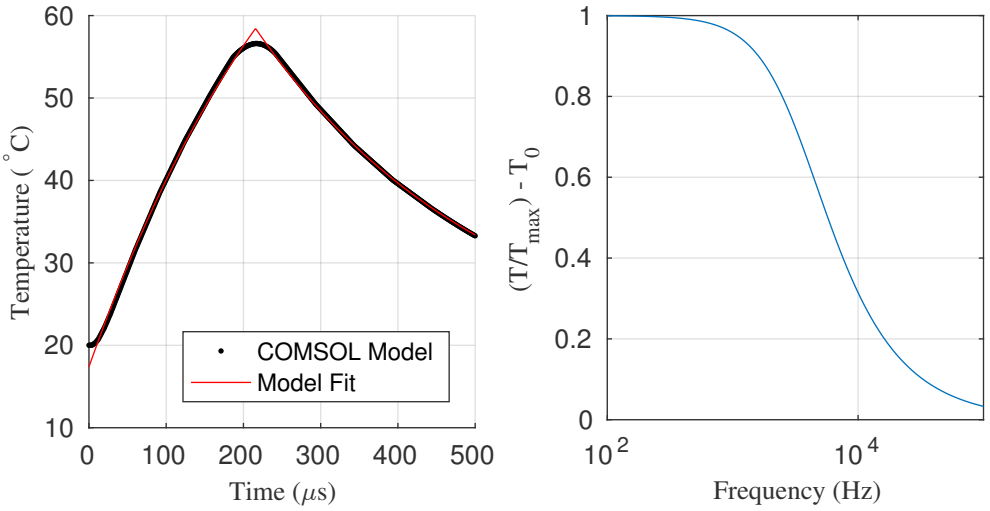

(a) Fitting of Equation 3.8, to find parameters for the LTI model.

(b) Magnitude frequency response of the fitted LTI from Equation 3.8

Figure 3.22: Finding the frequency response of the thermal heater using an LTI model.

where i is the imaginary unit, and f is frequency. The magnitude of this response function is shown in Figure 3.22b. The 50% of the maximum modulation depth is found at ~500 Hz.

The power density of the overall heating elements was also modelled using COMSOL. In this model a two dimensional overview of the heater was investigated. This was to look at how uniform the heating would be across the Bragg grating (Figure 3.23). Non uniformity would correspond to chirp, broadening the Bragg spectrum.

Most of the joule heating occurs in the bridges to the central strip, especially at the corners where the highest values are found. There is a 145 mW mm^{-1} difference between segments of heating strip of highest and lowest power per unit length. This is quite significant difference, fortunately the nichrome strip has a high thermal conductivity (11.3 W m^{-1} K^{-1}) compared to silica ((~1 W m^{-1} K^{-1})) and acts to help equalise the thermal differences.

The heater modelling demonstrates significant heating of the core facilitating tuning of the Bragg grating wavelength. The frequency response of the heaters is fast enough that it could be suitable for locking experiments and modulation of the laser wavelength.

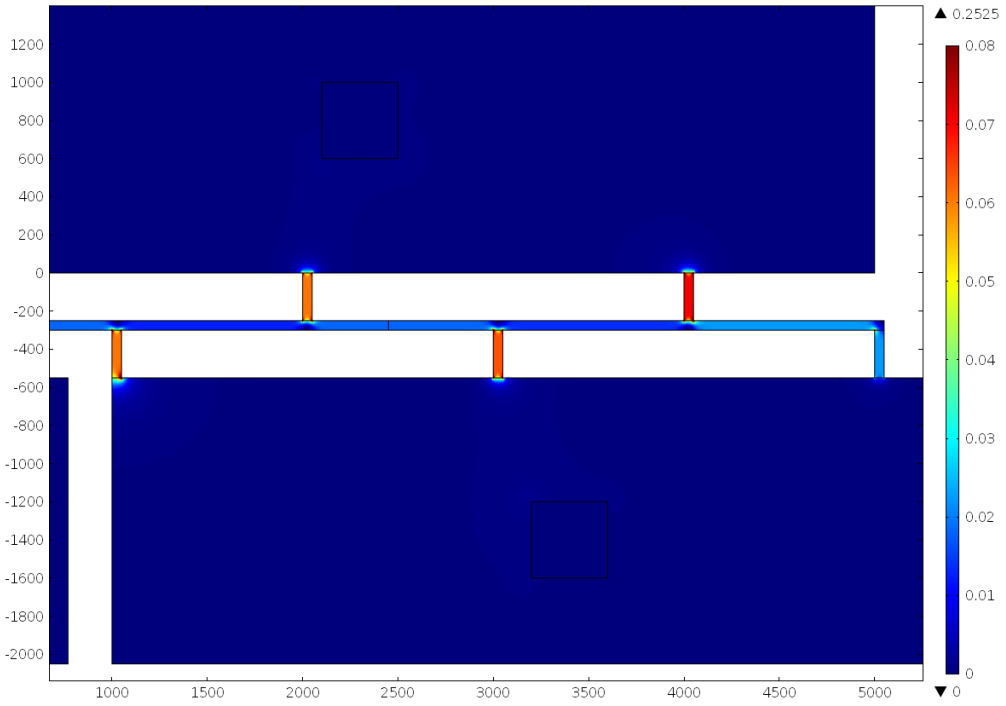

Figure 3.23: Heat map of power density in the device. The units are in $\mathrm{mW\,\mu m^{-1}}$.

3.5.2 Photolithography and deposition

The planar platform offers the opportunity for lithographic processing allowing the deposition of various patterns over the waveguide device. The flat surface makes it ideal for contact-photolithography - a process that allows arbitrary patterns to be defined onto the surface of a substrate that can be later exploited in further processes such as etching and deposition. In previous research a nichrome heating element was fabricated over a cross-coupler arm for a tuneable photonic Hilbert-transformer device [29]. In this research we are interested in being able to thermally tune the Bragg grating using a heater in close proximity and directly over the grating.

The photolithography technique uses UV light with a mask to selectively expose a substrate with a layer of photoresist. The photoresist is a chemical, that after exposure to UV light, can be selectively removed using a chemical known as a developer. The resist is usually dropped on top of the substrate and spun to make a uniform layer that is then baked solid. In contact-photolithography the photomask, a glass plate that has a desired pattern bonded onto it, is placed into direct contact with the sample selectively masking the substrate from exposure. Once the process is complete a substrate is left with the photoresist selectively protecting the desired regions of the sample.

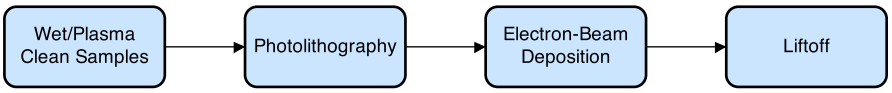

Figure 3.24: Flow process diagram showing the steps performed in the clean-room

The waveguide and Bragg grating are first written using the UV-writing process described in Section 3.4 on a 20 mm × 20 mm chip. The large chip surface makes it easier to place a uniform coating of photoresist onto the chip.

The samples are scrubbed with acetone, then dipped sequentially in acetone, isopropanol and then rinsed with deionized water. Next, using a mixture of hydrogen-peroxide and sulphuric acid known as piranha solution, the sample is cleaned of any organics. As a final step, the sample is then cleaned using a plasma-asher, a chamber with a low-pressure oxygen atmosphere that ionises removing any other organics. These cleaning steps ensure that in the final deposition stage the nichrome will adhere.

The sample is processed using contact-photolithography using the mask design shown in Figure 3.25. The photo resist used is S1813 [30] a positive photoresist where the exposed resist is removed after developing using MF-319. The blue areas in Figure 3.25 show where the resist is removed.

The sample is then transferred to the E-beam deposition tool. This tool fires an electron beam into a crucible of metal, under high vacuum, vaporising it and depositing it onto the substrate. In this process two metals are deposited: the first metal is ~10 nm chromium as an adhesion layer that helps subsequent layers to stick; then the final layer is a nichrome ($Ni_{0.2}Cr_{0.8}$) where ~300 nm of metal is deposited.

The final process step is known as lift-off, in this step the sample is placed into a bath of acetone until the remaining hardened photoresist dissolves, removing all excess nichrome deposited and leaving behind just the patterned nichrome heaters. The sample is then rinsed with deionised water.

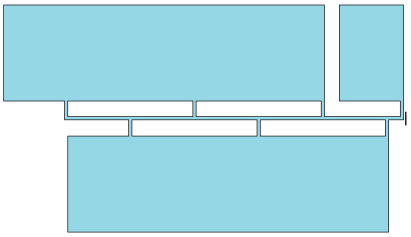

Figure 3.25: Design of heater layout that is on chrome mask. The design comprises of 3 pads, the largest is the ground pad, the smallest controllers the phase-shift heater and the larger controls the grating heater.

3.6 Wire bonding electrical connections

Once the heaters have been fabricated on the external cavity chip it is necessary to have a suitable method to supply electrical current to the heaters. Nichrome forms a nickel oxide layer on its surface that makes it impossible to solder or bond. In addition, solder would also be unsuitable as being in close proximity to heaters could cause the solder to melt. Finally the thin film of nichrome metal could easily allow migration of the solder metal making it more prone to failure from chemical changes. One solution is to fix a suitable breakout board in close proximity to the device that where current is supplied using conventional insulated wires and then using wire bonds to the heaters themselves. Wire bonding is also a key process for the assembly of the custom packages that are described in Section 3.7.3 as the supplied gain chips require small electrical connections to be made, practical only using a wire bonder.

The wire bonding used on the micro-heating assemblies was carried out by Dr Hwanjit Rattanasonti. Wire bonding and optimisation of the process of the packaged device was carried out by the author.

3.6.1 Wire bonding process

Wire bonds are point-to-point connections using thin, usually 25 µm gold or aluminium wires. There are two main types of wire bonding: wedge and ball. In both types a tool resembling a needle containing a capillary positions a thin wire over a bonding pad and welds it into place. Ball bonding is a newer, more versatile form of bonding but is limited to gold wire as the ball is formed at high temperatures using an arc discharge that would oxidise Al.

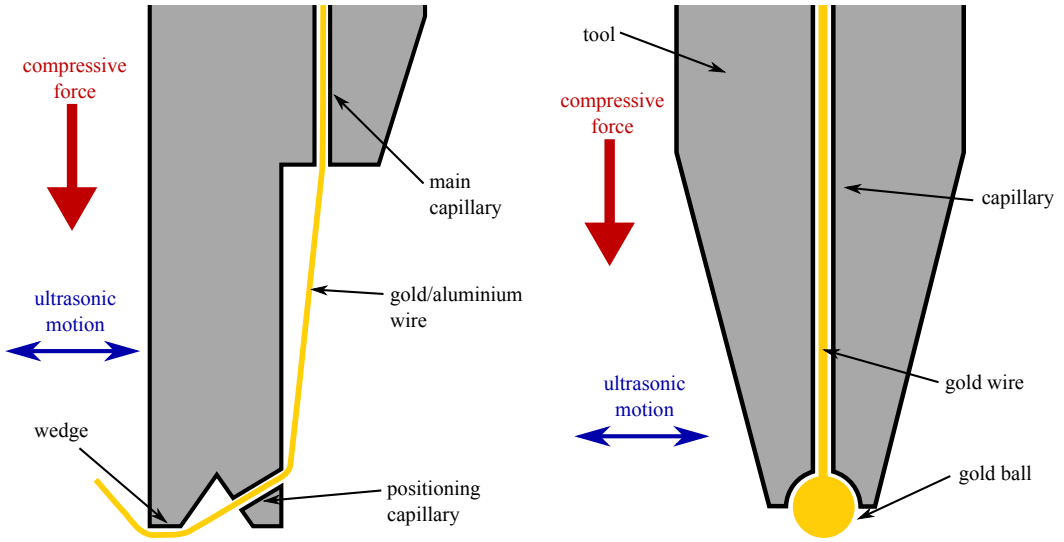

(a) The capillary feeds the wire to the tip. A secondary capillary positions it underneath the wedge. As the wire must be positioned underneath the wedge tool, once the first bond has been made the second bond must be behind the tool, or to the right of the tool in this depiction, consequently the tool cannot tolerate much angular deviation otherwise the wire may slip from underneath the wedge.

(b) Due to the ball formed at the tip of the wedge the structure is a simple capillary with a socket to hold the ball. The geometry means the ball bonding tool can move in any direction after the first bond, increasing its flexibility.

Figure 3.26: Cross-sectional diagrams of ball and wedge bonding tools.

During the bonding process a wire bonding tool is pressed down compressing the wire between the tool and the pad, where the tools are depicted in Figure 3.26. The tool then vibrates ultrasonically, where the ultrasonic energy causes the wire to weld to the pad it is pressed to. Gold wire requires elevated temperatures to form bonds using wedge or ball wire bonding. A description of wire bonding phy mechanisms will be not covered and the author recommends Harman for further details [31].

There are a number of factors that affect the bondability and reliability of a wire bond. One of the primary difficulties with wire bonding is the choice of wire and pad materials. Only certain combinations of materials will permit reliable bonding, ideally the wire and pad materials will be the same providing the most reliable connections. Bondability is also affected by the hardness of the substrate material that the electrical contact is attached to as it can dissipate ultrasonic energy, for this ceramics are often used as a substrate for their hardness.

In this thesis, aluminium wedge bonding was primarily used. The heating assembly used a printed circuit board as a breakout for conventional wires. Aluminium wire-bonds are able to bond to printed circuits boards more easily as the bonding can be formed at

room temperature. At high temperatures that are used in gold bonding usually take the plastic substrates used in printed circuits close to or over the T_g causing the substrate to soften significantly, resulting in too much dissipation of the ultrasonic energy making the gold bonding difficult.

Aluminium was also selected to make the connections between the gold contact on the gain chip and the gold breakout pads, despite that gold wire-bonds would provide higher reliability on gold surfaces. As will be described in the next section the gain chip and the wire bondable breakout contact was adhered to a silicon mount using a UV-curable adhesive called OP-67-LS [32], where the T_g is below 150 °C. The softening of this adhesive would allow too much movement during wire bonding making it difficult to bond. Additionally, it is convenient during the packaging for the silicon mount to be attached to the Peltier cooler before wire bonding, which can not be heated to 150 °C without damaging the Peltier cooler.

3.7 System assembly

This section will consider the assembly of the external cavity chip hosting the Bragg reflector that is coupled with gain chip. The importance and consideration taken for return losses is described. The two assemblies used: a linear translation staged based system, and then a smaller, more portable and stable packaged system will be outlined.

All the laser systems assembled on translation stages and also the packaged system was undertaken by the author.

Fibre provides a convenient means to integrate into larger optical systems, as many fibre components can be easily sourced and conform to standardised connectors. So light output from the laser systems considered is coupled out using a standard PM fibre pigtail for 1550 nm. The pigtail is a commercial PM fibre that is mounted in an 8° angle polished, V-groove assembly for high return losses from Oz-Optics. The V-groove is attached to the external cavity chip using an optical quality UV-curing adhesive (Dymax OP-4 [33]). The MFD of the planar waveguides should be well relatively matched to that of the PM fibre (<1 dB loss), whereas the IOF chip has a considerably smaller MFD resulting in considerable loss when coupling light out of the laser device. For the IOF, assuming the mode fields are approximately Gaussian in shape and assuming a negligible gap between the two devices the loss due to modal overlap is 3.5 dB.

3.7.1 Engineering return losses

A key issue in lasers and particularly in diode laser systems is elimination of unwanted optical feedback. Even low optical feedback from distant reflections can make the laser enter into unstable regimes characterised by frequent mode hoping and optical power fluctuations [34]. Diode lasers are very sensitive due to their high gain and generation of carriers with incident light affecting the gain and index. It is not unusual for the laser system to be sensitive to sources of reflections even when component return losses are as high as 50 dB [35]. Though carefully controlled distant optical feedback can be used to force the linewidth to become narrower [36].

It is essential that laser systems incorporate an optical isolator to attenuate any back-reflections [35]. Typically a Faraday isolator is preferable that is physically near to the laser system to minimise distance of reflections from the isolator itself. Many optical components have significant return loss, even matings of ultra physical contact (PC) fibres can contribute significant unwanted back-reflections. Often the phase of these reflections not be stable stable due to environmental vibrations, thermal fluctuations etc. occurring within the "external" cavity. As a result the laser mode will be likely to hop frequently and uncontrollably between these parasitic external cavity modes. In commercial laser packages it is common for the isolator to be incorporated into the laser package prior to output coupling.

In this system it is been sufficient for a fibre isolator to be included <50 cm away from the laser with >40 dB of isolation. This was achieved at first by placing an attenuator before an isolator as this provides twice the attenuation of isolation in addition to the isolator, for example a 10 dB attenuator followed by a 30 dB isolator provides 50 dB total isolation. All optical connections leading to the isolator must use an APC connector or be directly spliced.

3.7.2 Linear stage based system

The prototype laser system is built on a set of precision translation stages from Thorlabs. The external cavity is mounted in a fibre array holder. The gain chip is pre-mounted onto a heatsink which has been bolted into a custom aluminium block that holds a thermistor. This block has then been adhered onto a Peltier device.

The external cavity is aligned into position by monitoring out-coupled optical power. The injection current is set to a level where the laser is unlikely to lase but there is

enough power to monitor the spontaneous emission power. The system is difficult to align once lasing as the adjustments affect the cavity length, having a strong effect on the output power. Once aligned the power can be increased, often minor adjustments are needed to compensate for the effects of thermal expansion. The final prototype system can be seen in Figure 3.27.

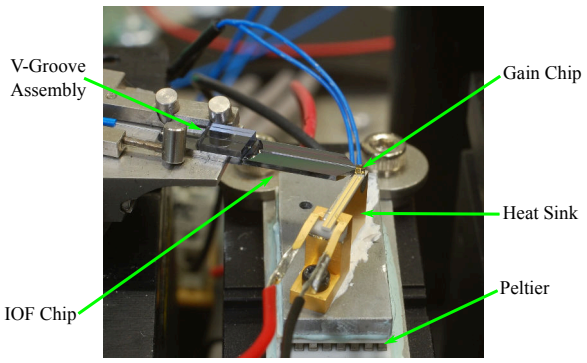

Figure 3.27: Photograph of prototype laser system built using linear translation stages.

3.7.3 Packaging of laser system

Ideally the entire system would not have to use large translation stages that are susceptible to thermal drift, but integrated onto a single mount inside a compact housing. There are numerous advantages to integration over the prototype system:

- Compact and portable - using translation stages for alignment makes the system large, heavy and cumbersome. The small and light size of the laser makes it simple to move and handle.
- Vibrationally stable - Having all the components held rigidly in close proximately eliminates the number of vibrational modes that can affect the system. The enclosure will also reduce air currents that would add additional vibrations to the system.
- Thermally stable - Like the vibrational stability, having the components held closely together with good thermal conduction. Matching of thermal expansion will reduce drift of components due to thermal drift.
- Cleanliness - Enclosing the system prevents the build-up of dust on the system that could introduce significant loss if particulates settle on the laser facets.

- Electrical Isolation - A metallic housing will reduce external electrical noise whilst also reducing circuit inductances when modulating the system.
- Protection - The housing provides a rigid and strong shell to protect from any accidental impacts.

As the external cavity is contained in a single mode waveguide, and the light is coupled out using a fibre pigtail, the entire system is devoid of any conventional free-space optics. Having no free-space components should improve the stability of the system as it limits the capacity for drift between components in the system. A further advantage of lacking free-space components is the increased simplicity of assembly.

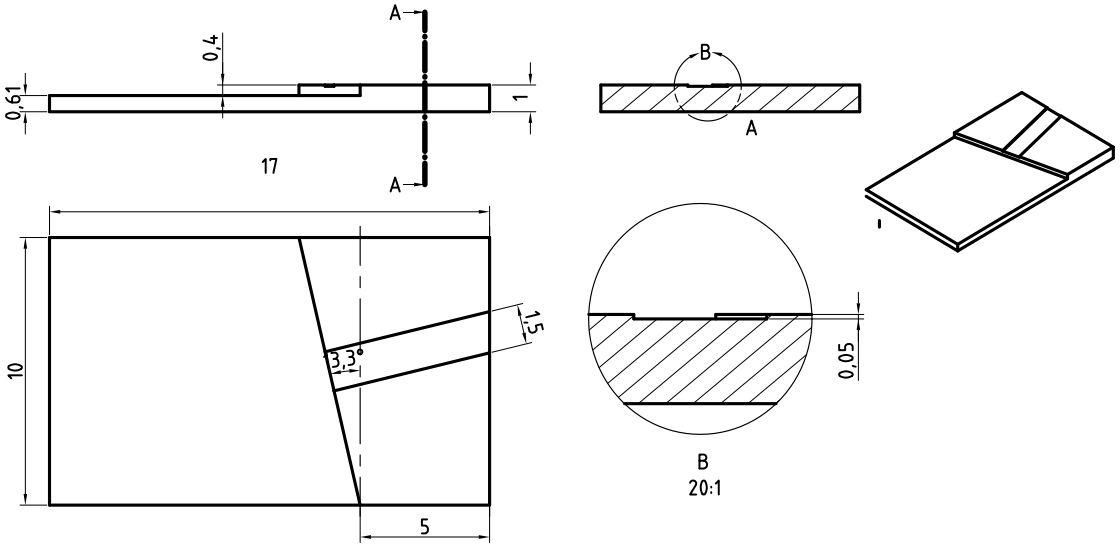

Figure 3.28: CAD drawing showing the dimensions of the silicon mount that the device will be bonded to. All dimensions are in mm unless specified otherwise.

In contrast to the stage based system the components are fixed to a silicon mount using low shrinkage UV-curable adhesives. The design of the silicon mount can be seen in Figure 3.28. Silicon was chosen for the mount, as the material is easily machined (using the MicroAce 3 dicing machine). Silicon has a desirable linear coefficient of thermal expansion (LCTE) as it is well matched to the gain chip substrate and has excellent thermal conductivity. The sub-mount material of the gain chip is silicon carbide, which has an LCTE of $4 \times 10^{-6}\,^{\circ}\mathrm{C}^{-1}$ and matching closely to silicon that has an LCTE of $3 \times 10^{-6}\,^{\circ}\mathrm{C}^{-1}$. For comparison, aluminium as a base-mount material has an LCTE of $22.2 \times 10^{-6}\,^{\circ}\mathrm{C}^{-1}$; using silicon as the base-mount to reduce effects from thermal drift.

The unenclosed system is depicted in Figure 3.29. The following steps describes the assembly process of the packaged laser system. It is assumed that the external cavity

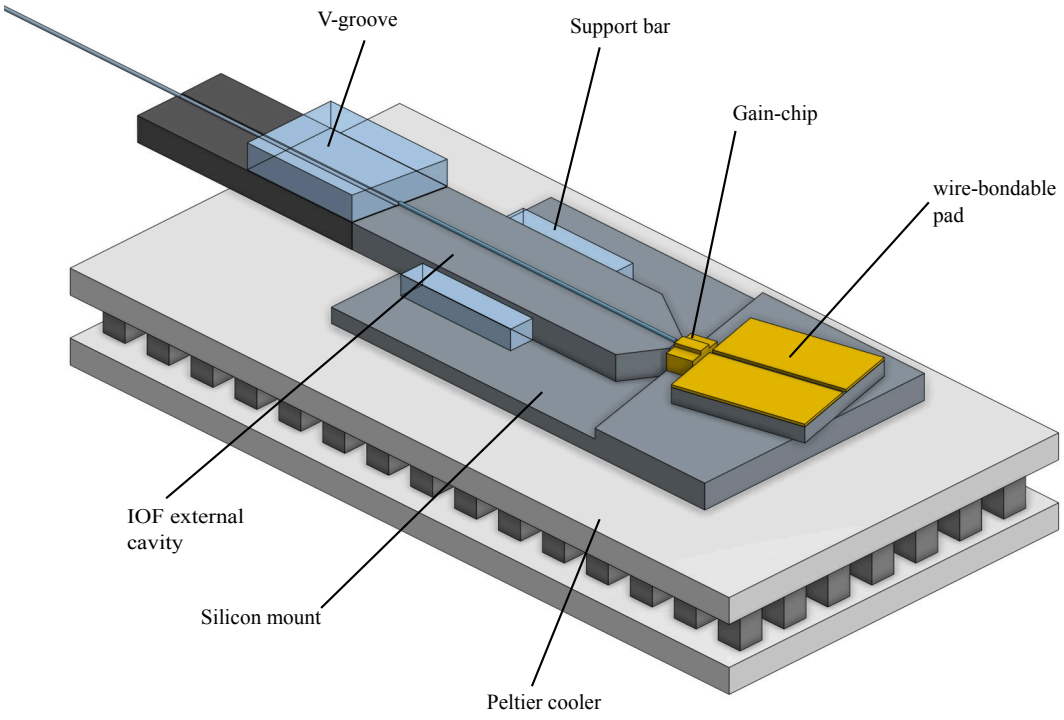

Figure 3.29: 3D CAD diagram of unenclosed laser system on silicon mount and Peltier.

chip is fabricated with a pigtail attached, using the techniques described from Section 3.2 to Section 3.5.

1. The base-mount is diced to shape as shown in Figure 3.28.
2. The base is placed on top of a Peltier device and adhered using a thermally conductive epoxy. A thermistor is then attached onto the Peltier close to where the gain chip will be seated.
3. The gain chip is placed onto the silicon base with thermal paste inserted between the chip and base. The chip is then bonded in place using a UV-curable adhesive.
4. A set of gold wire-bondable pads is fixed adjacent to the gain chip. 25 µm aluminium wire is then wedge-bonded between the pads and gain chip. Break out wires are then soldered to the pads.
5. The silicon base is then fixed to a platform where the external cavity chip can be aligned to it using a linear translation stages similar to the prototype design. The gain chip must have a small current such that the system remains below threshold. The external cavity is aligned until it maximises optical power. A

small air gap is maintained between the external cavity and the gain chip to avoid damage to the gain chip facet due to movements of either chip.

6. There is a significant gap between the chip (~0.5 mm) and the silicon base to account for higher errors from vertical position of the dicing system in addition to providing additional room for fine angular alignment. Though the UV-curable adhesive (OP-67 [32]) is designed to be low shrinkage (0.08 %) it is not possible to directly adhere the external cavity chip directly to the silicon base. This gap will allow for a significant height change upon curing, misaligning the system, as the gain chip vertical mode height is likely to be <2 µm. To minimise this effect, two structural glass bars with a small amount of UV-adhesive on one face of each bar is placed on either side of the cavity chip with the adhesive touching the sides of the chip. Glass is used as it is transparent to the curing light. This ensures a small gap between the structural bars and the silicon base. The bars are then cured to the silicon base.

7. The aluminium enclosure has a hole drilled for the optical fibre output and a hole for the electrical feeds. The electrical feed connector is then adhered to the electrical feed hole.

8. The fibre pigtail is cut and a strain relief boot is attached to the fibre. It is then threaded through the fibre optic feed hole in the housing. The laser device is lowered into the enclosure whilst threading additional fibre through the enclosure. The laser device is adhered to the base of the enclosure using a thermal epoxy. and the wires soldered to the electrical outputs. The fibre boot is adhered in place using epoxy.

9. The fibre end that was cut off is fusion spliced to a Faraday isolator (ensuring that the connector is APC).

10. The lid is firmly screwed in place.

3.8 Conclusion

This chapter has outlined the main fabrication processes used to fabricate and assemble all the devices used in this thesis. The FHD process was described that is used to fabricate the IOF and planar optical platforms used in the construction of devices in this thesis. The high precision dicing of these optical platforms into suitable geometries is described, and the ductile dicing process to obtain smooth optical surfaces and the

method to characterise roughness is also covered. A description of the UV-writing system and process is given for IOF and planar geometries, the methods to characterise UV-written gratings to achieve accurate writing are given. The fabrication process steps of the NiCr heating assembly used for wavelength tuning on the planar geometry are stated. The wire bonding process and factors affecting the reliability of bonds are outlined. Finally the steps and considerations of assembling the ECDL systems are explained. In the next two sections the characterisation of the assembled lasers will be outlined.

Bibliography

[1] W. A. Gambling, "The rise and rise of optical fibers," *IEEE J. Sel. Topics. Quantum Electron.*, vol. 6, no. 6, pp. 1084–1093, 2000.

[2] K. D. Simmons, D. L. Griscom, S. LaRochelle, V. Mizrahi, and G. I. Stegeman, "Correlation of defect centers with a wavelength-dependent photosensitive response in germania-doped silica optical fibers," *Opt. Lett.*, vol. 16, no. 3, pp. 141–143, Feb. 1991.

[3] S. Sakaguchi and S. Todoroki, "Light scattering properties in ternary germanate glasses," *Japanese J. Appl. Phys.*, vol. 34, no. 1R, p. 145, 1995.

[4] B. E. Deal and A. Grove, "General relationship for the thermal oxidation of silicon," *J. Appl. Phys.*, vol. 36, no. 12, pp. 3770–3778, 1965.

[5] A. S. Sudbo, "Film mode matching: a versatile numerical method for vector mode field calculations in dielectric waveguides," *Pure Appl. Opt.*, vol. 2, no. 3, p. 211, 1993.

[6] C. Holmes, J. C. Gates, and P. G. R. Smith, "Planarised optical fiber composite using flame hydrolysis deposition demonstrating an integrated FBG anemometer.," *Opt. Express*, vol. 22, no. 26, pp. 32 150–7, 2014.

[7] A. Rose, "Devitrification in annealed optical fiber," *J. Lightw. Technol.*, vol. 15, no. 5, pp. 808–814, 1997.

[8] I. Hatakeyama, M. Tachikura, and H. Tsuchiya, "Mechanical strength of fusion-spliced optical fibres," *Electron. Lett.*, vol. 19, no. 14, pp. 613–614, 1978.

[9] L. G. Carpenter, "Precision dicing and micromilling of silica for photonics," PhD thesis, University of Southampton, 2013.

[10] Thorlabs, *SAF1091H*, https://www.thorlabs.com/drawings/9db894c8c4f909ae-4EDD0C9A-5056-0103-793DF05996684538/SAF1091H-AutoCADPDF.pdf.

[11] H. E. J. Bennett and J. O. Porteus, "Relation between surface roughness and specular reflectance at normal incidence," *J. Opt. Soc. Am.*, vol. 51, no. 2, pp. 123–129, 1961.

[12] L. G. Carpenter, H. L. Rogers, P. a. Cooper, C. Holmes, J. C. Gates, and P. G. R. Smith, "Low optical-loss facet preparation for silica-on-silicon photonics using the ductile dicing regime," *Journal of Physics D: Appl. Phys.*, vol. 46, no. 47, p. 475 103, Nov. 2013.

[13] K. W. Shi, K. Yow, and R. Khoo, "Investigations of the effects of blade type, dicing tape, blade preparation and process parameters on 55nm node low-k wafer," in *Electronic Manufacturing Technology Symposium (IEMT), 2010 34th IEEE/CPMT International*, IEEE, 2010, pp. 1–6.

[14] G. Emmerson, S. Watts, C. Gawith, V. Albanis, M. Ibsen, R. Williams, and P. Smith, "Fabrication of directly UV-written channel waveguides with simultaneously defined integral Bragg gratings," *Electron. Lett.*, vol. 38, no. 24, pp. 1531–1532, 2002.

[15] C. Sima, "Integrated planar Bragg grating devices for advanced optical communication systems," PhD thesis, University of Southampton, 2013.

[16] R. M. Atkins and V. Mizrahi, "Observations of Changes in UV Absorption Bands of Singlemode Germanosilicate Core Optical Fibres on Writing and Thermally Erasing Refractive Index Gratings," *Electron. Lett.*, vol. 28, no. 18, pp. 1743–1744, 1992.

[17] P. J. Lemaire, R. M. Atkins, V. Mizrahi, and W. A. Reed, "High Pressure H2 Loading as a Technique for Acheiving Ultrahigh UV Photosensitivity and Thermal Sensivity in GeO2 Doped Optical Fibres," *Electron. Lett.*, vol. 29, no. 13, pp. 1191–1193, 1993.

[18] B. Malo, J. Albert, K. Hill, F. Bilodeau, and D. Johnson, "Effective index drift from molecular hydrogen diffusion in hydrogen-loaded optical fibres and its effect on Bragg grating fabrication," *Electron. Lett.*, vol. 30, no. 5, pp. 442–444, 1994.

[19] C. Sima, J. Gates, and H. Rogers, "Ultra-wide detuning planar Bragg grating fabrication technique based on direct UV grating writing with electro-optic phase modulation," *Opt. Express*, vol. 21, no. 13, pp. 15 747–15 754, 2013.

[20] H. L. Rogers, C. Holmes, J. C. Gates, and P. G. R. Smith, "Analysis of dispersion characteristics of planar waveguides via multi-order interrogation of integrated Bragg gratings," *IEEE Photon. J.*, vol. 4, no. 2, pp. 310–316, Apr. 2012.

[21] H. L. Rogers, S. Ambran, C. Holmes, P. G. R. Smith, and J. C. Gates, "In situ loss measurement of direct UV-written waveguides using integrated Bragg gratings," *Opt. Lett.*, vol. 35, no. 17, pp. 2849–2851, 2010.

[22] H. L. Rogers, "Direct UV-written Bragg gratings for waveguide characterisation and advanced applications," PhD thesis, University of Southampton, Apr. 2013.

[23] I. Sparrow, G. Emmerson, C. Gawith, S. Watts, R. Williams, and P. Smith, "Assessment of waveguide thermal response by interrogation of UV written planar gratings," *IEEE Photon. Technol. Lett.*, vol. 17, no. 2, pp. 438–440, 2005.

[24] S. Baker, H. Rourke, V. Baker, and D. Goodchild, "Thermal decay of fiber Bragg gratings written in boron and germanium codoped silica fiber," *J. Lightw. Technol.*, vol. 15, no. 8, pp. 1470–1477, 1997.

[25] M. Svalgaard and M. Kristensen, "Directly uv written silica-on-silicon planar waveguides with low loss," *Electron. Lett.*, vol. 33, pp. 861–863, 1997.

[26] Y.-J. Rao, "In-fibre Bragg grating sensors," *Meas. Sci. Technol.*, vol. 8, no. 4, pp. 355–375, Apr. 1997.

[27] C. Holmes, J. C. Gates, L. G. Carpenter, H. L. Rogers, R. M. Parker, P. A. Cooper, F. R. M. Adikan, C. B. Gawith, P. G. Smith, and S. Chaotan, "Direct UV-written planar Bragg grating sensors," *Meas. Sci. Technol.*, vol. 26, no. 11, p. 112 001, 2015.

[28] S. W. James, R. P. Tatam, A. Twin, M. Morgan, and P. Noonan, "Strain response of fibre Bragg grating sensors at cryogenic temperatures," *Meas. Sci. Technol.*, vol. 13, no. 10, p. 1535, 2002.

[29] C. Sima, J. C. Gates, H. L. Rogers, P. L. Mennea, C. Holmes, M. N. Zervas, and P. G. R. Smith, "Phase controlled integrated interferometric single-sideband filter based on planar Bragg gratings implementing photonic Hilbert transform.," *Opt. Lett.*, vol. 38, no. 5, pp. 727–729, Mar. 2013.

[30] Rohm and Haas Electronic Materials, *Microposit s1800 series photoresists*, http://micromaterialstech.com/wp-content/dow_electronic_materials/datasheets/S1800_Photoresist.pdf, 2006.

[31] G. Harman, *Wire Bonding in Microelectronics*. McGraw Hill Professional, 2009.

[32] *Low-Shrink^{TM} OP-67-LS precision positioning optical adhesive*, TJA1043, Rev., Dymax, Apr. 2013.

[33] *Ultra Light-Weld®OP-4-20632 high T_g light path adhesive for fibre optic assembly*, TJA1043, Rev., Dymax, Mar. 2014.

[34] R. Tkach and A. Chraplyvy, "Regimes of feedback effects in 1.5-μm distributed feedback lasers," *J. Lightw. Technol.*, vol. 4, no. 11, pp. 1655–1661, 1986.

[35] C. E. Wieman and L. Hollberg, "Using diode lasers for atomic physics," *Rev. Sci. Instrum.*, vol. 62, no. 1, pp. 1–20, 1991.

[36] W. Lewoczko-Adamczyk, C. Pyrlik, J. Häger, S. Schwertfeger, A. Wicht, A. Peters, G. Erbert, and G. Tränkle, "Ultra-narrow linewidth DFB-laser with optical feedback from a monolithic confocal Fabry-Perot cavity," *Opt. Express*, vol. 23, no. 8, pp. 9705–9709, 2015.

- Chapter 4 -

1651 nm Planar Laser for Methane Sensing

4.1 Introduction

This chapter will describe a planar-waveguide based external-cavity diode-laser fabricated using the techniques described in Chapter 3. The laser is capable of continuously scanning and mapping the methane R4 quadruplet line at 1651 nm. The external cavity is a glass-on-silicon formed waveguide incorporating a Bragg grating as a frequency dependent reflector used to form the external part of the laser resonator. The external cavity utilises thermal micro-heaters that are deposited directly over the Bragg grating providing wider course tuning of the laser system. The grating and waveguide are inscribed into the chip using the UV-writing process. An external cavity diode laser can be fabricated to operate at any wavelength provided there is the availability of gain devices at the desired wavelengths, and availability of transparent, photosensitive glass that can be flame-hydrolysis deposition (FHD) deposited. Tuning is possible both finely through injection current tuning and coarsely by thermo-optically tuning using the micro-heaters. The concept of using heaters to tune a planar grating based laser device has has been outlined in patent [1] and reported in [2], both schemes used polymer based waveguides. To the author's knowledge no previous implementation has been demonstrated on glass waveguides. The details of the fabrication are provided in Chapter 3. All characterisation described in this chapter was undertaken by the author.

First, the general design considerations will be considered, followed by a discussion of various laser characteristics. Then a detailed description of how the relative intensity

noise (RIN) and phase noise measurements were taken, including experimental results are also included. This is followed by a demonstration of the laser system's capability for use in locking applications by implementing a frequency offset locking loop which is then used to characterise the heaters. Finally a discussion on preliminary methane spectroscopy results will be covered measuring methane gas concentrations between 250 ppm to 25 000 ppm.

4.2 System Overview

4.2.1 Geometry

Gain-chips are semiconductor laser diodes where usually one chip facet does not provide optical feed back usually through the use of an anti-reflection coating. For the laser systems described in this work an InP based gain-chip was used as the gain medium, whose centre wavelength is 1650 nm, available from Thorlabs. This centre wavelength makes the gain-chip especially suitable for methane gas spectroscopy. One facet has an anti-reflection coating and an angular exit to eliminate optical feedback. The other facet has a 90 % reflective coating. An additional advantage to using an angular exit is that it facilitates butt coupling, as any adjoining planar waveguide will require an angled facet to butt-couple in close proximity reducing parasitic back reflections from re-entering the waveguide. The butt coupling can be expected to be higher than 4 dB following the simulation and discussion in Section 3.2.3.1.

The second reflector of this laser resonator is formed by a Bragg grating written into a planar waveguide and is butt-coupled to the gain-chip, see Figure 4.1 using the processes described in Chapter 3. This waveguide uses a phosphogermanate core as it is known to provide more uniform layers that are important for accurate and repeatable writing of gratings at a particular wavelength. In addition this layer as described in Chapter 3 has been optimised to provide the smallest possible mode-field diameter to improve coupling to the gain-chip. This external reflector chip is attached to a V-groove assembly holding a standard telecommunications panda-type PM fibre that serves to couple out light using standard components. This is then followed by an attenuator and then an isolator. The attenuator has higher return losses than the isolator and provides additional isolation. The chip must be connected to the gain-chip at 17.7° to satisfy Snell's law as the light exits the gain-chip at 26.5° and the external cavity chip has an effective index of 1.45.

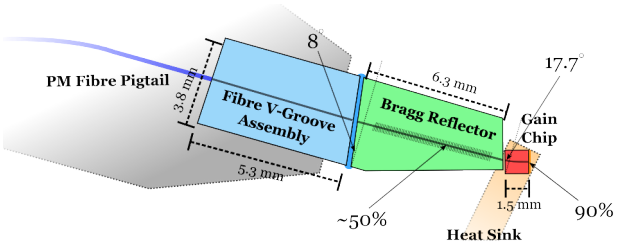

(a) Diagram showing the structure of the entire device along with approximate reflectivities of reflectors

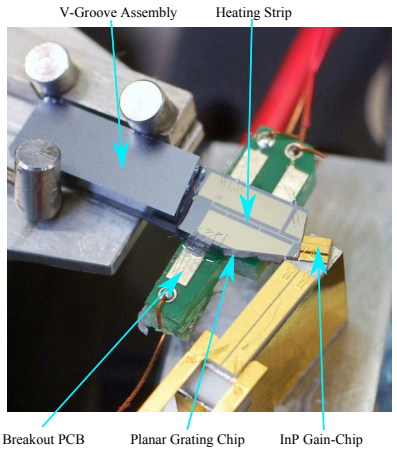

(b) Corresponding photo of one of the 1651 nm laser systems.

Figure 4.1: Diagram and photo of prototype system used in characterisation.

Measuring the coupling loss between the planar waveguide and gain chips was practically difficult and instead estimated using a simple elliptical Gaussian model. Elliptical Gaussians were used due as the exact mode structure was not known. From the angular divergence values of the output beam from the gain-chip specifications, an estimate of the near field elliptical Gaussian field could be determined. The most optimal design that could be produced using the FHD and UV-writing processes as discussed in Section 3.2.3.1 would produce an idealised coupling loss of ~1 dB. However layers produced in the FHD process usually diffuse between layers resulting in a larger mode than intended, in addition the surface roughness and alignment will be imperfect so the loss value will be >1 dB. The integrated optical fibre (IOF) chip has a considerably smaller mode-field diameter (MFD) compared to the planar waveguide improving the coupling between the external cavity and the gain chips resulting in a computed loss of approximately 1.2 dB. However the small MFD results in a higher coupling loss of 3.5 dB to the polarisation maintaining (PM) fibre pigtail though this loss is less critical compared to the intracavity loss of of the gain chip.

4.2.2 Grating Design

The spectral shape of an unchirped weak Bragg grating is approximately the Fourier transform of the apodisation profile of the grating. The apodisation profile refers to the strength of the fringe visibility of the written fringes. A uniform or unapodised grating has the strongest reflection as the fringe visibility is at full strength through the span of the grating. However the spectral shape of such a grating is a sinc-like profile and provides the narrowest spectral shape limiting the tuneability of the laser.

A Gaussian apodised grating leads to a Gaussian spectral shape and broadens the bandwidth of the Bragg grating reflection spectrum. Unfortunately the reflectivity drops significantly as much of the fringe visibility is reduced. A compromise between the strong, spectrally narrow uniform and weaker, spectrally broader Gaussian apodisation is the super-Gaussian. A super-Gaussian function of order n is defined as

$$f_{\mathrm{sg}}(x) \equiv \exp\left(-\left[\frac{x^2}{\sigma^2}\right]^n\right), \tag{4.1}$$

where σ is super-Gaussian width. A first order super-Gaussian is a regular Gaussian. The decision was made to use a super-Gaussian of order $n = 4$ as this resulted in a strong but broader grating where an unapodised grating or a Gaussian apodised grating would be too narrow or too weak respectively. A spectrally broader grating is necessary to cover the methane gas line suitably. This grating apodisation function would also result in a full-width at half-maximum (FWHM) bandwidth that was more comparable to the expected free spectral range (FSR) ensuring excellent side-mode suppression-ratio (SMSR) and good injection current tuning range.

The Bragg wavelength of the gratings is intentionally written at a lower wavelength than the methane gas line at 1650.96 nm as can be seen in Figure 4.2. This is to take advantage of the tuning capability of the micro-heater to precisely position the grating over the gas line. Since the gas line is spectrally broad (134 pm FWHM) the grating must be precisely positioned to resolve as much of the line as possible without mode-hopping. The lower wavelength confers another advantage that is to compensate for the Bragg wavelength shift induced from the deposition of the NiCr heater which shifts the spectral response of the grating to longer wavelengths, probably from a combination of induced stresses and interaction with the tail of the lateral mode field due to the thin (7 µm) overclad layer. The final measured reflectivity of the Bragg gratings for both devices was ~50 %.

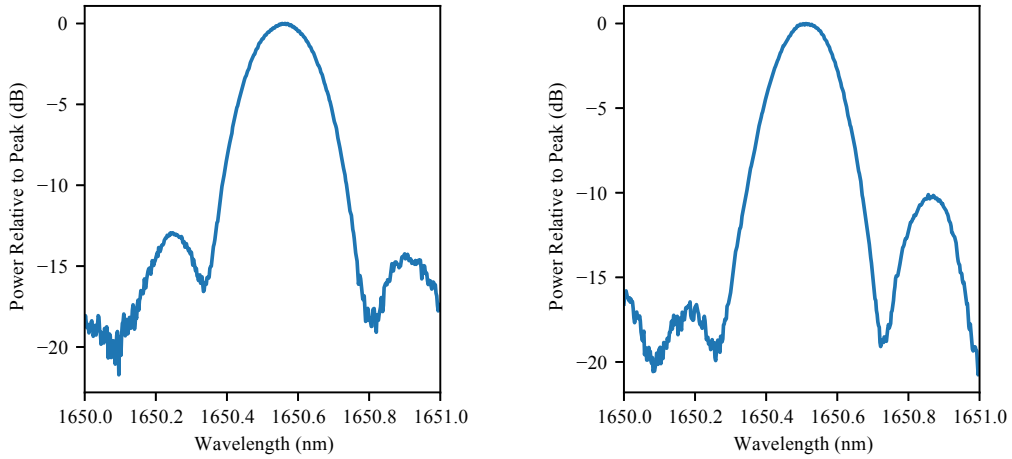

Figure 4.2: Reflectivity of gratings used to make both laser systems. Both gratings were written using the same recipe and went through the same process steps. The reflectivity is collected using an OSA and the gainchip as the ASE source for the measurement. The grating profiles have strengthened side lobes after the deposition of the thermal micro-heaters.

4.3 Laser Characterisation

The laser power characteristic with injection current is shown in Figure 4.3a, with a threshold at 140 mA. The evolution of the laser spectrum from threshold, as measured on an OSA, is shown as in Figure 4.3b. The wavelength shift is caused by an increase in the refractive index of the gain chip due to more injected carriers and changes of temperature. The inset plot demonstrates single mode operation with a side mode suppression ratio of >40 dB. Changes of injection current can achieve an SMSR of 55 dB. To the author's knowledge this SMSR is the highest achieved compared to values reported in the literature or quoted on commercial data sheets [3]–[6].

The laser power was measured at 20 °C, 25 °C, and 30 °C measured using a thermistor at the thermoelectric-cooler (TEC). For each temperature the laser system had to be realigned due to the thermal expansion of the heat sink between the TEC and the gain-chip. As the injection current is varied across the full range the laser hops 3 times as longitudinal modes are swept across the grating bandwidth and another longitudinal mode becomes more dominant.

The injection current tuning is shown in Figure 4.4. This measurement was taken by adjusting the current and measuring the central wavelength via the OSA. The current tuning demonstrates that it is possible to tune across the target gas line (>120 pm). The

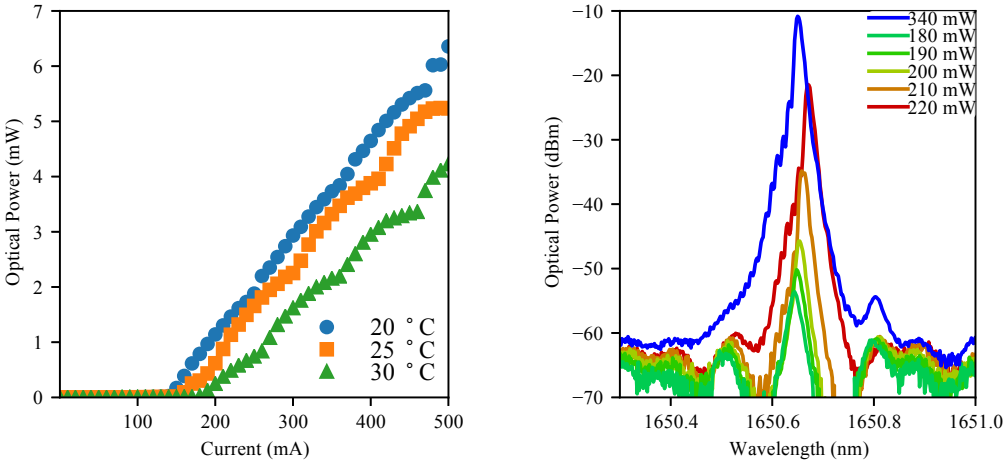

(a) Current-power displayed at various temperatures. The undulation seen in the output power is a result of mode hops whilst increasing the injection current.

(b) Spectra obtained using an OSA shows the evolution of laser spectrum as injection current is increased above threshold.

Figure 4.3

thermal heaters will be used to centre the grating over the gas line wavelength, which will maximise the mode-hop free spectral bandwidth the laser can scan.

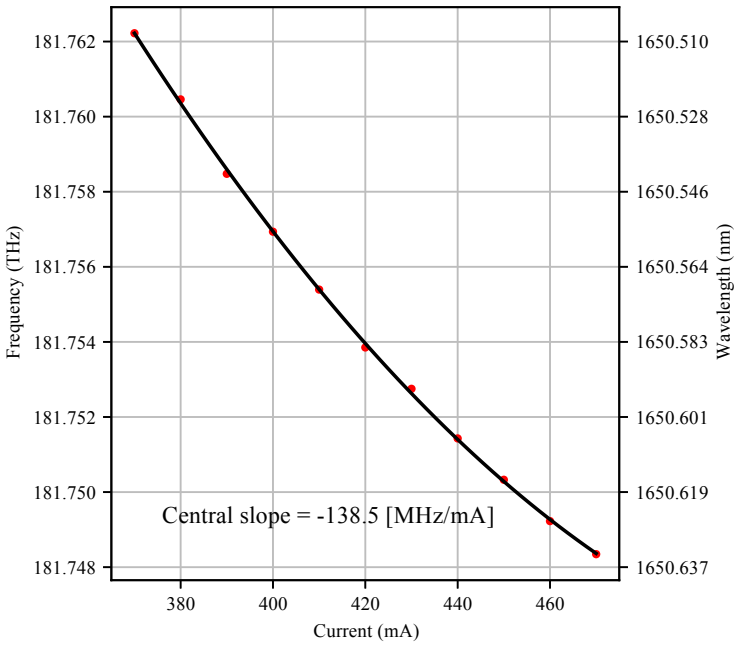

Figure 4.4: Plot shows the current tuning with wavelength and frequency. The plot is fitted using a second order polynomial. The displayed slope is the tangential slope measured at 420 mA, the midpoint of the curve approximately between two mode hops.

4.3.1 Laser Polarisation

Edge emitting diode lasers tend to be highly polarised devices due to having strong anisotropic geometry normal to the optical axis. Edge emitters often have strong Cartesian geometry, and in single mode devices, two polarisation modes with significantly different propagation constants. Vertical confinement is achieved by controlling the semiconductor layer refractive indices and usually results in strong confinement to give good overlap with the thin active region layer. Many edge emitting devices use a ridge structure to weakly guide light horizontally in the structure. As a result the mode field solutions result in a transverse-electric (TE) mode where the field is parallel with the horizontal axis, and the transverse-magnetic (TM) mode is perpendicular.

The mode that receives the lowest losses, will determine what mode the laser will lase on. There have been a number of mechanisms identified that contribute to diode laser polarisation preferences. Some polarisation dependent physical mechanisms are: propagation losses, Fresnel reflectivity, gain, stresses, and the confinement factor [7]–[11]. Interestingly, most of these mechanisms favour conditions for lasing action on a TE mode solution, which explains why most diode lasers are usually, but not necessarily, TE polarised. However without intricate knowledge of the gain-chips used

in this thesis it is difficult to offer a discussion for the dominant mechanism for the polarisation selection in this laser.

The laser external cavity is strongly birefringent due to the stronger confinement in the vertical direction. Through the same mechanism as PM fibre the mode should undergo minimal rotation as it propagates through the waveguide to the V-groove assembly. The V-groove assembly houses a PM fibre that couples out the light. The light collimated and transmitted in freespace through a polariser. Through manual rotation of the polariser the polarisation is TE and the isolation from TM is measured at ~25 dB. The polarisation is likely to be limited by the alignment tolerances between gain-chip to the external cavity and :to the PM fibre; these misalignments are likely to activate the orthogonal mode resulting in a slightly elliptical mode.

4.4 Noise Properties

This section will describe the noise properties of the laser with regards to relative intensity noise (RIN) and phase noise. These noise properties directly affect the suitability of the laser for various applications. In particular the RIN plays an important role in the tunable diode-laser spectroscopy (TDLS) technique used in this report.

4.5 Relative Intensity Noise

The RIN will affect the performance of the laser for measuring gas lines. Noise during scanning of a gas line can potentially conceal the characteristic dip that is used to infer the presence of the gas line. In the TDLS technique used in this thesis the laser wavelength will scan repeatedly over the gas line and the response measured on a photodiode. The intensity noise near the scanning frequencies and its harmonics will directly affect the system's performance.

Two measurement systems were used for this laser to cover different parts of the frequency spectrum. For lower frequency measurements (1 Hz to 1 kHz) a Thorlabs biased photodiode was used, followed by a transimpedance amplifier to convert the current signal into a voltage signal whilst maintaining high sensitivity and maintaining a good frequency response. For the higher frequencies (100 MHz), a fast amplified photodiode is used with a built-in transimpedance amplifier. The signal from this detector is amplified in a Minicircuits low noise amplifier and then fed into a 3 GHz

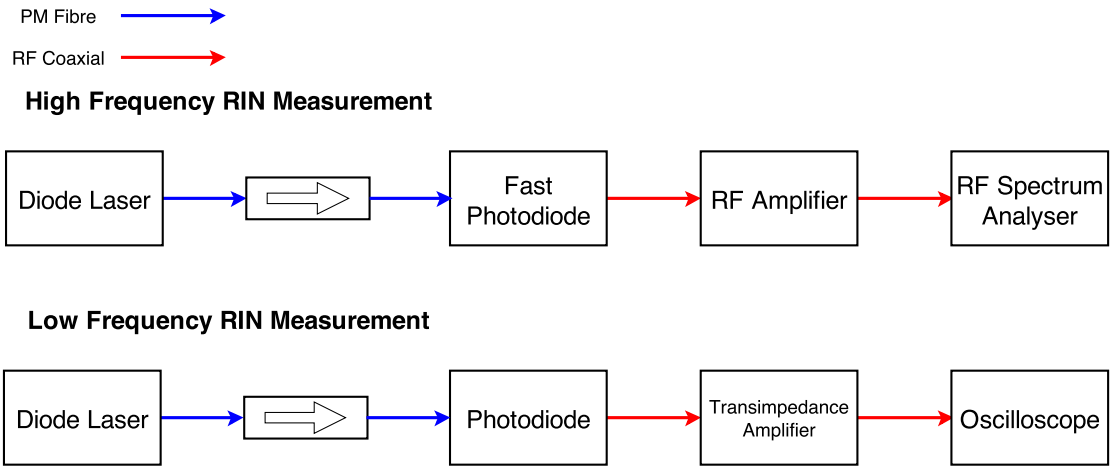

Figure 4.5: The system level diagrams of the two measurement systems used to measured the RIN. The RF amplifier prevented measurement under 100 MHz, and no significant noise was observed down to the low frequency limit of the RFSA. For lower frequencies, where likely TDLS modulation schemes will be used, a low frequency measurement system was used with custom built transimpedance amplifier.

radio-frequency Spectrum-Analyzer (RFSA). The measurement systems used are shown in Figure 4.5.

The higher frequency noise is limited by a noise floor that is close to the expected value of the associated shot noise limit. This is compared to a commercial Agilent external cavity diode laser (ECDL) based on a moving diffraction grating as seen in Figure 4.6b. The peak at ~200 MHz is caused by relaxation oscillations of the laser, the laser is then shot noise limited beyond this peak. The low frequency RIN can be seen in Figure 4.6a. The low frequency range was of most interest as this is where likely TDLS modulation schemes would occur. The low frequencies show a number of noise peaks corresponding to harmonics of mains electrical noise. Many of the other peaks seen are likely to be caused by acoustical standing wave modes excited by environmental noise, as peaks at a similar band of frequencies was suppressed in a similar system after being moved into a compact enclosure, discussed in Chapter 5.

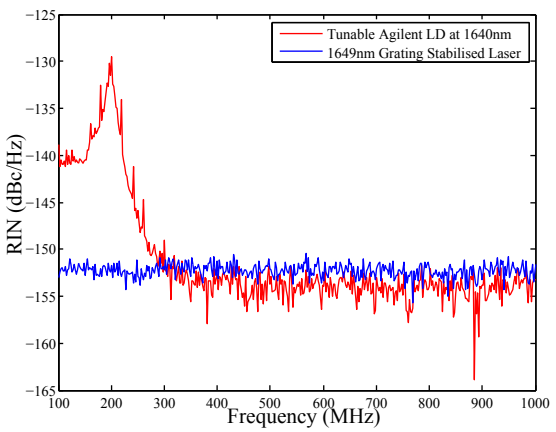

(a) Comparison between high frequency RIN of planar laser system and commercial Agilent ECDL taken on an RF spectrum analyser. Note the Agilent laser was emitting slightly more power at 1625 nm nearer to peak detector response leading to an effectively lower noise floor. The trace was taken over a period of 2 s and contains 461 data points.)

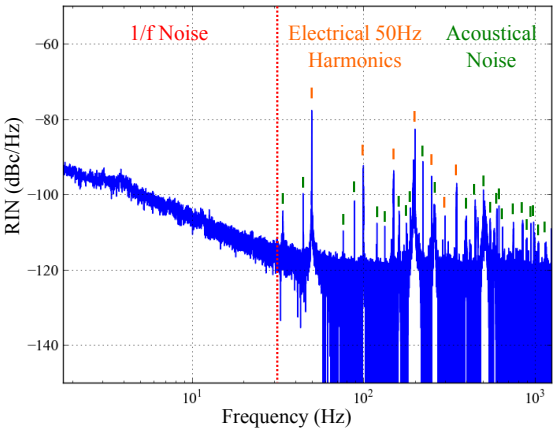

(b) Low frequency RIN after averaging the periodogram spectra of 20 long (23 s) oscilloscope traces. 50 Hz peaks and harmonics can be seen, in addition to acoustical modes.

Figure 4.6: Relative intensity noise traces for low and higher frequencies.

4.6 Phase noise and linewidth

Phase noise and linewidth measurements cannot be obtained directly from the photodiode as it is for a RIN measurement. Light incident on a photodiode converts photons to electrons and thus the derived signal from the photodiode is proportional to the incident optical power and not the field, and as a consequence any phase information is lost. This electrical response can be considered identical to a response that is equal to the incident field squared whilst dropping any high frequency terms. In the coherent detection configuration, the phase information can be inferred by mixing the signal of the device under test with an optical signal of known linewidth or phase noise. The square law response of the detector will produce a signal whose frequency and phase is the difference between frequencies and phases of the two signals, known as the beat note of the signals.

4.6.1 Measurement techniques

There are many measurement techniques used for determining the linewidth of a laser. An OSA could be used to measure the linewidth of a laser, however the best OSAs can only measure as low as 5 MHz [12], which is still broader than the linewidth of

most diode laser systems. The delayed self-heterodyne interferometer, heterodyne interferometer, optical phase locked loop (OPLL), and the frequency discriminator are far more precise techniques used to measure phase noise or linewidth properties of a laser [13].

In this section, arguably the most common technique, the delayed self-heterodyne interferometer will be discussed. This is followed by a discussion on the heterodyne interferometer which is the technique used in this thesis. Finally an account of the signal processing steps used to determine the phase noise in this thesis will be detailed.

4.6.1.1 Delayed Self-Heterodyne Interferometer

One of the most common and convenient methods for obtaining a linewidth measurement is to use a delayed self-heterodyne measurement. This technique splits the laser output into two. Where one signal is delayed, and the other frequency shifted before being combined again, so both are incident on a photodiode allowing the beat note at the frequency offset to be measured. The delay line is necessary and must delay the laser signal beyond its coherence length [14]. Where the coherence length is defined by $L_{\text{coh}} \equiv c\tau_{\text{coh}}$. The coherence time τ_{coh} is usually defined in the literature by

$$\tau_{\text{coh}} = \int_{-\infty}^{\infty} \left(\frac{R_E(\tau)}{R_E(0)} \right)^2 d\tau, \tag{4.2}$$

where R_E is the autocorrelation function of the laser optical field $E(t)$. The linewidth and coherence length are directly linked, using the definition of Equation 4.2, the linewidth $\delta\nu$ is expressed by τ_{coh} as

$$\delta\nu = \frac{1}{\pi\tau_{\text{coh}}} = \frac{c}{\pi L_{\text{coh}}}. \tag{4.3}$$

If the laser is not delayed sufficiently beyond $L_{\text{delay}} \gg L_{\text{coh}}$ it leads to calculation of an artificially narrow linewidth. For relatively low linewidth lasers this can make the measurement quite problematic as many kilometres of delay line may be needed. For example, a 10 kHz linewidth laser signal will have a coherence length of ~30 km which, for a valid measurement, may require much longer delay lines of optical fibre to be sufficient [15]. Even if measured at 1550 nm, where SMF-28 losses are low enough for a measurement, such lengths of fibre can be impractical in a lab, requiring many spliced, large bobbins of fibre. For many types of lasers, such as fibre-lasers and ECDLs, there

are other types of phase noise present beyond the $1/f^2$ that contributes to Lorentzian line shape. Other forms of $1/f$ noise contributions require even longer delay lines than would otherwise be needed [14].

An acoustic-optic modulator (AOM) is commonly employed in this measurement so that the beat signal is centred away from 0 Hz as the RIN is highest here and also for practical reasons as many RFSAs cannot measure near direct-current (DC).

4.6.1.2 Heterodyne Interferometer

Another common method of measuring linewidth is to use a heterodyne measurement. This technique typically uses a reference laser and a local oscillator (LO). Similar to the self heterodyne technique the LO and reference lasers are combined using a splitter. One splitter arm is then incident on a photodiode. This current is measured by suitable radio frequency (RF) equipment, often an RFSA. The field seen at the photodiode is

$$E(t) = E_1(t) + E_2(t) = E_1 \sin(2\pi f_1 t + \phi_1(t)) + E_2 \sin(2\pi f_2 t + \phi_2(t)), \tag{4.4}$$

where $E_1(t)$ and $E_2(t)$ are the laser fields generated by either lasers, $E_{i=1,2}$ is the mean respective laser's field and any intensity fluctuations are assumed to be negligible. f_i and ϕ_i are the laser's carrier frequency and phase fluctuation term. The photodiode generates a photo current that is proportional to the intensity of the total incident field electric field.

$$I(t) \propto (E_1(t) + E_2(t))^2 = \frac{1}{2}[{E_1}^2 + {E_2}^2 + E_1 E_2 \cos(2\pi(f_1 - f_2)t + \phi_1(t) - \phi_2(t))] + \text{hft.}, \tag{4.5}$$

where hft. refers to the remaining high frequency terms that are not considered as they cannot be detected by the photodiode. The beat note frequency is the difference of the two waveforms and the phase noise is characterised by the group $\phi_1(t) - \phi_2(t)$. As $\phi_1(t)$ and $\phi_2(t)$ represent the Gaussian distributed random phase walks with a mean of zero, the terms can be considered the sum of the two noise distributions.

As the line shape is directly linked to the phase walk terms, measuring the linewidth of the beat note on an RFSA generally results in a measurement that is the sum of the two linewidths. For example if the two lasers are beat together with Lorentzian line shapes of 12 kHz and 20 kHz the measured beat note Lorentzian linewidth would be

32 kHz. This leads to two common methods of determining the linewidth of a laser using a heterodyne interferometer. The first method uses a reference laser of known linewidth or a linewidth known to be significantly narrower than the LO. However for measurements of a narrow linewidth LO like this may not be practical. Alternatively the LO and reference can be identical laser systems. In this situation the measured linewidth is assumed to be double that of the individual lasers [16]. The main disadvantage to this measurement technique is the requirements for an additional well matched laser system to exist. However this method scales to lasers of arbitrarily narrow linewidths, it does not require much lab space as there is no need for lengthy delay lines. When using an identical laser this technique then does not require a narrow linewidth reference laser that can be very difficult to characterise or obtain.

4.6.2 Obtaining Phase Noise from Beat Note

The use of linewidth as a measure of the phase noise gives quite limited information. It is not uncommon to have linewidths quoted in product specifications without indicating the experimental procedure, measurement time, and the delay line length used in the case of a self-heterodyne measurement. Measuring linewidths over longer periods of time has a tendency to generate a broader line shape; the line can be thought to be "drifting" significantly with time. This highlights the importance of quoting measurement times (or delay line lengths) when producing a linewidth value.

The typical method for measuring the intensity power spectral density (PSD) of the beat note typically produces an overestimation of the intrinsic linewidth due to drift of laser line with time as discussed in Section 2.4.3.4. As a consequence, using a laser intensity PSD is not an accurate predictor of performance in coherent communication systems. A more useful predictor in optical systems, where phase performance is important, is to produce a phase or frequency noise PSD. It is a far more general indicator of performance to specific systems where laser coherence is a critical performance parameter, especially when considering phase modulation and coherent detection performance. The phase noise PSD of a laser can then be used to derive other commonly used frequency stability metrics such as the linewidth and Allan deviation metrics. Unfortunately measuring the phase noise PSD can require more stringent configurations. Frequency discriminators and an OPLL are a couple of methods that can provide a direct means of measurement [13]. However it has been shown that the measurement can be determined from beat note signals using a fast Fourier-transform (FFT) based on a vector network analyzer (VNA) [17]. This section will outline an alternative method that utilises an oscilloscope measurement of a beat-note to obtain the phase noise PSD,

to the author's knowledge the using an oscilloscope and post processing in this manner to determine linewidth and phase noise is novel and was developed by the author.

A beat note signal generated by a heterodyne interferometer, that is digitally acquired using a suitable oscilloscope, can be used to compute the phase noise PSD through a series of signal processing steps. When measured on an oscilloscope, the difference frequency of the lasers is likely to be many MHz or GHz and may be difficult to capture near zero, due to drift, where the sampling rate is slowest. This obtains the longest possible measurement where oscilloscope memory depth is limited. A longer measurement time expands the PSD frequency range into lower frequencies. The beat note from a sampling perspective can be considered a carrier wave that is modulated and has a finite bandwidth. Rather than oversampling at a frequency well above twice the carrier frequency, the signal can instead be undersampled at twice the bandwidth of the signal. This type of undersampling is known as intermediate frequency (IF) sampling in the communications field [18]. The only information lost is the redundant centre frequency, which is only the difference between the lasers and contributes no useful information to phase noise PSD computation. This method allows for a simpler experimental setup when compared to a heterodyne frequency down conversion. Additionally only the insignificant phase noise of the oscilloscope's sampling clock is added to the phase noise of the signal, resulting in a more accurate measurement of the signal.

The sampling rate F_s will divide the measurement bandwidth into Nyquist zones that are $F_s/2$ wide. It is important to select the F_s such that the signal bandwidth is captured within a particular zone. The signal will then be aliased to the first Nyquist zone between 0 and $F_s/2$. However all the noise present in the measurement bandwidth will also be aliased to the first Nyquist zone, decreasing the signal-to-noise ratio (SNR). Figure 4.7 illustrates the effects of undersampling.

When measuring the beat note of a single frequency laser the background noise is likely be low compared to the beat note signal power even after aliasing. A higher noise floor will increase the measured phase noise power however in practice there should be sufficient SNR as the original background noise will likely be very small. An accurately recorded beat note signal is assumed to be in the form

$$v(t) = V(t)\cos(2\pi f_{\text{bn}} t + \Delta\phi(t)), \tag{4.6}$$

where $V(t)$ and $\phi(t)$ represents the instantaneous amplitude and phase walk with time t, f_{bn} represents the beat note frequency and the phase fluctuations

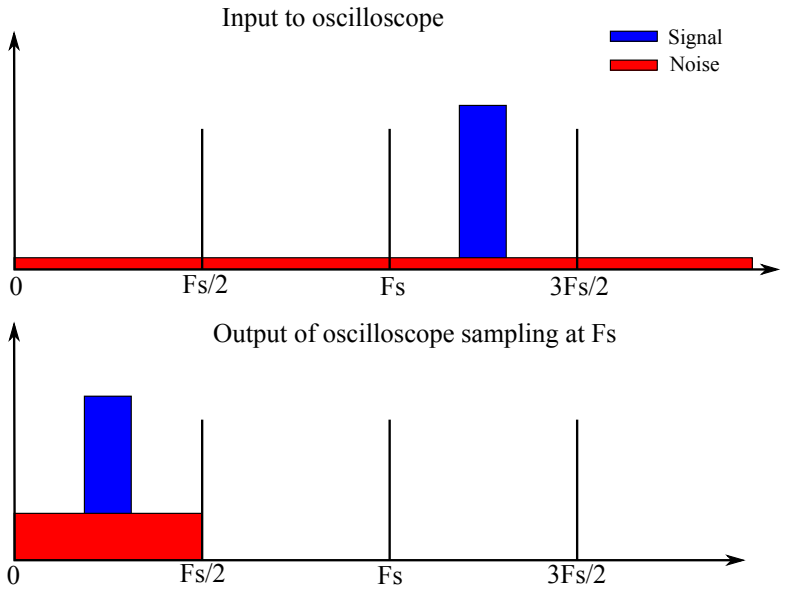

Figure 4.7: Plot demonstrating the effects of spectral content as seen by the oscilloscope when IF sampling a signal. Undersampling the total spectrum that is bandlimited to $2 \times F_s$ with a sampling rate of F_s divides the oscilloscope bandwidth into Nyquist zones of width F_s. All frequency content of higher Nyquist zones are aliased down into the first Nyquist zone. The signal is denoted in blue, and the noise power denoted as red. The measurement noise power density has compounded by 4 times.

$$\Delta\phi(t) \equiv \phi_1(t) - \phi_2(t). \tag{4.7}$$

The beat note average frequency f_{bn} is an arbitrary frequency as a consequence of undersampling and confers no information to the phase noise. The real representation of the signal does not allow convenient access of the phase term $\Delta\phi(t)$. A more useful representation is the complex analytic signal associated with $v(t)$ defined as

$$v_a(t) = v(t) + i\mathcal{H}v(t), \tag{4.8}$$

where $\mathcal{H}$ is the Hilbert transform operator. The Hilbert transform is obtained by deleting the negative frequency components of the sample signal. An equivalent representation of the analytic signal Equation 4.8 is its phasor representation [19]

$$v_a(t) = V(t)e^{i[2\pi f_{\text{bn}}t + \Delta\phi(t)]}. \tag{4.9}$$

As the complex argument contains the phase information it can be computed simply. First the high frequency carrier is removed. There are number of simple algorithmic

signal processing techniques for determining average frequency f_{bn} that will not be discussed further. To eliminate the high frequency term the analytic is multiplied by the the complex exponential $e^{-i2\pi f_{\text{bn}}t}$

$$v_a(t)e^{-i2\pi f_{\text{bn}}t} = e^{-i2\pi f_{\text{bn}}t}V(t)e^{i[2\pi f_{\text{bn}}t+\Delta\phi(t)]} = V(t)e^{i\Delta\phi(t)}. \tag{4.10}$$

The argument $\Delta\phi(t)$ can be easily determined due to the polar representation of the signal leading to a phase value that falls between $(-\pi,\pi]$. This phase value is unwrapped by compensating for 2π phase jumps, which is only reliable when the phase fluctuations occur significantly less than 2π. This leaves us with a random phase walk term $\Delta\phi(t)$.

In this thesis the spectrum $R_{\Delta\phi}$ is estimated using Welch's method, a method for estimating the PSD of a time sampled signal. This provides a more useful estimation than simply computing the FFT of the entire signal. This method divides the signal into overlapping segments that overlap by 50%. An FFT is computed on each segment, and each frequency bin is then averaged over all of the segments. The validity of this method will not be detailed further in this thesis and the author recommends [20] for further reading.

This method provides a way of deriving the phase noise from a time trace of the beat note signal using only a high sampling rate oscilloscope. This measurement method provides greater flexibility and convenience compared to designing an OPLL or building a sensitive enough interferometer to measure the phase noise.

4.6.3 Phase Noise Measurement

For this laser system, the decision was made not to use a self-heterodyne measurement. In part, due to the difficulty of obtaining optical components at 1650 nm and also the lengthy delay required would add significant loss to the signal. Instead a second well matched laser was constructed. This laser system used the same translation stages, gain-chip model, and the waveguides came from the same wafer and was processed using the same procedures; because of this it is assumed that they will share similar noise properties. Beating the two lasers together provides a beat note and this beat-note is analysed to produce a conventional intensity plot of the laser. In addition a phase noise PSD is produced utilising the technique described in the previous section. The measurement setup used to obtain the time traces of the beat note is shown in Figure 4.8.

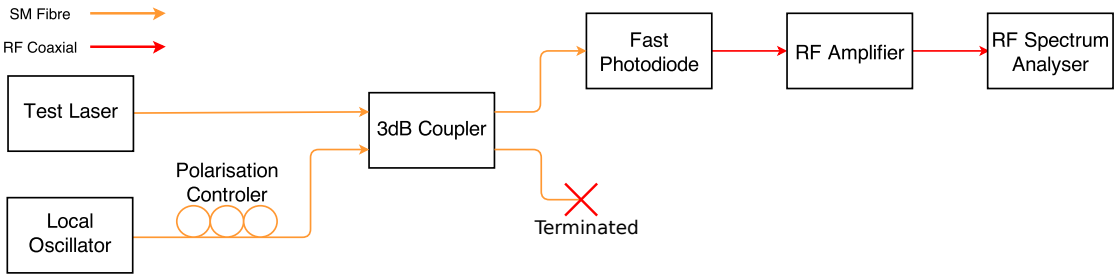

Figure 4.8: System level diagram showing the setup used to make the beat-note measurements in this work. The two lasers are well matched and operate at similar wavelengths such that the wavelength difference is <3 GHz to be measurable on the oscilloscope. These beat note traces are post processed in order to derive plots of the spectral line and also the phase noise.

The intensity spectrum of the line is obtained by computing the discrete Fourier transform (DFT) of the laser line using Welch's method, and a Lorentz profile is fitted to the spectral data. To avoid overestimating the Lorentzian linewidth of the beat signal, only a short time length of the beat-note is used (120 µs), reducing the error from drift in the signal. The measurement time cannot be made arbitrarily short as the DFT windowing function will broaden. The beat-note and the Voigt fit of the PSD can be seen in Figure 4.9. The Voigt fit indicated a Lorentzian linewidth of ~414 kHz for each individual laser, this value will be an overestimation and only indicates an upper limit of the linewidth as drift will always be present in any direct measurement of the linewidth from the intensity PSD.

As previously discussed, measurement of the phase noise provides an alternative method for evaluating the frequency stability properties of oscillators. The phase noise is time independent and can give an accurate measurement of the underlying laser Lorentz linewidth without it being obfuscated by longer time scale drift instabilities.

The computed phase noise from the time trace is given in Figure 4.10. The phase noise model given in Equation 2.71 is used to accurately determine the intrinsic linewidth [13], [17]. The noise model fit indicated by intrinsic Lorentz linewidth of ~220 kHz for each laser. This measurement indicates a lower linewidth than obtained directly from the FFT, but within reasonable agreement. To the author's knowledge this is the narrowest Lorentz linewidth achieved at 1651 nm. Most other laser systems are in MHz range with the lowest quoted linewidths found in commercial single frequency diode lasers with linewidths in the region of 1–5 MHz [5], [6].

A linewidth of ~220 kHz is a narrower linewidth than would be achieved in most monolithic diode laser systems however it is broader than expected. High intracavity losses caused by the coupling between the waveguide and the gain-chip could contribute

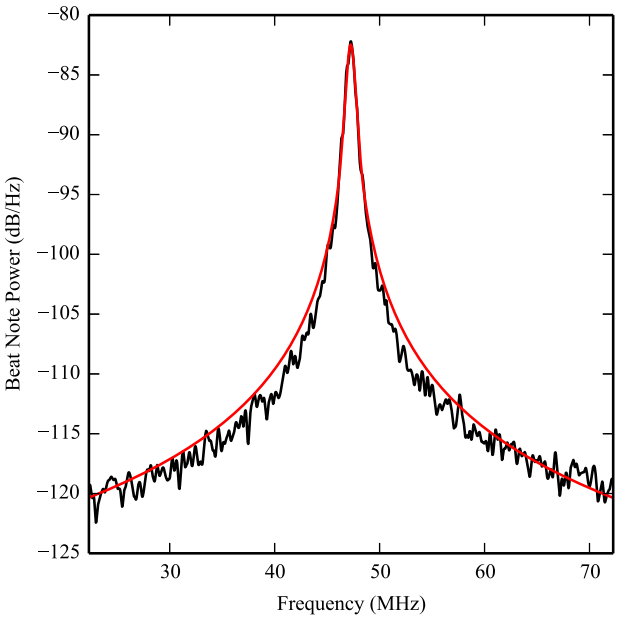

Figure 4.9: Black shows the resulting beat-note spectrum after applying the FFT to the beat-note signal derived by heterodyning the lasers emissions. Red shows the Voigt fit in where the Lorentz FWHM is ~828 kHz FWHM, the individual linewidths will be approximately half of this value.

significantly the broader linewidths as this reduces the round trip lifetime of photons in the cavity. If the heaters are indeed interacting with the optical field this could also introduce a significant losses into the cavity.

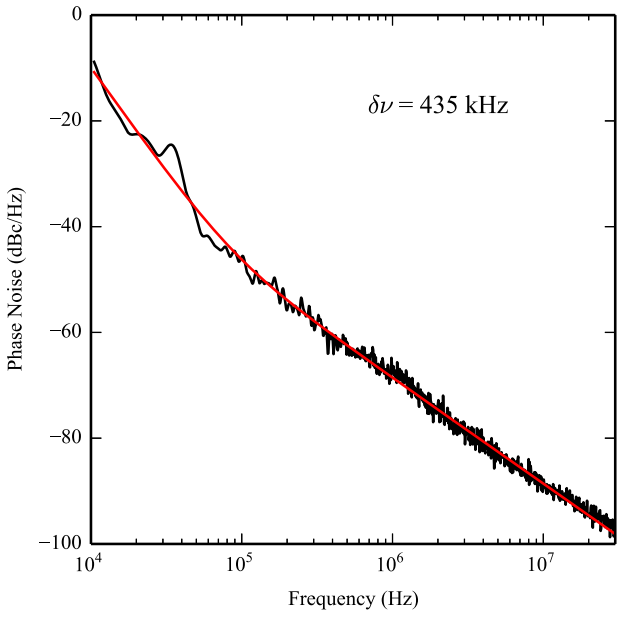

Figure 4.10: Black line shows the phase noise measurement calculated from the beat-note measured on an RF-oscilloscope. The red line shows fitted model as described by [13] with fitted Lorentz linewidth parameter $\delta\nu$ = 435 kHz. The phase noise was measured over a period of 2.1 ms.

4.7 OPLL Stabilisation

The phase locked loop (PLL) is an extremely successful electronic control loop system used for locking a voltage controlled oscillator (VCO) frequency to a reference frequency. The loops are so successful its use is ubiquitous, often used for example for clock recovery, demodulation and frequency synthesis. Frequency synthesis refers to the generation of a rational multiple of the reference signal. This is commonly used when generating an accurate oscillator signal based off a precision reference signal such as a quartz oscillator.

Consider the case of using a heterodyne configuration discussed shown in Figure 4.8, current tuning a laser changes the index of the gain-chip, changing the cavity length of the laser, and as a consequence changing the operating laser frequency. This can be thought of as a type of VCO and like a conventional VCO, the beat signal of two beating lasers can be locked to a frequency reference. This has the effect of the locking the frequency difference such that the slave laser follows the frequency of the master laser with a fixed frequency offset and is known as frequency offset locking or an OPLL [13], [21], [22]. These loops have applications in Brillouin sensing [23] and atomic physics [24].

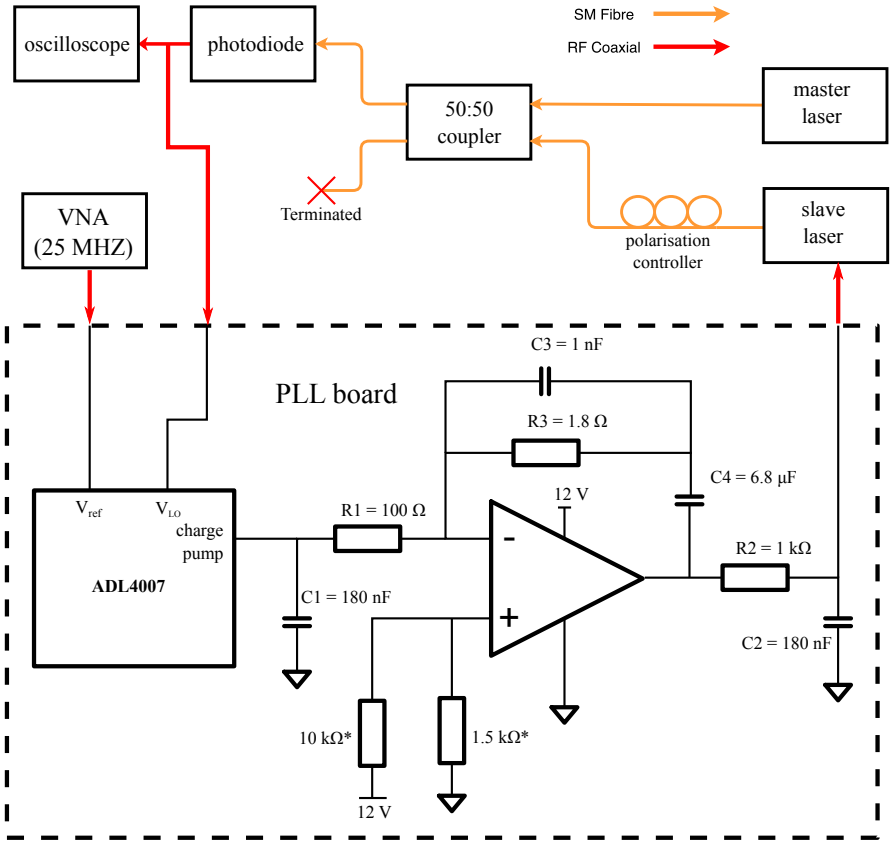

Figure 4.11: Overview of the OPLL locking system. The dashed box gives a simplified circuit diagram of the evaluation board containing the ADF4007, with the full circuit of the loop filter given. Component values R1, R2, R3, C1, C2, C3 and C4 had to be designed to the application. Component values marked by * were preinstalled and are used to bias the opamp filter, which maintains a positive output. The VNA acted as tuneable reference oscillator that was set to output 25 MHz. The ADL4007 was configured to phase lock to 32 times the frequency of the reference.

In this thesis the capability of these waveguide based lasers to lock using injection current locking is demonstrated. This locking scheme is used in Section 4.8 to measure the thermal heater frequency response. A system overview of the locking system can be seen in Figure 4.11. The OPLL configuration described here uses a commercial ADF4007 PLL frequency synthesizer prepared on an evaluation board from Anolog Devices. The RF reference is generated from a VNA operating at 25 MHz. The generated beat note from the lasers which will be referred to as the VCO signal. The PLL synthesiser divides down the reference signal by an integer value, and a separate frequency divider also divides the VCO signal before the phase frequency detector (PFD). The PFD is typically limited by the frequency it can operate at, hence the need for a divider. The divider also serves a second purpose as it is essential for frequency synthesis. Manipulating how the VCO and reference signals are divided will determine the frequency relationship

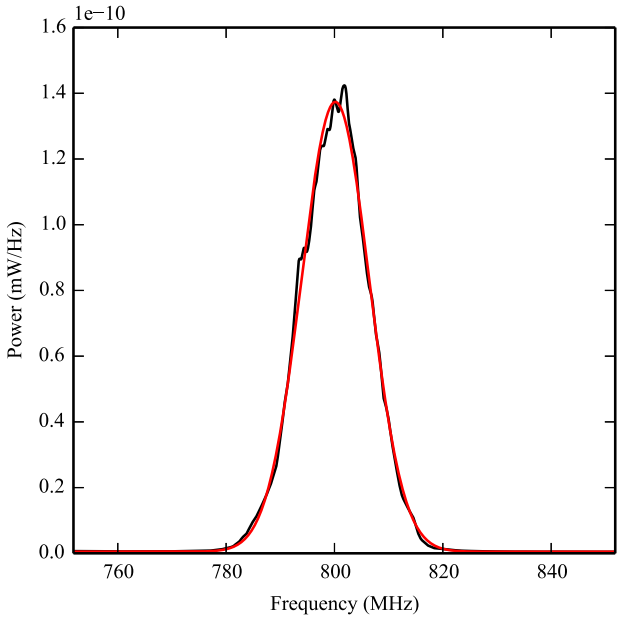

Figure 4.12: The computed beat-note PSD after frequency offset locking at 800 MHz. The measurement was taken over 2 ms. The red line shows the Gaussian fitting with a FWHM of 10.5 MHz.

between both signals. The PFD compares the two signals, and determines whether VCO signal is lower, higher or equal to the reference frequency and generates a discrete positive, neutral, or negative pulse width modulation (PWM) signal. To derive a suitable continuous phase error signal for the VCO the PWM signal must be integrated. A charge pump converts the PWM voltage signal to a current signal that makes the loop filter design simpler, for example a capacitor would integrate a current signal and produce a voltage signal. Most PLL synthesiser chips incorporate the frequency dividers, PFD and charge pump, leaving the loop filter design for the engineer to design to the requirements of their system.

The evaluation board contains a skeleton circuit for an active loop filter providing spaces for resistors R1, R2, R3 and capacitors C1, C2, C3 and C4 to be soldered as seen in Figure 4.11). Analog Devices provides a software PLL design tool that was used to determine reasonable resistor and capacitor values for the loop filter. The PLL is set up to divide the 25 MHz reference signal by 2 and divide the VCO signal by 64 effectively multiplying the signal to 800 MHz. The loop filter circuit is shown in Figure 4.11.

The PSD of the beat-note can be seen in Figure 4.12, this measurement was taken over 2 ms; the beat-note was not observed to broaden over longer time periods (>1 h) and will likely be limited to the frequency stability of the VNA that is used to generate the reference.

4.8 Characterisation of Thermal Heaters

Using the heaters in combination with injection current tuning, mode-hop free frequency tuning of up to 28 GHz can be performed. Figure 4.13 shows the laser wavelength with tuning. Failure is usually observed at heater powers >5 W that would correspond to an approximate Bragg wavelength shift of ~4 nm. Although the temperature sensitivity of Bragg gratings written in FHD deposited phosphogermanate glass is unknown if we assume the value is approximately the same as silica the maximum wavelength shift corresponds to heating of the core to >300 °C.

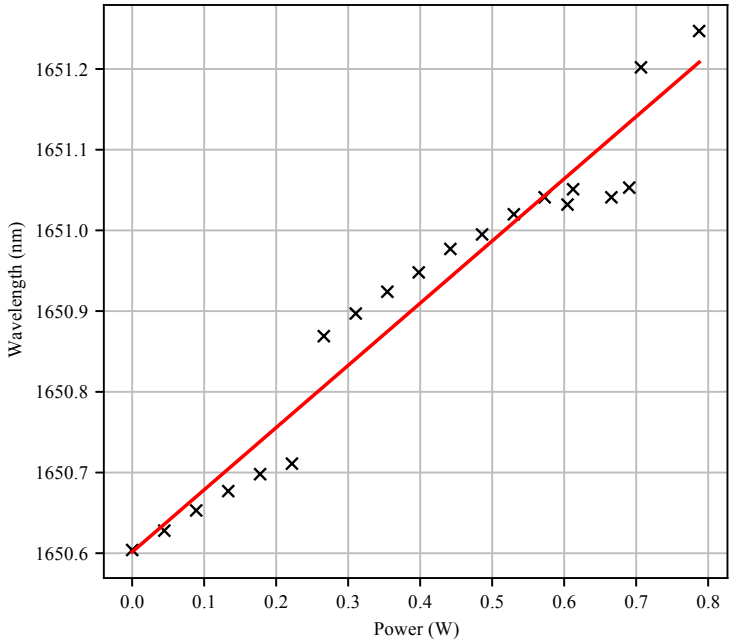

Figure 4.13: Plot showing change of laser wavelength as heater power is increased. Note there are two jumps at 1650.79 nm and 1651.13 nm as a result of a mode hop. The slope of the line is 770 pm W^{-1}.

To evaluate the frequency response of the heaters for wavelength-tuning, the lasers are put into an OPLL configuration as described in Section 4.7. The response can be measured from the tuning signal generated from the integrating filter used to modulate the injection current to the laser. The heaters were sine wave modulated with a DC value due to the square-law response of the heaters to the signal using a function generator. The subsequent signal was recorded using lock-in detection. The frequency response is shown in Figure 4.14 with a 1.5 kHz cut-off (at 3 dB point). This is higher than the predicted cut off from the approximated COMSOL model discussed in Section 3.5.1. This mismatch is likely from approximations made in the COMSOL model such as heat loss mechanisms and accuracy of layer thicknesses and thermal responses. Using

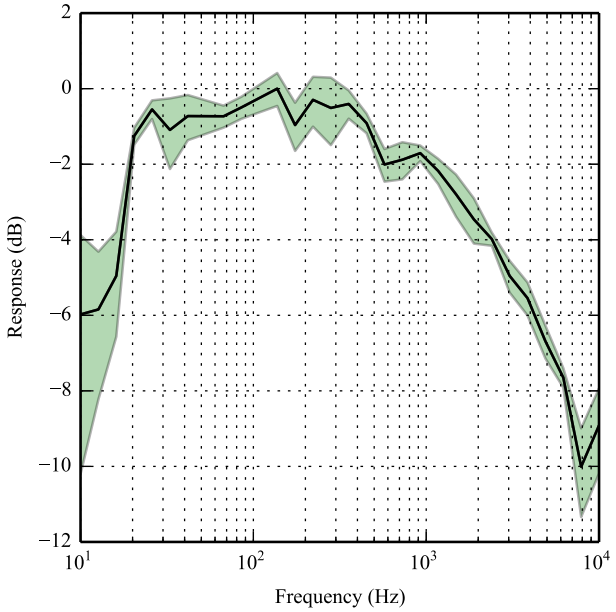

Figure 4.14: Frequency response of the heaters; the 3 dB point is 1.5 kHz. The shaded areas above or below represents 1 standard deviation. 0 dB is maximal frequency tuning.

heaters to modulate the wavelength results in >6 dB isolation from intensity fluctuations compared to modulation of the injection current. The weaker signal near DC is due to distortion of the signal, transferring energy into higher harmonics hindering lock-in detection.

4.9 Methane Spectroscopy

To demonstrate the suitability of this laser for applications in spectroscopy. The laser was transported to Cranfield University. Here I worked with another PhD based in Cranfield University student to scan various concentrations of methane gas in synthetic air.

The test methane gas mixture was produced by combining the two cylinders whose mixtures were 2.5 % methane (CH_4) in synthetic air, and the other cylinder is pure synthetic air, where synthetic air is 80 % N_2 and 20 % O_2. Combining the gases this way was done for safety reasons so that leakages would not deplete room oxygen and methane concentrations were always kept below the lower explosive limit. The mixtures were combined to various concentrations using two mass flow controllers (MFCs) into a gas cell that is 25 cm long with Brewster windows. A schematic of the system can be seen in Figure 4.15.

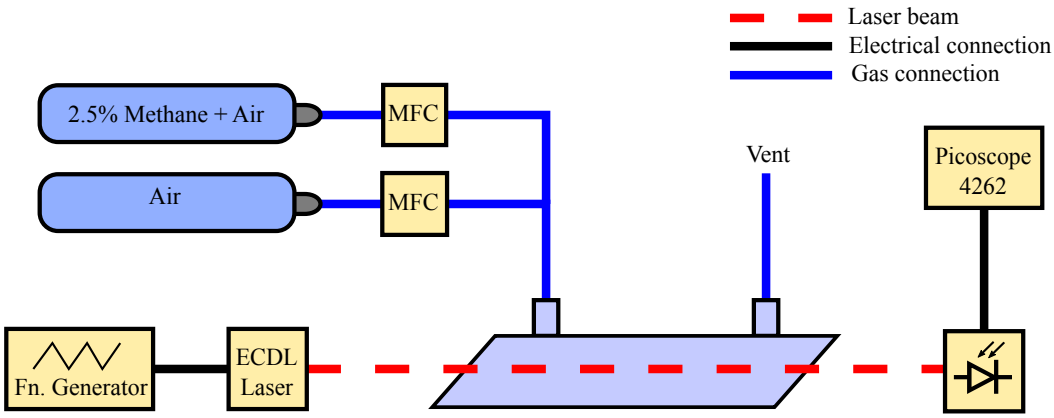

Figure 4.15: System overview diagram of the ECDL system for measurement of the methane R4 gas line. An 80 Hz triangle wave injection current was used to modulate the system. A Pioscope 4262 16-bit oscilloscope was used to sample the resulting waveform detected from the biased InGaAs photodiode. Not to scale.

The Beer-Lambert law, describes the attenuation of an optical signal as it propagates through an absorbing medium. The law gives attenuation the light $\mathcal{P}$in going into a gas by the relationship

$$\frac{\mathcal{P}\text{out}}{\mathcal{P}\text{in}} = e^{-\alpha L}, \tag{4.11}$$

where $\mathcal{P}$out is the attenuated light intensity, α is the coefficient of absorption, and L is the interaction length.

This detection system was used to scan methane at concentrations of 25 000 ppm, 12 500 ppm, 5000 ppm, 2500 ppm, 125 ppm, 500 ppm, and 250 ppm. Before each scan was taken, the gas cell was vented with pure synthetic air for several minutes and a calibration trace taken, then a new gas mixture was added and allowed another several minutes before a new scan taken. The gases were scanned by injection current tuning using a triangular waveform at 80 Hz from a function generator. A triangular waveform was used instead of a saw-tooth wave as the discontinuity resulted in an unstable laser output. The recorded calibration trace is removed from the scan trace as a form of common mode rejection of the modulation effects, revealing the dip associated with the absorption line. This is averaged over the total number of triangle wave periods taken for 5 µs duration of the scan. To obtain the x and y axis scales a Voigt profile is fitted to the 25 000 ppm trace and then scaled based on simulation values derived from the HITRAN database[25]. The fitted scan can be seen in Figure 4.16.

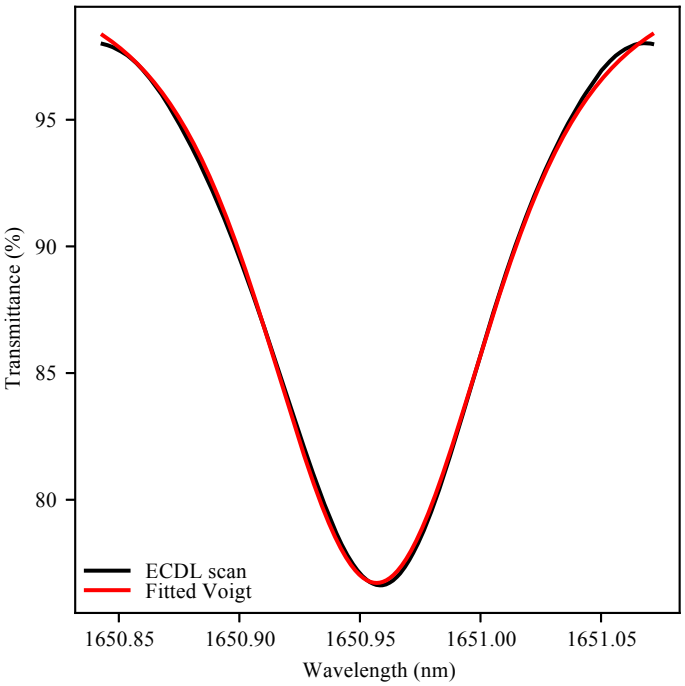

Figure 4.16: Example of detected methane absorption line at concentration of 25 000 ppm. A Voigt profile is fitted to the scan and used to infer transmittance and x-axis scale.

The laser was able to identify down to a concentration of about 1250 ppm as can be seen by the detected absorptions in Figure 4.17. A number of factors prevented measurement lower than this concentration. Weak Fabry-Pérot fringes prevented measurement at lower concentrations from unintended reflections within the optical setup that became strong at low concentrations. As the laser is on stage systems there is significant drift between calibration and gas measurements. The wavelength dependence on output coupling from the Bragg grating made any drift have a significant impact on common mode rejection between the calibration and measurement traces. Sensing down to this level would make the system suitable for locating gas leaks and determining lower explosion limit of leaks [26], [27]. Other single frequency diode laser systems operating at nearby methane gas lines can detect down to 1–50 ppm [28]–[30].

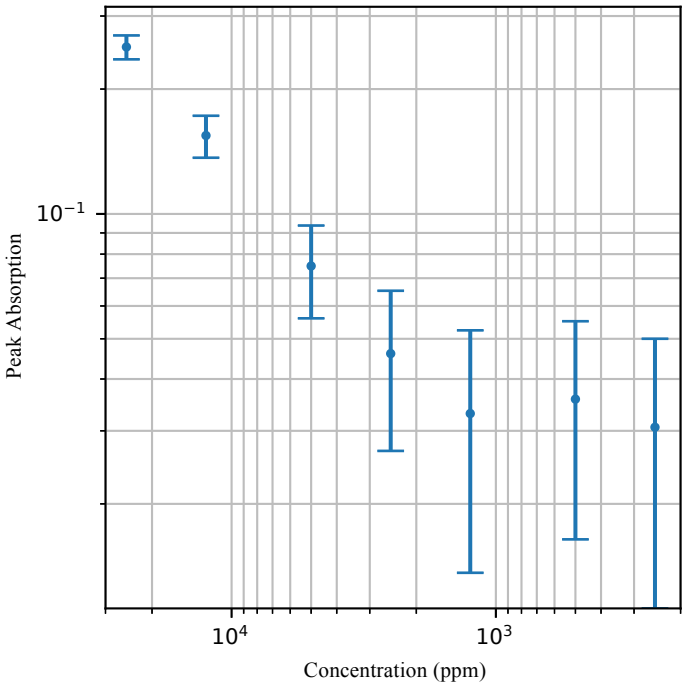

Figure 4.17: Inferred absorptions of the various methane gas concentrations. The trend should continue down linearly, but hits a floor at concentrations higher than 1250 ppm due to limitations in the measurement configuration.

4.10 Towards improving methane detection limits

Though the noise parameters of the laser were satisfactory for methane detection. The system failed to detect below 1250 ppm typical of ECDL based lasers. There are spectroscopic experiment improvements and also improvements to the laser design that can be made. A simple experimental design improvement that should significantly improvement the experimental sensitivity to lower concentrations would be to use two photodetectors, ideally balanced photodetectors. This would offer true common mode rejection between the optical signals rather than removing the calibration trace from the methane detection trace in post processing where time between the collection of the traces allows the laser response to drift.

Packaging of the laser would go a long way to eliminating drift as a result of the environmental changes of conditions particularly temperature. As the stage systems are largely metallic with significant thermal coefficients of thermal expansion (1 µm $°C^{-1}$), exaggerated further as two separate mounts are used to hold the gain-chip and the external cavity chip, leading to significant drift during the experiment. Sweeping the current using a triangle wave, revealed significant nonlinearity in the relationship of the injection current output coupled optical power and was highly dependent on

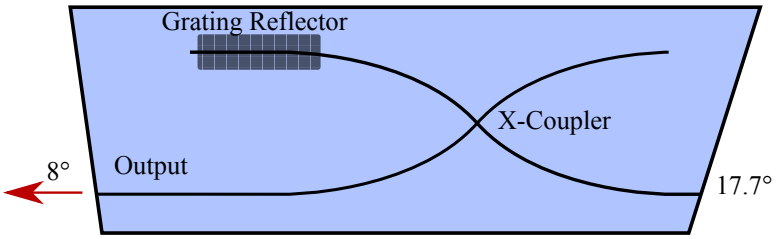

Figure 4.18: Conceptual diagram of an external cavity utilising an X-coupler as a means of output coupling optical power from the device. The X-coupler coupling ratio can be chosen to arbitrary values. Waveguides that finish within the chip are self terminating and have negligible back reflections.

the alignment conditions of the system. As a result thermal drift would result in the significant changes in the response. This nonlinear relationship is a result of coupling power out of the Bragg grating reflector end as this has a highly wavelength dependent response.

To reduce this effect the thermal tuning of the Bragg grating could also be modulated such that the grating shift is matched to the shift associated with the injection providing a constant output coupling ratio. It has been demonstrated that the ECDL system can modulate the thermal heaters at <1.5 kHz. This also would extend the range of wavelengths that the laser can be modulated over without mode hopping as the active longitudinal mode would not roll off the the bandwidth of the Bragg grating reflector.

Another design improvement that can be made would be to incorporate an X-coupler into the resonator of the external cavity before the Bragg grating reflector [31]. Figure 4.18 shows conceptually how this could work. X-couplers provide a means of coupling two UV-written waveguides and their coupling ratio is highly insensitive to wavelength. Output coupling the laser power in this fashion would increase the linearity of the injection current to optical power response of the laser improving the laser's ability to detect lower concentrations of the methane.

4.11 Conclusions

Two single frequency laser systems, with an SMSR of >55 dB, at 1651 nm have been demonstrated. The systems have demonstrated coarse wavelength tuneability via a deposited NiCr heating assembly. The heating element could successfully tune the laser over the 1650.96 nm methane line and demonstrated high modulation speeds of up to 1.5 kHz. Though a similar tunable laser system has been built using a polymer

waveguide at C telecommunications band, little information is provided on noise properties. The polymer based system has smaller SMSR of ~ 40dB and lower output power (< 1mW) [2]. Measurement of the RIN showed suitability for low noise applications, at higher frequencies >100 MHz the signal was limited by the noise floor of the system. The laser was made to beat with an identically built system to obtain that phase noise, resolving a linewidth of 218 kHz, also demonstrating a new method of determining the phase noise using an oscilloscope. The RIN is comparable to more monolithic laser systems such as distributed Bragg reflector (DBR) or distributed feedback (DFB), however the linewidth is narrower where typical monolithic systems would often as narrow as 500kHz [32] at 1550nm. One laser was frequency offset locked to another highlighting the capability of the laser to be used in locking experiments. Finally the laser system was shown to resolve the methane line detecting down to a concentration of 1250 ppm. Some improvements and future work will be discussed in the next section. In next chapter the characterisation of lasers based on the new integrated optical fibre platform will be presented.

Bibliography

[1] Y. Sidorin and A. H. Kärkkåinnen, *Tunable optical source*, US Patent 6,920,159, Jul. 2005.

[2] G. Jeong, J.-H. Lee, M. Y. Park, C. Y. Kim, S.-H. Cho, W. Lee, and B. W. Kim, "Over 26-nm wavelength tunable external cavity laser based on polymer waveguide platforms for wdm access networks," *IEEE Photonics Technol. Lett.*, vol. 18, no. 20, pp. 2102–2104, 2006.

[3] B. Niu, H. Yu, L. Yu, D. Zhou, L. Zhao, J. Pan, and W. Wang, "1.65 μm three-section distributed bragg reflective (dbr) laser for ch 4 gas sensor," in *Photonics Asia*, International Society for Optics and Photonics, 2012, 85550Z–85550Z.

[4] S. Li, H. Riris, K. Numata, S. Wu, D. Poulios, A. Ramanathan, J. Abshire, and M. Krainak, "Tunable narrow linewidth laser source for a methane lidar," in *Aerospace Conference, 2012 IEEE*, IEEE, 2012, pp. 1–8.

[5] nanoplus Nanosystems and Technologies GmbH, *DFB laser diodes from 1650 nm to 1850 nm*, http://nanoplus.com/fileadmin/user_upload/Data_sheets/nanoplus_DFB_1650-1850nm.pdf.

[6] Laser 2000 Ltd, *EP1654-DM-B Series, 1653.7 nm Single Wavelength Laser Butterfly Package*, http://www.laser2000.co.uk/ds/DS_00974.pdf.

[7] A. Rickman, G. Reed, and F. Namavar, "Silicon-on-insulator optical rib waveguide loss and mode characteristics," *J. Lightw. Technol.*, vol. 12, no. 10, pp. 1771–1776, 1994.

[8] T. Ikegami, "Reflectivity of mode at facet and oscillation mode in double-heterostructure injection lasers," *IEEE J. Quantum Electron.*, vol. 8, no. 6, pp. 470–476, 1972.

[9] H. Kobayashi and H. Iwamura, "Polarisation-dependent gain-current relationship in GaAs-AlGaAs MQW laser diodes," *Electron. Lett.*, vol. 19, no. 5, pp. 166–168, 1983.

[10] N. Dutta and D. Craft, "Effect of stress on the polarization of stimulated emission from injection lasers," *J. Appl. Phys.*, vol. 56, no. 1, pp. 65–70, 1984.

[11] T. Visser, H. Blok, B. Demeulenaere, and D. Lenstra, "Confinement factors and gain in optical amplifiers," *IEEE J. Quantum Electron.*, vol. 33, no. 10, pp. 1763–1766, 1997.

[12] A. Technologies, *Ap2040 series/ap2050 series optical spectrum analyzer.*

[13] S. Camatel and V. Ferrero, "Narrow linewidth CW laser phase noise characterization methods for coherent transmission system applications," *J. Lightwave Technol.*, vol. 26, no. 17, pp. 3048–3055, 2008.

[14] P. Horak and W. H. Loh, "On the delayed self-heterodyne interferometric technique for determining the linewidth of fiber lasers," *Opt. Express*, vol. 14, no. 9, pp. 3923–3928, 2006.

[15] T. Okoshi, K. Kikuchi, and A. Nakayama, "Novel method for high resolution measurement of laser output spectrum," *Electron. Lett.*, vol. 16, no. 16, pp. 630–631, 1980.

[16] R. Hui and M. O'Sullivan, *Fiber Optic Measurement Techniques.* Academic Press, 2009.

[17] M. Schiemangk, S. Spiessberger, A. Wicht, G. Erbert, G. Tränkle, and A. Peters, "Accurate frequency noise measurement of free-running lasers.," *Appl. Opt.*, vol. 53, no. 30, pp. 7138–43, 2014.

[18] D. M. Akos, M. Stockmaster, J. B. Tsui, and J. Caschera, "Direct bandpass sampling of multiple distinct RF signals," *IEEE Trans. on Commun.*, vol. 47, no. 7, pp. 983–988, 1999.

[19] E. Rubiloa, *Phase Noise and Frequency Stability in Oscillators*, S. C. Cripps, Ed. Cambridge University Press, 2008.

[20] P. D. Welch, "The use of fast fourier transform for the estimation of power spectra: A method based on time averaging over short, modified periodograms," *IEEE Trans. Audio Electroacoust.*, vol. 15, no. 2, pp. 70–73, 1967.

[21] A. Bordonalli, C. Walton, and A. Seeds, "High-performance phase locking of wide linewidth semiconductor lasers by combined use of optical injection locking and optical phase-lock loop," *J. Lightw. Technol.*, vol. 17, no. 2, pp. 328–342, 1999.

[22] F. Friederich, G. Schuricht, A. Deninger, F. Lison, G. Spickermann, P. Haring Bolívar, and H. G. Roskos, "Phase-locking of the beat signal of two distributed-feedback diode lasers to oscillators working in the MHz to THz range.," *Opt. Express*, vol. 18, no. 8, pp. 8621–9, Apr. 2010.

[23] Y. Li, X. Bao, F. Ravet, and E. Ponomarev, "Distributed Brillouin sensor system based on offset locking of two distributed feedback lasers.," *Appl. Opt.*, vol. 47, no. 2, pp. 99–102, 2008.

[24] A. M. Marino and C. R. Stroud, "Phase-locked laser system for use in atomic coherence experiments," *Rev. Sci. Instrum.*, vol. 79, no. January, pp. 1–8, 2008.

[25] L. S. Rothman, I. E. Gordon, Y. Babikov, A. Barbe, D. C. Benner, P. F. Bernath, M. Birk, L. Bizzocchi, V. Boudon, L. R. Brown, *et al.*, "The HITRAN2012 molecular spectroscopic database," *J. Quant. Spectrosc. Radiat. Transf.*, vol. 130, pp. 4–50, 2013.

[26] J. Hodgkinson, Q. Shan, and R. D. Pride, "Detection of a simulated gas leak in a wind tunnel," *Meas. Sci. Technol.*, vol. 17, no. 6, p. 1586, 2006.

[27] J. Hodgkinson and R. D. Pride, "Methane-specific gas detectors: the effect of natural gas composition," *Meas. Sci. Technol.*, vol. 21, no. 10, p. 105 103, 2010.

[28] G. Whitenett, G. Stewart, K. Atherton, B. Culshaw, and W. Johnstone, "Optical fibre instrumentation for environmental monitoring applications," *J. Opt. A: Pure Appl. Opt.*, vol. 5, no. 5, S140, 2003.

[29] J. Hodgkinson, D. Masiyano, and R. P. Tatam, "Gas cells for tunable diode laser absorption spectroscopy employing optical diffusers. part 1: single and dual pass cells," *Appl. Phys. B*, vol. 100, no. 2, pp. 291–302, 2010.

[30] J. Hodgkinson and R. P. Tatam, "Optical gas sensing: a review," *Meas. Sci. Technol.*, vol. 24, no. 1, p. 012 004, Jan. 2013.

[31] F. R. Adikan, C. B. Gawith, P. G. Smith, I. J. Sparrow, G. D. Emmerson, C. Riziotis, and H. Ahmad, "Design and demonstration of direct UV-written small angle X couplers in silica-on-silicon for broadband operation," *Appl. Opt.*, vol. 45, no. 24, pp. 6113–6118, 2006.

[32] Optilab, *1550 nm dfb laser diode, pm output, high performance*, http://www.optilab.com/images/datasheets/DFB-1550-PM-HP_09022016_v2.pdf.

- Chapter 5 -

IOF planar laser

In previous work, our research group demonstrated the integration of fibre onto a silicon substrate as a hot-wire anemometer [1]. The integrated optical fibre was fused to a silicon substrate using a flame-hydrolysis deposition (FHD) process that would normally be used in the fabrication of planar waveguides. The fibre is bonded with a mechanically strong and high optical quality glass providing good acoustical and thermal coupling to the silicon substrate. In this instance the optical qualities of the bonding material are not exploited, but rather the mechanical strength and stability. The platform has advantages from both fibre and planar technologies: fibre technology is highly developed, providing good photosensitivity, lower losses, and greater complexity and precision can be achieved in the waveguide structure. To the author's best knowledge this is the first demonstration of a external cavity diode laser utilizing this platform. All characterisation outlined in this chapter was undertaken by the author.

The integrated optical fibre (IOF) platform uses a fibre which has very low losses compared to planar waveguides that have been fabricated. The device is more readily processed for better surface roughness compared to the planar platform. The high thermal conductivity of the silicon substrate, that the device is bonded to, thermalises the device permitting a more uniform thermal profile over its guiding regions. In contrast to previous fibre Bragg grating (FBG) based external cavity diode laser (ECDL)s, the fibre is made considerably more rigid helping to eliminate the susceptibility to acoustic vibrations which affect the Bragg grating and cavity length. As the IOF is attached to a planar silicon layer this can also facilitate lithographic processing steps such as adding micro-heaters similar to those outlined in Chapter 4.

In this chapter an IOF based ECDL will be detailed. Three versions of this system will be considered that are designed at wavelengths of 1532.83 nm and 1560.48 nm. The overall

system geometry and Bragg grating design of both lasers will be discussed. Laser characteristics will be covered including, laser power, side-mode suppression-ratio, laser intensity and phase noises. As a demonstration of the system, characterisation of the P13 acetylene line will be presented. Finally the improved stability characteristics of packaging the packaged laser system will be discussed.

5.1 System overview and design

5.1.1 Geometry

The system geometry is very similar to the 1651 nm system geometry discussed in Chapter 4. This system instead uses a Thorlabs InP gain-chip with a centre wavelength at 1550 nm, which has a bandwidth of 40 nm. The gain-chip also has an angled, anti-reflection coated facet, and a 90 % reflectivity coated facet. The angular exit of this gain-chip is smaller with a 19.5° angled exit to the normal to satisfy Snell's law as the emission angle from the gain-chip is different at 1550 nm than 1650 nm. The gain-chip die is mounted on a $1.5 \times 1 \times 0.64$ mm silicon carbide submount that is mounted onto a metallic heat sink. This heat sink is screwed onto a aluminium block that encapsulates a thermistor. This block is then attached to a Peltier cooler using thermally conductive epoxy (see Figure 5.1. The injection current and temperature of the gain-chip and the temperature control are controlled using a LDC-3724B diode laser controller.

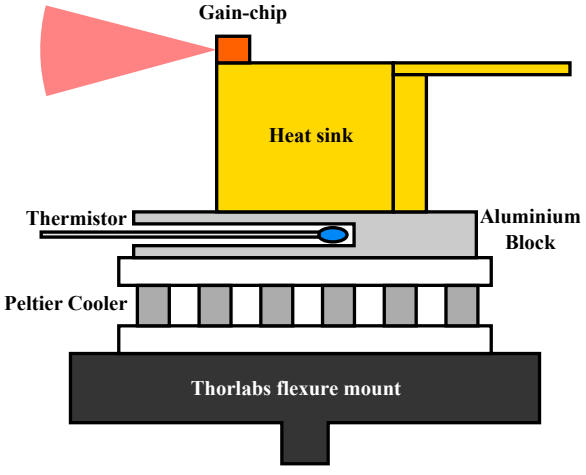

Figure 5.1: Diagram depicting the components comprising the optical mount for the gain-chip used in the stage based prototype system. Components are bonded together using a thermally conductive epoxy. (Not to scale.)

The IOF geometry itself can be seen in 5.2 (Top Left). This geometry consists of a ThorLabs GF4A fibre that is attached to a silica-on-silicon substrate, the fabrication of

which is described in Chapter 3. The GF4A fibre has a core diameter of 3.5 µm with a corresponding mode-field diameter (MFD) of (4.00 ± 0.03) µm. The two are bonded together using a FHD phosphogermanate melt. The IOF hosting a UV-written Bragg reflector was diced into a chip with a triangular tip to prevent material from obstructing alignment. The facet was diced in the ductile regime (see Section 3.3.2.2) with an angle of 13.3°, in order to satisfy Snell's law.

The IOF external cavity is adhered to a V-groove assembly with a polarisation maintaining (PM) fibre. This the output port for where light for analysis is coupled out, which is clamped to a V-groove array holder. This holder is mounted onto a translation stage at an angle of 13.3°. This is aligned close to the gain-chip so that there is a small air gap (<5 µm). Note the chip is not directly adhered using optically transparent adhesive as this would affect alignment, disrupt the anti-reflection coating and introduce a significant intra-cavity loss. The stage systems are then mounted on a breadboard that is isolated using air cushioning to reduce susceptibility to building vibrations. The emerging pigtail is then connected to a Faraday isolator providing ~60 dB isolation. The geometry and corresponding photo can be seen in Figure 5.2 (Top and Bottom Right).

Measuring the coupling loss between the IOF and gain chips was practically difficult and instead it was estimated using a simple elliptical Gaussian model. Elliptical Gaussians were used due as the exact mode structure was not known. From the angular divergence values of the output beam from the gain-chip specifications, an estimate of the near field elliptical Gaussian field could be determined. The IOF chip has a considerably smaller MFD compared to the planar waveguide improving the coupling between the external cavity and the gain chips resulting in a computed loss of approximately ~1 dB. However the small MFD results in a higher coupling loss of 3.5 dB to the PM fibre pigtail though this loss is less critical compared to the intracavity coupling loss of the gain chip.

5.1.2 Grating design

Well established fibre fabrication methods have been extremely successful at producing highly uniform waveguide structures in arbitrary lengths of fibre. Planar waveguides on wafers by comparison have significant variations refractive index and in vertical waveguide structure at different positions on the wafer, there are even variations found on 10 × 20 mm chips [2]. These wafer perturbations in the UV-written waveguides, reducing the precision that Bragg gratings can be fabricated. Unlike the conventional

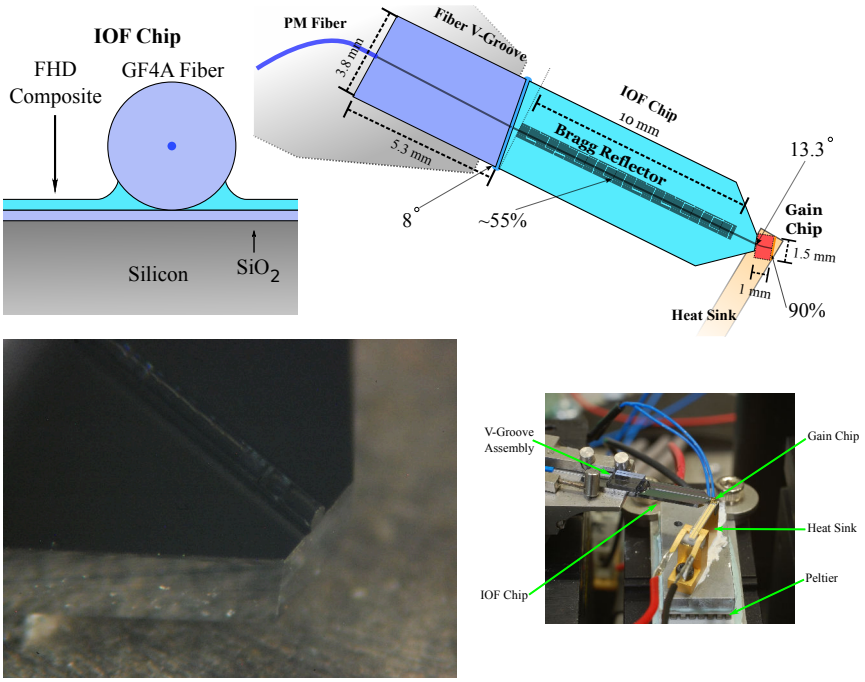

Figure 5.2: (Top Left) Cross section of IOF chip. (Top Right) Schematic of the ECDL employing an IOF device (Bottom Left) Photograph of external cavity taken through a microscope. The tip of the IOF chip is diced to a triangular shape to facilitate alignment with the gain-chip. (Bottom Right) Photograph of prototype system.

planar platform, the IOF platform utilises optical fibre for the waveguide structure, utilising the high consistency and uniformity of commercial optical fibre. When properly characterised, UV-written Bragg gratings can be fabricated with far greater precision. This can forgo the need to use a thermal heating system to accurately move the grating onto the desired wavelength. To demonstrate this, two IOF based laser systems were fabricated utilising gratings written to target the acetylene P13 line (1532.83 nm) and double the wavelength of the rubidium D2 line (1560.48 nm). This second scheme facilitates frequency doubling of the laser for use in rubidium spectroscopy.

In an effort to achieve improved linewidth properties a longer grating was used compared to the previous 1651 nm system, with gratings written with lengths 10 mm and 12 mm for 1532.83 nm and 1560.48 nm respectively. The grating used in the 1532.83 nm system used a uniform grating, as tuneability was not a requirement in this system, a narrow grating would provide excellent reflectivity. It was later found that a uniform grating reflectivity was unnecessarily high as the gain-chip gain-saturates easily with less optical feedback, as a result a Gaussian apodised grating was used for the 1560.48 nm wavelength system. The Gaussian shows good agreement to the theoretical spectrum using coupled mode theory. However the the actual grating is slightly

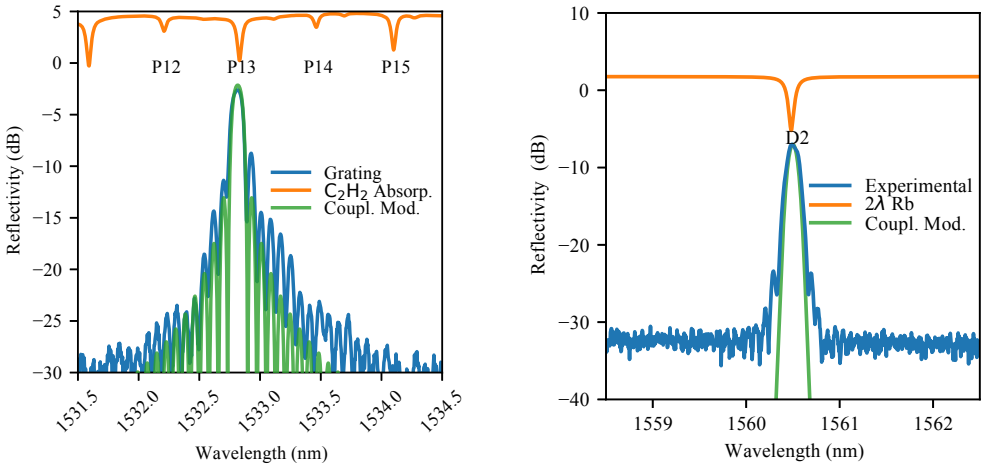

(a) Grating reflection spectrum for an unapodised grating used in the laser external cavity with FWHM of 110 pm. A measured acetylene absorption spectrum has been overlaid for comparison with lines of the P-branch labelled and uses the same log scaling but arbitrary offset. The acetylene spectrum shown was obtained from the internal acetylene cell in the OSA used for calibration. The spectrum is compared to its simulated spectrum using coupled mode theory.

(b) Grating reflection spectrum for a Gaussian grating used in the laser external cavity with FWHM of 150 pm. The simulated rubidium absorption spectrum has been overlaid for comparison with lines of the P-branch labelled and uses the same log scaling but arbitrary offset. The spectrum is compared to its simulated spectrum using coupled mode theory.

Figure 5.3: TE polarised reflection spectra of the gratings used in the laser systems with overlaid absorption lines they are designed to match.

broader and shows higher side bands as the UV-writing system cannot write gratings that perfectly follow the intended apodisation profile.

The 1532.83 nm grating reflectivity was measured to be ~55 %; performed by dicing the end facet of the chip in the ductile regime, the reflected light at the grating resonance is then compared against the detuned reflected light of the end facet whose index and reflectivity is known to be 3.4 %. Based on simulations of the Bragg grating using coupled mode theory it is determined that the grating reflectivity of the Gaussian apodised, 1560.48 nm grating is ~15 %. The spectral responses of the gratings were measured on an OSA using the polarised output of an amplified spontaneous-emission (ASE) source and can be seen in Figure 5.3, the grating has a FWHM of 110 pm.

5.2 System characterisation

In this section some of the basic optical properties are given for the laser systems. The laser behaviour with injection current is outlined. Finally the relative intensity noise (RIN) and phase noise properties of the laser systems are discussed.

The free spectral range (FSR) of the cavity of the 1532.83 nm system is ~7.5 GHz (59 pm), corresponding to an effective optical cavity length of 20 mm; this value was directly measured from the OSA and corresponds to the effective cavity length that solves the phase condition of the cavity. Interestingly this inferred cavity length is longer than what would be expected. This is likely the combined effects of a non-linear phase response from the strong Bragg grating, and the effects of the group indices of the IOF external cavity chip and gain chip. Despite the longer effective cavity length the grating reflector is sufficiently narrow to ensure only one longitudinal mode can lase. The laser power characteristic with injection current is shown in Fig. 5.4, with a threshold current of 50 mA. A consequence of a narrow grating spectrum compared to the FSR is that mode hops cause significant changes in the output power of the laser as seen by the large discontinuity in Fig. 5.4, this is an unintended consequence of using such a strong grating. This mode hop occurs as the laser mode moves spectrally to a regime where the grating feedback is lower and slightly less preferable to the laser. However the intra-cavity power of the mode is still close to gain-saturating but there is a significant change to the output coupled power due the lower transmission of the Bragg grating at that wavelength. This effect would be mitigated by weakening the reflectivity of the Bragg grating and by using a spectrally broader grating that is more comparable to the FSR, through apodisation or chirp. This same effect of the variation in output coupling results in the nonlinear relationship between current and output power. As the current is increased the active longitudinal mode sweeps spectrally across the reflection spectrum of the grating which is highly wavelength dependent resulting in a variation in output coupling. In this stage based setup, the avoidance of mode hops in desired tuning ranges could be achieved by adjusting the cavity length using the translation stages, enabled by the tuning of the small air gap between the IOF and gain-chip. The grating provides suppression of other longitudinal modes leading to a side-mode suppression-ratio (SMSR) of >60 dB (see Fig. 5.4.) and decreasing to ~45 dB on the threshold of mode hopping. Note that the spectral shape, including the shoulder seen in Fig. 5.4, is an artefact of the OSA and not a feature of the line shape of the laser spectrum.

In the 1560.48 nm system, the use of a lower, 15 % reflectivity reflector, seemed to significantly improve the linearity of the laser output during injection current sweeping. The

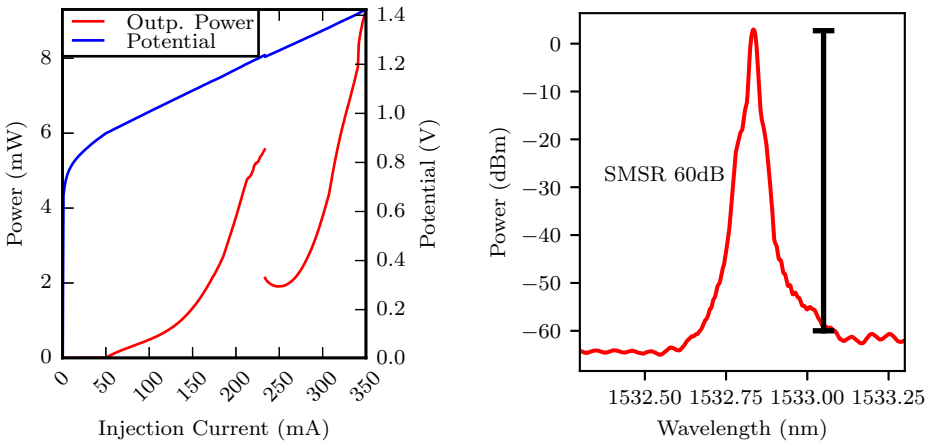

Figure 5.4: (Left) Power current curve of laser of 1532.83 nm wavelength system. Threshold was measured at 50 mA. A mode hop occurs at 200 mA. (Right) Spectrum of laser taken on OSA with 20 pm resolution bandwidth. The spectrum indicates a >65 dB SMSR.

threshold at 50 mA is still maintained. During the sweep, as seen in Figure 5.5 (left), the power undergoes a mode hop at 200 mA. The decrease in power during the mode hope suggests again that the gain-chip is gain saturating indicating that even a reflectivity of ~15 % is higher than needed. Also seen in Figure 5.5 (right) is the spectrum of the laser measured on an OSA, confirming single mode lasing with an SMSR of ~65 dB. The higher SMSR could be a result of using a Gaussian apodised grating with significantly higher side lobe suppression than the uniform grating.

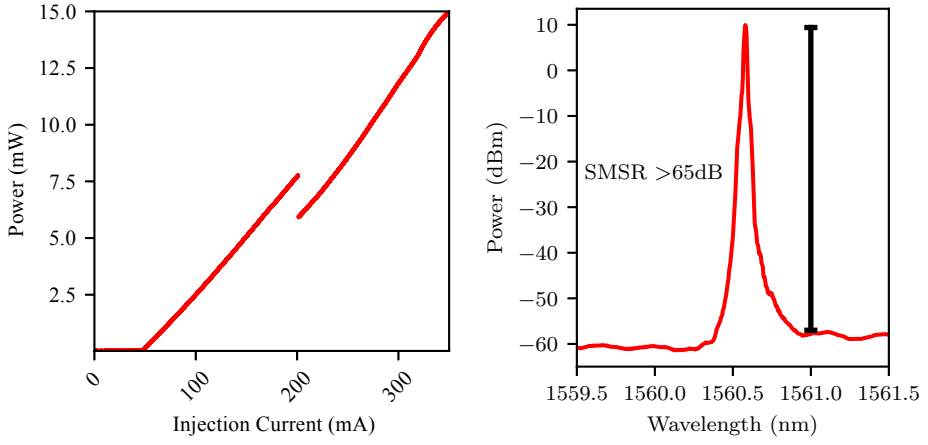

Figure 5.5: (Left) Power current curve of 1560.48 nm laser. Threshold was measured at 50 mA. A mode hop occurs at 233 mA. (Right) Spectrum of laser taken on OSA with 20 pm resolution bandwidth. The spectrum indicates a ~60 dB SMSR.

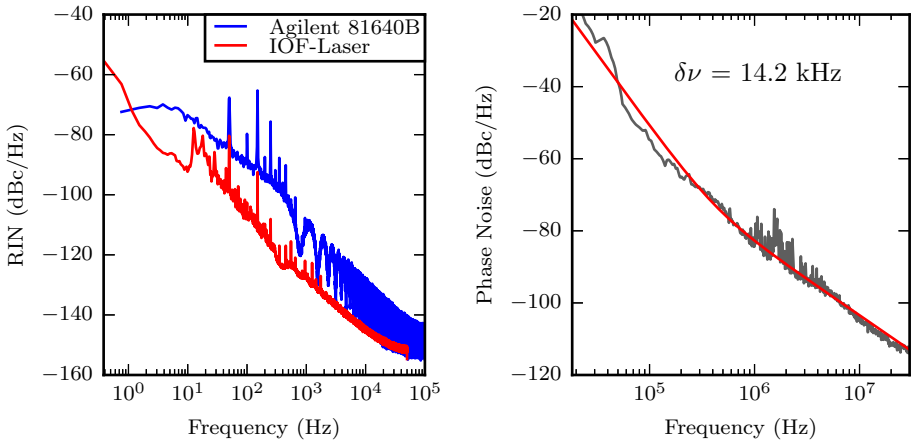

Figure 5.6: (Left) RIN of the the IOF laser measured for 10 s compared with a tunable Agilent 81640B measured for 1 s. Peaks can be seen at 50 Hz and its harmonics. Much of the low frequency noise is dominated by acoustics. The current prototype setup is susceptible to vibrations and thermal fluctuations in the environment. This measurement was taken at 1532.86 nm, with an injection current of 320 mA, and the optical power attenuated down to ~0.5 mW. (Right) The phase noise plot derived from the beat note of the an Agilent 81640B laser and the IOF laser measured for 5 ms. The plot is fitted to noise parameters as specified by [3]. The Lorentzian linewidth is given as 14.2 kHz - this linewidth is the sum of linewidths of the Agilent and IOF lasers. This measurement was taken at 1532.86 nm, with an injection current of 320 mA and an optical power of 5 mW.

5.2.1 Noise properties

To measure the intensity noise, the outputs from the laser systems were incident on the 15 GHz Agilent 11982A Lightwave Converter, providing a signal with intensity noise information, which was sampled on a 16-bit resolution, 5MHz bandwidth, oscilloscope (Picoscope 4262). The signal was normalised using the method described in Section 4.5, and the power spectral density (PSD) was estimated using Welch's method and is displayed on Figure 5.6). As the existing prototype arrangement is mounted on translation stages there is significant instability nearer the low frequencies due to increased susceptibility to acoustics and thermal drifts; it is expected that if the external cavity and gain-chip were bonded to a monolithic substrate this would significantly reduce the effects of the thermal fluctuations and susceptibility to acoustical effects. At higher frequencies the noise floor is limited to around −150 dBc/Hz which is close to the shot noise limit at the measured optical power.

To accurately measure the frequency noise or linewidth property of the laser a heterodyne technique with another narrow linewidth laser is used. The resulting beat note is recorded on a 3 GHz bandwidth oscilloscope and multiple time traces are taken

for averaging. The sampled beat note is processed using the procedure described in Section 4.6.2 and the PSD is estimated using Welch's method using a Hanning window as described in Chapter 4.

The laser output of the IOF was mixed with the output from an Agilent 81640B tuneable ECDL onto a photodiode and the beat signal recorded by sampling the signal on an oscilloscope. The time signal was post processed to produce a phase noise plot. Using the phase noise model specified by Camatel and Ferrero [3], and fitting this model to the phase noise, the Lorentzian linewidth is measured to be 14.2 kHz [4]. The Agilent tunable laser is specified with a linewidth of 100 kHz [5], which was determined using a delayed self-heterodyne measurement. Camatel and Ferrero measured the intrinsic Lorentzian linewidth of a very similar Agilent model, that had the same specified linewidth, to be only 8 kHz [3]. Their measurement was obtained and confirmed using both an optical phase locked loop (OPLL) and a Michelson interferometer method, and then fitting the same noise model as used in our phase noise plots. Given that the width of the intrinsic Lorentzian spectrum obtained from the beat note signal is the sum of both lasers' Lorentzian widths we can at least specify that the IOF laser has a linewidth of <14 kHz.

5.3 Acetylene spectroscopy

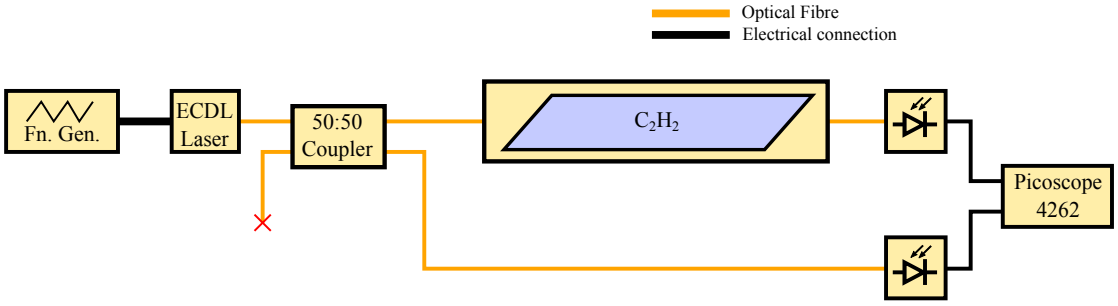

Figure 5.7: Experimental configuration used to detect acetylene. The acetylene cell is a 20 Torr acetylene cell acquired from Wavelength References.

The experimental system used to scan the P13 acetylene line is shown in Figure 5.7. The ECDL system injection current was modulated using a triangle wave at 60 Hz, causing the laser to tune through the C_2H_2 spectral line. The output of the laser was split using a 50:50 fibre splitter, where one arm passed through a fibre coupled, sealed, 5.5 cm, 20 Torr gas cell onto a photodiode; the other arm passed directly onto another photodiode. The outputs of the detectors were then sampled using a Picoscope 4262. By taking the trace of filtered and unfiltered light simultaneously, the nonlinear variation

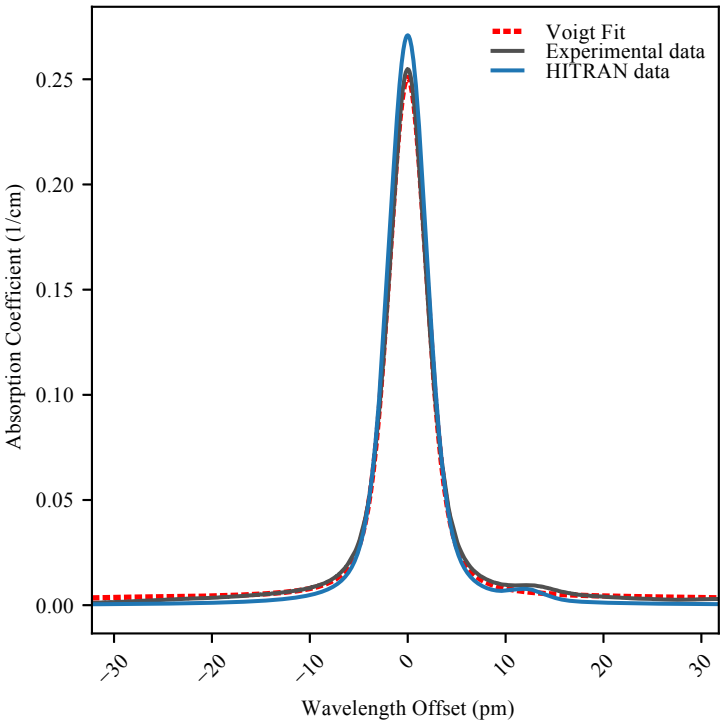

Figure 5.8: Scan of the P13 acetylene line. Acetylene gas cell is held at a pressure of 20 Torr (2.67 kPa). The difference in measured strength and the strength suggested by the HITRAN database is likely due to the tolerances of the gas cell. The bump at the right of central peak is another much weaker absorption line shown in the HITRAN simulation absorption spectra and is also observed in the laser scan.

in the power output with injection current of the laser system could be removed using digital processing.

The processed scan is fitted using a Voigt profile. The fitted Voigt FWHM is compared to the FWHM of another Voigt profile fitted to the simulated data produced from the HITRAN database to infer the x-axis scale [6]. The corrected data, the fitted Voigt profile, and the HITRAN simulation can be seen in Figure 5.8.

5.4 Miniaturised and packaged laser system

Using translation stages to maintain the laser system geometry provides flexibility by allowing adjustments to the cavity alignment and optical length by varying the size of the small air gap that exists between the gain-chip and the IOF chip. Changing the external cavity also becomes a simple process of removing the existing external cavity and replacing with a different device and aligning again. However the relatively large

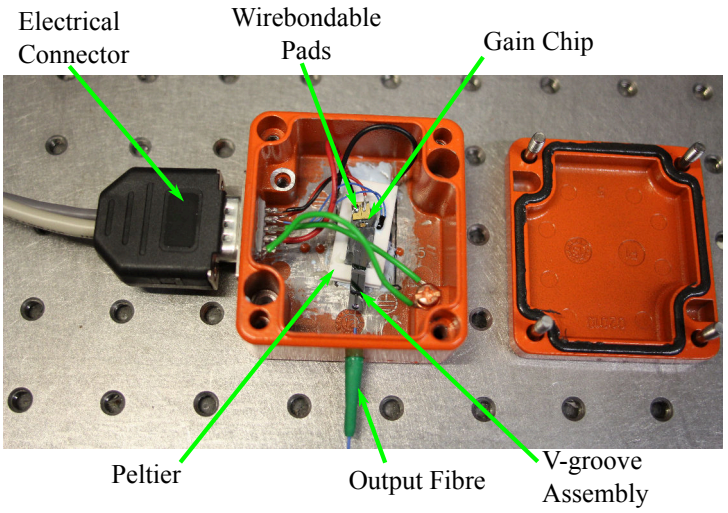

Figure 5.9: Birds-eye photo of the system. Photo taken courtesy of Teresa Ferreiro.

metallic translation stages exhibit large drifts with temperature. In addition, there is a large volume of solid material between the gain-chip and the external cavity chip, via the translation stages and bread board. This will permit the existence of a number acoustic standing wave modes at lower frequencies where acoustical environment noise is higher, as acoustic noise generally exhibits $1/f$ characteristics [7].

The functional components that make up the ECDL excluding the translation stages are much smaller, on the order of several centimetres. This gives great potential for miniaturising the system by changing the method of mounting the devices. In this implementation the components are fixed using adhesives to a common silicon substrate, as described in Chapter 3. A photo depicting the assembled system can be seen in Figure 5.9, details of the packaging can be found in Section 3.7.3. This should eliminate many of the standing wave acoustical modes that can form between the gain-chip and external cavity chip. The thermal expansion of the silicon, that is better matched to the silicon-carbide gain-chip submount, helps suppress alignment issues due to thermal drift.

The packaged laser demonstrated similar capabilities of the previous lasers with improvements to noise. The laser produced an output power, with single mode operation, at 1560.5 nm of 5 mW, and SMSR of >55 dB (Figure 5.10).

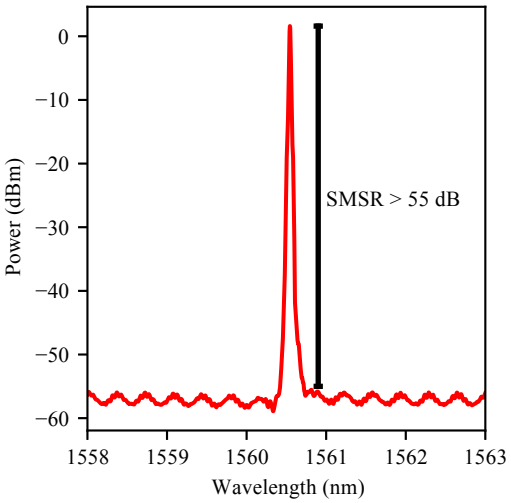

Figure 5.10: The optical spectrum of the packaged laser measured on an OSA demonstrating single frequency operation with >55 dB SMSR. The fringes seen at the spontaneous emission noise floor comes from the weak internal cavity mode of the gain-chip itself corresponding to an optical length of ≈1 mm.

5.4.1 Noise improvements of packaged system

There are number of physical mechanisms that contribute to RIN, the two often discussed in the literature are mode partition noise and spontaneous emission noise. In realised systems often the most important contributions are variations in the output power to due to thermal drift in alignment and acoustic vibrational modes in the geometry of the system from environmental noise and air currents.

To indicate the improvement of noise characteristics by packaging the system in the way described in Section 3.7.3, the RIN is given and compared to a similar system realised utilising translation stages in Figure 5.11. The RIN plot demonstrates improved low frequency noise and an elimination of a band of noise centred around ~40 Hz. At very low frequencies where thermal fluctuations contribute more there is a 15 dB improvement.

In addition to the RIN, a preliminary linewidth measurement was made by beating the output of the packaged laser with the output of the translation stage based laser. Using the same fitting procedures as covered before the resulting plot can be seen in Figure 5.12.

The linewidth is measured to be somewhat higher than previous measurements ≫14 kHz. It was later discovered that when this measurement was obtained the laser cavity had been suffering significant losses as a result of an oil depositing in the air gap between

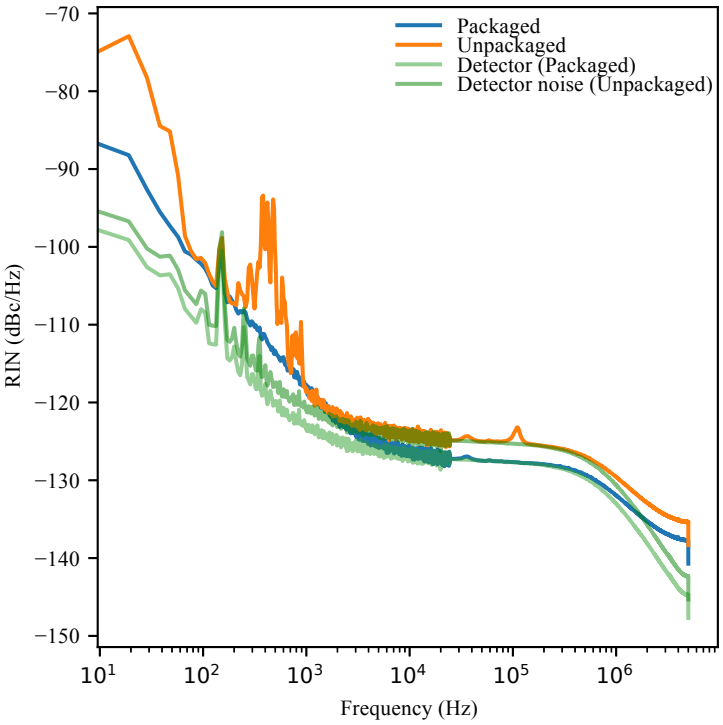

Figure 5.11: The RIN of a packaged laser, and a translation staged based laser. There are demonstrably noticeable improvements in the laser stability after packaging. Welch's method was applied separately for the lower frequencies and higher frequencies using different sized windows to optimise plot variance. The background noise contributed by the detector is included in green normalised by the mean power of the packaged and unpackaged laser respectively.

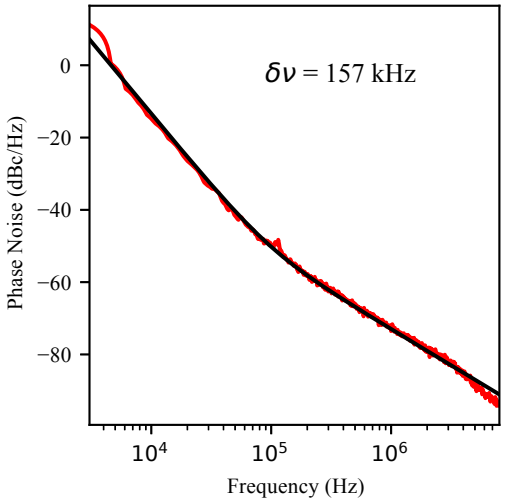

Figure 5.12: The phase noise of the beat note between the packaged and unpackaged lasers at 1560 nm. It cannot be assumed that the linewidth is half the fitted value due to the oil contaminant only that the linewidth of the packaged laser is <157 kHz.

the facets of the gain-chip and external cavity chip. The source of the oil is most likely due to a pocket of uncured glue between the V-groove and the chip shadowed from curing by the silicon on both these pieces. It is likely the oil flowed along the length of the attached fibre on the IOF chip through capillary action. The presence of the oil seems to introduce significant losses into the system most likely through a combination of misalignment due to refraction (as the alignment and AR coating is optimised for air), and transmission loss of the oil. A simple fix for future devices would be to flip the V-groove upside down as the top of the V-groove is glass and would transmit the UV light to lower half of the joint allowing the join to be fully exposed and cured.

5.5 Future work

Packing the system imparted significant advantages in stability and miniaturisation. However some number of days after packaging, an oil based contaminant transferred to the intra-cavity facets of the gain and external cavity chips impeding investigations. The oil contaminant needs to be properly identified and eliminated depending on the source. This would likely either be through improvements in process cleanliness during optical alignment and assembly, or using alternative adhesives that do not precipitate oily residues.

Further investigation and research into the IOF platform could allow for a fibre connection to be directly spliced to the system without the need for V-groove pigtail. One route to achieve this would be to directly splice a fibre to the chip using a CO_2 fibre splicer. Alternatively, further optimisation of the FHD recipe and the sintering process should allow for fibres to be bonded onto chips with the fibre protruding off with a length long enough to splice a fibre to.

The UV-writing system is capable of producing gratings with chirp where the Bragg period varies over the length of the grating. Chirped gratings introduce a nonlinear phase delay response with wavelength. Depending on the orientation of the chirp, this could be used to create longitudinal resonator modes that are resistant to changes in the cavity length thereby improving linewidth, or indeed can be made to be significantly more sensitive improving tuneability at the expense of frequency stability.

In Chapter 4 the laser system demonstrated that it could be frequency offset locked. With the capability to write at arbitrary spectroscopic lines, a system could be developed that locks one laser system to a gas line, whilst using another laser that is frequency offset locked to scan the absorption line. This spectroscopic method would provide

absolute frequency measurement of the spectral line relative to the line centre as a result of being able to measure the beat note with conventional electronics. These types of locking schemes can be used in atom trapping and would have applications in spectroscopy and Doppler atom cooling.

5.6 Conclusions

The IOF platform has demonstrated the capability of UV-writing Bragg gratings accurately at a wide range of wavelengths allowing rapid development of working devices. Three laser systems based on the IOF technology were demonstrated at wavelengths on the acetylene P13 absorption line (1533 nm) where the line was characterised, and two systems at twice the wavelength of the rubidium R4 absorption line (1560 nm) utilising UV-written Bragg gratings on the IOF platform. These lasers were demonstrated to be single frequency with laser properties that compare well, or perform better than, existing single frequency systems in terms of SMSR, RIN and phase noise.

The laser system was able to be miniaturised and the components fixed onto a silicon substrate that was housed in an aluminium enclosure. The enclosed system showed improved stability, with a significant reduction in weight and size. This demonstrates the laser is capable of being further developed for enclosure in a bespoke package that would be suitable for field applications and industry. The next chapter will summarise the work covered in this thesis as well as some future directions for research.

Bibliography

[1] C. Holmes, J. C. Gates, and P. G. R. Smith, "Planarised optical fiber composite using flame hydrolysis deposition demonstrating an integrated FBG anemometer.," *Opt. Express*, vol. 22, no. 26, pp. 32 150–7, 2014.

[2] H. L. Rogers, "Direct UV-written Bragg gratings for waveguide characterisation and advanced applications," PhD thesis, University of Southampton, Apr. 2013.

[3] S. Camatel and V. Ferrero, "Narrow linewidth CW laser phase noise characterization methods for coherent transmission system applications," *J. Lightwave Technol.*, vol. 26, no. 17, pp. 3048–3055, 2008.

[4] S. G. Lynch, C. Holmes, S. A. Berry, J. C. Gates, A. Jantzen, T. I. Ferreiro, and P. G. R. Smith, "External cavity diode laser based upon an FBG in an integrated optical fiber platform," *Opt. Express*, vol. 24, no. 8, pp. 8391–8398, 2016.

[5] Keysight Technologies, *81480B, 81680/40/72B, 81482B, & 81642B tunable laser modules user's guide*, http://www.keysight.com/upload/cmc$\delimiter"026E30F${_}upload/All/b$\delimiter"026E30F${_}tlsB0402.pdf.

[6] L. S. Rothman, I. E. Gordon, Y. Babikov, A. Barbe, D. C. Benner, P. F. Bernath, M. Birk, L. Bizzocchi, V. Boudon, L. R. Brown, *et al.*, "The HITRAN2012 molecular spectroscopic database," *J. Quant. Spectrosc. Radiat. Transf.*, vol. 130, pp. 4–50, 2013.

[7] B. De Coensel, D. Botteldooren, and T. De Muer, "1/f noise in rural and urban soundscapes," *Acta acustica united with acustica*, vol. 89, no. 2, pp. 287–295, 2003.

- Chapter 6 -

Conclusions

This chapter gives a summary of the work carried out and of significant results of the work described in this thesis. A comparison is given between the lasers researched in this thesis and comparable state of the art lasers commercially available or published in the literature. The chapter finishes by proposing possible future directions of this research.

In this research a number of single frequency lasers have been built utilising integrated single mode external cavities with UV-written Bragg gratings for optical feedback. Using a direct UV-writing technique for fabricating Bragg gratings allows gratings to be written at arbitrary wavelengths with high accuracy.

The advantages of using a planar external silica-on-silicon waveguide has been demonstrated by the capability of lithographically defining and depositing micro-heater assemblies directly over the waveguide, an approach not suitable for optical fibres. These micro-heating devices are able to modulate at a frequency of 1.5 kHz. A planar external cavity diode laser (ECDL) has built and demonstrated to tune to and operate at the 1651 nm methane gas line sensing down to 1250 ppm and characterising the absorption spectrum.

This research has demonstrated integrated optical fibre (IOF) technology to be an excellent optical platform for building an ECDL, by enabling the accurate fabrication of Bragg gratings. Good fabrication tolerances allow assembly of ECDLs directly at 1560.48 nm and 1532.83 nm, the 2λ of the D2 line of Rubidium, and the P13 line of acetylene.

The lasers developed as part of this project have all demonstrated narrow linewidths as low as <14 kHz. The relative intensity noise (RIN) was also demonstrated to be low,

performing better than a commercial [1] grating-based laser, with higher frequencies limited by the noise floor of the photodiode.

6.1 Comparison with existing published and commercial lasers

To understand how the properties of the lasers considered in this thesis compare to other compact single frequency lasers this section will compare some of the properties of commercially available and published lasers. Attention was only paid towards lasers that were reasonably compact, single frequency and were reasonably close in wavelength to the lasers considered here. Exceptions were made to identify state of the art of narrow linewidth, single frequency, free running lasers. Free running being defined as lasers that were not operating as a slave or part of an active control loop to lock to the laser frequency. The list of lasers and the properties being considered is given in Table 6.1. Intensity noise was not considered as most lasers without moving parts have excellent noise properties and these values are not produced reliably or comparably between manufacturers.

Fibre lasers and nonplanar ring oscillator (NPRO)s are considered as they represent the state of the art of narrow linewidth lasers available at the time of writing. They do however have serious limitations: the NPRO is currently only available at two frequencies: 1064 nm and 1319 nm as it is based upon using a Nd:YAG limiting the operational wavelengths; fibre lasers have a similar limitation that there must be a suitable rare earth dopant to operate a particular wavelength, though a wide variety of dopants exist there are large gaps in operable wavelengths as indicated in Table 6.1. An additional limitation to both lasers is that they cannot be tuned easily, though highly tuneable examples of fibre lasers exist in the literature, they are usually at the expense of other properties such as linewidth [12]. Finally the fibre laser usually has to be hosted in relatively large package to contain and insulate the fibre coil properly and to contain the pump.

The 1651 nm laser researched in this thesis compares very favourably to other lasers available at the same wavelength. To the author's knowledge the 1651 nm lasers discussed in this research have the highest side-mode suppression-ratio (SMSR) of any laser commercially made or published in the literature. The linewidth is also one of the narrowest reported at 1651 nm where only the linewidth generated from the Sacher-Lasertechnik Littman laser produced is narrower [2]. Like many Littman lasers

Table 6.1: Table comparing similar lasers and their properties. Wavelength values given represent the availability of wavelengths rather than tuneability unless otherwise specified. Dimensions given in the package type column represent the largest dimension of the device.

Laser	Wavelength (nm)	Power (mW)	Lorentzian Linewidth (kHz)	SMSR (dB)	Package Type
Planar laser	1651	6.5	220*	55	Lab Table
IOF laser	1533	8.5	N.M.	60	Lab Table
IOF laser	1561	15	<14*	65	Lab Table
Packaged IOF laser	1561	5	157*	55	6cm Box
Sacher Lasertechnik Littman [2]	1600-1800‡	20	100*	40	20 cm Box
DFB Lasers [3]–[5]	Near IR	<50	<3000**	<40	Various Compact
Redfern Planar ECDL [6]	1530-1565	20	2**	55	Butterfly Pkg.
Sacher Lasertechnik Laser VHG ECDL [7]	638-1064	250	<100* 18 @ 780 nm*	45-50	TO 3cm
Vescent Short ECDL [8]	1180-1610	40	50*	N.P.	10 cm Box
Laser 2000 SQWL [9]	1550	5	100**	40	Butterfly Pkg.
Coherent NPRO [10]	1319	800	<1*	N.P.	17 cm Box
SCOWECL [11]	1550	370	1**	80†	40 cm Box
Fibre laser	1030 1064 1535-1570 1900-2050	>5 W	>0.200***	>50	Benchtop/ OEM (>20cm)
Littrow and Littman lasers	Near IR	<50	10-200***	55	Benchtop/ OEM (>20cm)

Lasers researched in this thesis. Specific lasers available commercially. Specific laser found in scientific literature only. Widely available lasers.

* Measured using beat note from two lasers. ** Measured using self-heterodyne or self-homodyne and fitting. *** Range of linewidth values published for these types of lasers † Not directly measured. ‡ Laser's tuning range.

SQWL (Strained quantum well laser), NPRO (Non-planar ring oscillator), SCOWECL (Slab-coupled optical waveguide external cavity, OEM (original equipment manufacturer), N.M. (not measured), N.P. (not published). Laser)

however, they suffer from some stability problems from utilising moving parts and are usually contained in relatively large original equipment manufacturer (OEM) or benchtop style packages. Although the 1651 nm laser demonstrated in this thesis was based on translation stages which would suffer the same problems, it was demonstrated that these lasers could be enclosed in a fixed and compact package in Section 5.4. The only other compact lasers available for measuring at this wavelength are a number of distributed feedback (DFB) based lasers, whose linewidths are usually a number of MHz [4], [13].

The IOF based lasers considered in this thesis show comparable single frequency properties to many other compact devices produced commercially such as Redfern's Planex laser and Sacher-Lasertechnik's Micron Laser. The best linewidth value produced in this thesis (<14 kHz) compares well to aforementioned commercial lasers. To the author's knowledge the SMSR of the laser at 1561 nm matches the highest published value for a diode based laser [14] and is higher than any of the commercial lasers found by the author. Though the IOF laser that was enclosed in a compact package did display an a linewidth of ~160 kHz this could be explained by alignment error and the use of a shorter Bragg grating both of which would impact overall linewidth.

The lasers produced in this thesis demonstrate wavelength flexibility and favourable low noise and single frequency lasing. The lasers have compared well to other similar lasers available commercially and demonstrated that they can be miniaturised into a compact form factor.

6.2 Future directions for research

6.2.1 Towards a narrow linewidth source for rubidium

Rubidium has been the subject of a number of optical cooling and Bose-Einstein condensation experiments. Though many 780 nm laser sources currently exist based on traditional Littrow and Littman-Metcalf configurations [15], [16]; their spatial mode qualities are typically poor and they also suffer from alignment and mechanical stability issues in applications that require portability. Highly stable, frequency doubled, single frequency fibre lasers have been demonstrated previously [17], [18]. Fibre lasers based around erbium doped fibre amplifiers at 1560 nm demonstrate high powers, narrow linewidths, with high spatial mode quality making them suitable for single pass frequency doubling configurations.

In Chapter 5 a single frequency laser was demonstrated at 1560.48 nm, which can be frequency doubled to the Rb D2 line (780.24 nm). In parallel to this research, our research group have been developing single mode diced waveguides in periodically-poled lithium-niobate (PPLN) suitable for frequency doubling to 780 nm. Waveguiding PPLN chips confine light to a small cross-section, maintaining a high intensity light profile through the length of the chip therefore improving the efficiency of second harmonic generation (SHG) conversion. Combining the stable laser with the high conversion efficiency of a waveguiding PPLN chip provides a high stability source important for Rb spectroscopy, which can be used for Rb locking and spectroscopy experiments. The efficiency can be further improved by utilising the mature amplifying technology that an erbium doped fibre amplifier (EDFA) provides without significantly impacting the noise properties of the system; an advantage made possible by seeding with a source at telecommunications wavelengths. To eliminate the needed for an expensive fibre amplifier, a cavity enhanced SHG configuration could be used instead.

6.2.2 Towards a stable package

The package used to encapsulate a laser in Chapter 5 was a simple aluminium enclosure intended for prototype electronics. A package designed to dimensions of the laser system could significantly reduce the overall size of the package. The spatial footprint of the device is important in some applications such as using the device in space applications such as gravity wave sensing. The package would continue to be aluminium as the thermal expansion of the package would not affect the internal alignment of the laser and aluminium has superior thermal and electrical conductivity (for EMF isolation) compared to other standard packaging materials. For an industry capable device, the housing could be assembled in an inert atmosphere such as dry nitrogen, improving longevity and long term stability of the laser by preventing moisture and oxygen from ageing the gain-chip, adhesives, and external cavity chip.

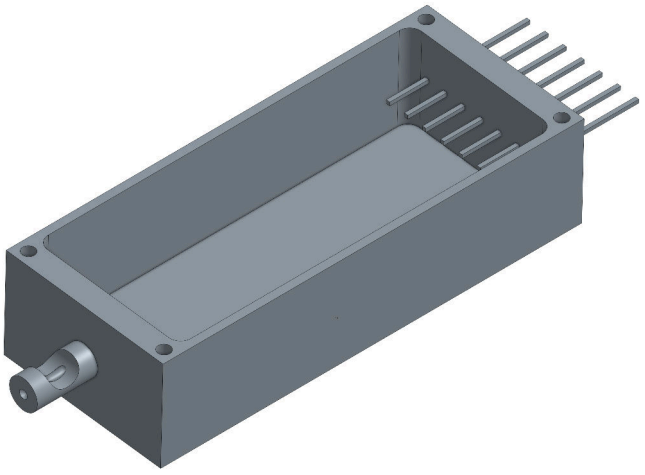

Figure 6.1: CAD diagram of bespoke package design. Package will be made of aluminium as this confers greatest thermal and electrical conductivity, and is relatively cheap compared to other common packaging materials.

Bibliography

[1] Keysight Technologies, *81480B, 81680/40/72B, 81482B, & 81642B tunable laser modules user's guide*, http://www.keysight.com/upload/cmc$\delimiter"026E30F${_}upload/All/b$\delimiter"026E30F${_}tlsB0402.pdf.

[2] Sacher-Lasertechnik GmbH, *TEC-500-1650-020*, https://www.sacher-laser.com/downloads/specifications/6TCcN5_en.pdf.

[3] Optilab, *1550 nm dfb laser diode, pm output, high performance*, http://www.optilab.com/images/datasheets/DFB-1550-PM-HP_09022016_v2.pdf.

[4] nanoplus Nanosystems and Technologies GmbH, *DFB laser diodes from 1650 nm to 1850 nm*, http://nanoplus.com/fileadmin/user_upload/Data_sheets/nanoplus_DFB_1650-1850nm.pdf.

[5] Laser Components GmbH, *Spectroscopic DFB-Lasers: SPECDILAS®-D*, http://www.lasercomponents.com/fileadmin/user_upload/home/Datasheets/divers-ir/spectroscopic-dfb-lasers.pdf.

[6] Redfern Integrated Optics, *RIO PLANEX^{TM} external cavity laser*, http://www.rio-lasers.com/pdf/Rio_Planex_Product%20Brief_1.24.14.pdf.

[7] S. Rauch and J. Sacher, "Compact bragg grating stabilized ridge waveguide laser module with a power of 380 mw at 780 nm," *IEEE Photonics Technol. Lett.*, vol. 27, no. 16, pp. 1737–1740, 2015.

[8] Vescent Photonics, *CECL Laser Module*, http://www.vescent.com/manuals/doku.php?id=d2:cecl_laser.

[9] Laser 2000 Ltd, *EP1550-NLW-B Series, 1550nm Narrow Linewidth Laser - Butterfly*, http://www.laser2000.co.uk/ds/DS_00973.pdf.

[10] Coherent Inc, *Mephisto Lasers*, https://www.coherent.com/lasers/main/mephisto-lasers.

[11] W. Loh, F. O'Donnell, J. J. Plant, M. Brattain, L. J. Missaggia, and P. W. Juodawlkis, "Packaged, high-power, narrow-linewidth slab-coupled optical waveguide external cavity laser (scowecl)," *IEEE Photonics Technol. Lett.*, pp. 1–3, 2011.

[12] A. Castillo-Guzman, J. Antonio-Lopez, R. Selvas-Aguilar, D. May-Arrioja, J. Estudillo-Ayala, and P. LiKamWa, "Widely tunable erbium-doped fiber laser based on multimode interference effect," *Opt. Express*, vol. 18, no. 2, pp. 591–597, 2010.

[13] OSI Laser Diode Inc, *DSCW 1731F-D40R*, http://www.laserdiode.com/product_pdf/10-4400-0060IR-Data_Sheet_for_SCW_1731F-D40R.pdf.

[14] Z. Lu, P. Poole, J. Liu, P. Barrios, D. Poitras, Z. Jiao, G. Pakulski, J. Caballero, D. Goodchild, B. Rioux, *et al.*, "Inas/inp quantum dot laser devices around 1550 nm for fiber communications," in *Information Photonics (IP), 2011 ICO International Conference on*, IEEE, 2011, pp. 1–2.

[15] K. MacAdam, A. Steinbach, and C. Wieman, "A narrow-band tunable diode laser system with grating feedback, and a saturated absorption spectrometer for Cs and Rb," *American Journal of Physics*, vol. 60, pp. 1098–1098, 1992.

[16] S. E. Park, T. Y. Kwon, E. Shin, and H. S. Lee, "A compact extended-cavity diode laser with a Littman configuration," *IEEE Transactions on Instrumentation and Measurement*, vol. 52, no. 2, pp. 280–283, 2003.

[17] S. Sané, S. Bennetts, J. Debs, C. Kuhn, G. McDonald, P. Altin, J. Close, and N. Robins, "11W narrow linewidth laser source at 780nm for laser cooling and manipulation of rubidium," *Opt. Express*, vol. 20, no. 8, pp. 8915–8919, 2012.

[18] F. Lienhart, S. Boussen, O. Carraz, N. Zahzam, Y. Bidel, and A. Bresson, "Compact and robust laser system for rubidium laser cooling based on the frequency doubling of a fiber bench at 1560 nm," *Appl. Phys. B*, vol. 89, no. 2-3, pp. 177–180, 2007.

- Appendix A -

Conference and journal publications

S. G. Lynch, C. Holmes, S. A. Berry, J. C. Gates, A. Jantzen, T. I. Ferreiro, and P. G. R. Smith, "Narrow linewidth external cavity diode laser using UV-written gratings in an integrated optical fiber platform." Opt. Express **24**(8), 8391–8398 (2016).

S. G. Lynch, C. Holmes, S. A. Berry, J. C. Gates, A. Jantzen, T. I. Ferreiro, and P. G. R. Smith, "External cavity diode laser based upon an FBG in an integrated optical fiber platform." CLEO: Science and Innovations, (2016).

S. G. Lynch, J. C. Gates, S. A. Berry, C. Holmes, and P. G. R. Smith, "Thermally tunable integrated planar Bragg-grating stabilized diode laser." SPIE OPTO, (2015).

S. G. Lynch, F. Chen, J. C. Gates, C. Holmes, S. E. Staines, S. W. James, J. Hodgkinson, P. G. R. Smith, and R. P. Tatam, "Bragg-grating-stabilized external cavity lasers for gas sensing using tunable diode laser spectroscopy." Proc. SPIE 9382, Novel In-Plane Semiconductor Lasers XIV, 93820O, (2014).

S. G. Lynch, J. C. Gates, J. Hodgkinson, R. P. Tatam, and P. G. R. Smith, "Integrated planar Bragg grating stabilized diode lasers for TDLS." FLAIR, (2014).

J. C. Gates, S. G. Lynch, C. Holmes, C. Sima, P. L. Mennea, and P. G. R. Smith "Integrated planar Bragg grating stabilized diode lasers." CLEO, (2013).